CAPITAL UNIVERSITY OF SCIENCE AND
TECHNOLOGY, ISLAMABAD

Multiscale Design and Analysis of a TPMS-Based Biomimetic Femoral Stem Implant

by

Muhammad Noman Shahid

A thesis submitted in partial fulfillment for the
degree of Master of Science

in the

Faculty of Engineering
Department of Mechanical Engineering

2025

I dedicate this thesis to Allah Almighty, whose endless mercy and guidance have been my strength throughout this journey. And to my beloved family, whose unwavering support, prayers, and love have been the foundation of my perseverance and success.

CERTIFICATE OF APPROVAL

Multiscale Design and Analysis of a TPMS-Based Biomimetic Femoral Stem Implant

by

Muhammad Noman Shahid

(MME233006)

THESIS EXAMINING COMMITTEE

S. No.	Examiner	Name	Organization
(a)	External Examiner	Dr. Naseem Ahmed	IST, Islamabad
(b)	Internal Examiner	Dr. M. Mahabat Khan	CUST, Islamabad
(c)	Supervisor	Dr. Shummaila Rasheed	CUST, Islamabad

Dr. Shummaila Rasheed
Thesis Supervisor
September, 2025

Dr. M. Mahabat Khan
Head
Dept. of Mechanical Engineering
September, 2025

Dr. Imtiaz Ahmad Taj
Dean
Faculty of Engineering
September, 2025

Author's Declaration

I, **Muhammad Noman Shahid** hereby state that my MS thesis titled "**Multi-scale Design and Analysis of a TPMS-Based Biomimetic Femoral Stem Implant**" is my own work and has not been submitted previously by me for taking any degree from Capital University of Science and Technology, Islamabad or anywhere else in the country/abroad.

At any time if my statement is found to be incorrect even after my graduation, the University has the right to withdraw my MS Degree.

(Muhammad Noman Shahid)

Registration No: MME233006

Plagiarism Undertaking

I solemnly declare that research work presented in this thesis titled "**Multiscale Design and Analysis of a TPMS-Based Biomimetic Femoral Stem Implant**" is solely my research work with no significant contribution from any other person. Small contribution/help wherever taken has been duly acknowledged and that complete thesis has been written by me.

I understand the zero tolerance policy of the HEC and Capital University of Science and Technology towards plagiarism. Therefore, I as an author of the above titled thesis declare that no portion of my thesis has been plagiarized and any material used as reference is properly referred/cited.

I undertake that if I am found guilty of any formal plagiarism in the above titled thesis even after award of MS Degree, the University reserves the right to withdraw/revoke my MS degree and that HEC and the University have the right to publish my name on the HEC/University website on which names of students are placed who submitted plagiarized work.

(Muhammad Noman Shahid)

Registration No: MME233006

Acknowledgement

First and foremost, I am deeply grateful to **Allah Almighty**, whose endless mercy, guidance, and blessings have carried me through every challenge and moment of uncertainty. Without His help, none of this would have been possible.

I owe everything to my **family**, whose unconditional love, prayers, and constant encouragement have been my greatest strength. A special thanks to my **uncle** and my **brother** for their quiet support and belief in me, which meant more than I can ever express.

I am also very thankful to my supportive **wife**, whose patience, understanding, and constant encouragement gave me the strength to keep going, even when things got tough. Her presence has been a source of peace and motivation throughout this journey.

I would like to sincerely thank my supervisor, **Dr. Shummaila Rasheed**, for her patience, guidance, and continuous support throughout this research. Her encouragement and advice helped me stay on track and gave me confidence during the most difficult times.

I am also grateful to our Head of Department, **Dr. Muhammad Mahabat Khan**, for allowing us access to the computational resources that were essential for completing this work.

This thesis is not just the result of my own effort, but the outcome of the love, guidance, and support I've been fortunate to receive from so many wonderful people.

(Muhammad Noman Shahid)

Abstract

Total Hip Arthroplasty (THA) is a widely adopted treatment for end-stage hip disorders, but conventional solid femoral stems often lead to stress shielding, aseptic loosening, and poor bone ingrowth due to excessive stiffness and low physiological load transfer. This study introduces a biomimetic femoral stem design based on Triply Periodic Minimal Surface (TPMS) structures to overcome these limitations. Six TPMS structures (Gyroid, Diamond, Schwarz, Lidinoid, Neovius, and SplitP) were analyzed using Asymptotic Homogenization, from which Gyroid and Lidinoid were selected at an optimal relative density of 0.3 (70% porosity) for their ability to replicate the elastic modulus of trabecular bone while maintaining high porosity for osseointegration. Finite Element Analysis (FEA) demonstrated substantial improvements over the solid stem baseline. The solid stem exhibited very low average von Mises stress (3.74 MPa), reflecting poor load transfer to surrounding bone. In contrast, the Gyroid stem showed a dramatic rise in average stress to 177.91 MPa, while the Lidinoid stem further increased average stress to 204.04 MPa. These results confirm that TPMS-based stems significantly reduce stiffness mismatch, promote physiological load sharing, and mitigate stress shielding compared to solid design. To evaluate the fluid transport performance, Computational Fluid Dynamics (CFD) was performed at inlet velocities of 0.5–0.8 mm/s. Under Newtonian flow, the Gyroid stem exhibited permeability values of 1.20×10^{-5} to $1.18 \times 10^{-5}\,\mathrm{m}^2$, with corresponding Wall Shear Stress (WSS) ranging from 0.00018–0.00028 Pa. The Lidinoid stem showed comparable permeability of 1.20×10^{-5} to $1.26 \times 10^{-5}\,\mathrm{m}^2$, with WSS values between 0.00016–0.00027 Pa. Under non-Newtonian conditions, the Gyroid and Lidinoid stems exhibited permeability values of 5.83×10^{-6} to $5.81 \times 10^{-6}\,\mathrm{m}^2$ and 5.80×10^{-6} to $5.79 \times 10^{-6}\,\mathrm{m}^2$, respectively, while WSS increased to 0.00139–0.00195 Pa for the Gyroid stem and 0.00131–0.00182 Pa for the Lidinoid stem. Surface roughness was strategically applied to the distal stem region to enhance osseointegration. This novel approach integrating optimized porosity, lattice architectures, and surface modifications presents a promising solution for enhancing the long-term performance of femoral stem implants in THA.

Contents

List of Figures

List of Tables

Abbreviations

AH	Asymptotic homogenization
CAD	Computer-aided design
CFD	Computational fluid dynamics
FEA	Finite element analysis
ISO	International Organization for Standardization
Re	Reynolds number
RVE	Representative volume element
SLM	Selective laser melting
STL	Stereolithography
THA	Total hip arthroplasty
TPMS	Triply periodic minimal surface
WSS	Wall shear stress

Symbols

μ	Dynamic viscosity	kg/(m·s)
μ_a	Apparent viscosity	kg/(m·s)
$\mu_{\min}$, $\mu_{\max}$	Minimum and maximum viscosity cutoffs	kg/(m·s)
γ	Shear rate	s^{-1}
ρ	Fluid density	kg/m^3
u	Fluid velocity	m/s
L	Characteristic length / model length	m
K	Consistency index (power-law fluid)	mPa·s^n
n	Power-law exponent	–
Δp	Pressure drop	Pa
k_0	Permeability (Newtonian)	m^2
k_n	Permeability (non-Newtonian)	m^2
Re	Reynolds number	–
E	Young's modulus	MPa
σ	Stress (generic)	MPa
σ_{vm}	von Mises stress	MPa
$u_{\max}$	Maximum deformation	mm
WSS	Wall shear stress	Pa

Chapter 1

Introduction

1.1 Overview of Femoral Anatomy

The human femur is the longest, heaviest, and strongest bone in the body, forming the main structural support of the thigh. Its proximal end includes the femoral head, which articulates with the pelvis at the acetabulum and the neck, positioned at an angle averaging approximately 125°, though this varies with age, sex, and pelvic dimensions. Two prominent bony projections, the greater and lesser trochanters, serve as critical attachment points for muscles that move the hip and knee (Figure 1.1). The shaft of the femur is slightly arched anteriorly, and at its distal end, it flares into the medial and lateral condyles, which articulate with the tibia to form the knee joint. These anatomical features are essential for both stability and mobility of the lower limb. Structurally, the femur is composed of a dense outer layer of cortical bone and an inner network of trabecular (cancellous) bone, especially in the proximal epiphysis. The trabecular bone in the femoral head and neck is uniquely organized into isotropic and orthotropic patterns, which are not found in other primates. These patterns correspond to regions of compression and tension, efficiently distributing mechanical loads during movement and weight-bearing. The femoral calcar, a dense posteromedial structure, provides additional strength to the proximal femur, withstanding forces that can exceed 1000 Newtons during activities such as standing and walking [1, 2].

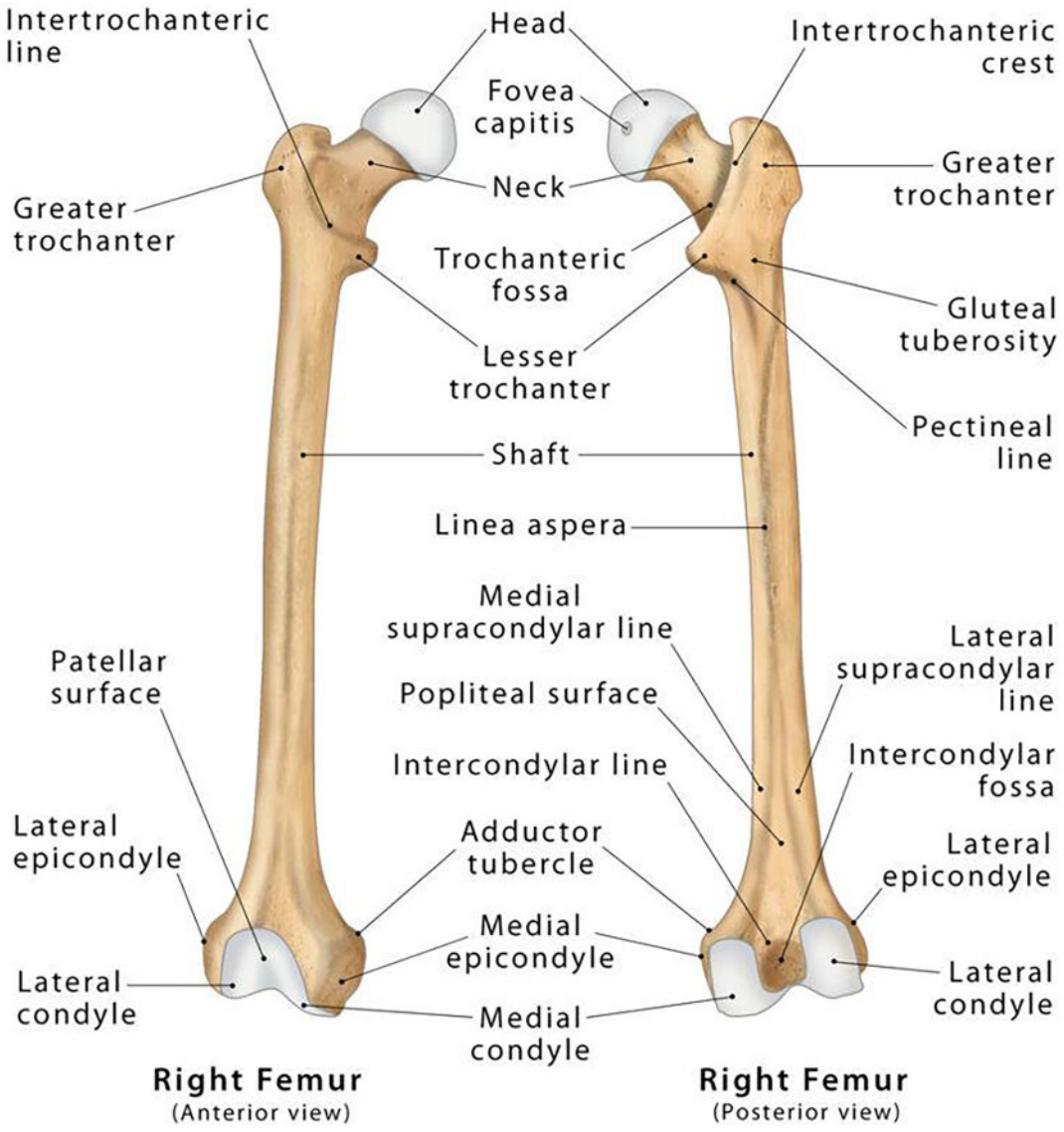

FIGURE 1.1: Anatomical features of the right femur in anterior and posterior views [3]

1.2 Anatomical Features of the Proximal Femur

The proximal femur comprises several integral parts that enable both structural support and mobility: the femoral head, neck, greater trochanter, lesser trochanter, intertrochanteric line, and crest as shown in Figure 1.2. The femoral head is roughly spherical and articulates with the acetabulum of the pelvis to form the hip joint; its smooth, cartilage-covered surface (excluding the *fovea capitis*) ensures a low-friction range of movement. The femoral neck connects the head to the shaft at an angle (about 120°–135°), providing both leverage and optimal alignment

for weight transmission. Variations in this angle have significant biomechanical implications [4].

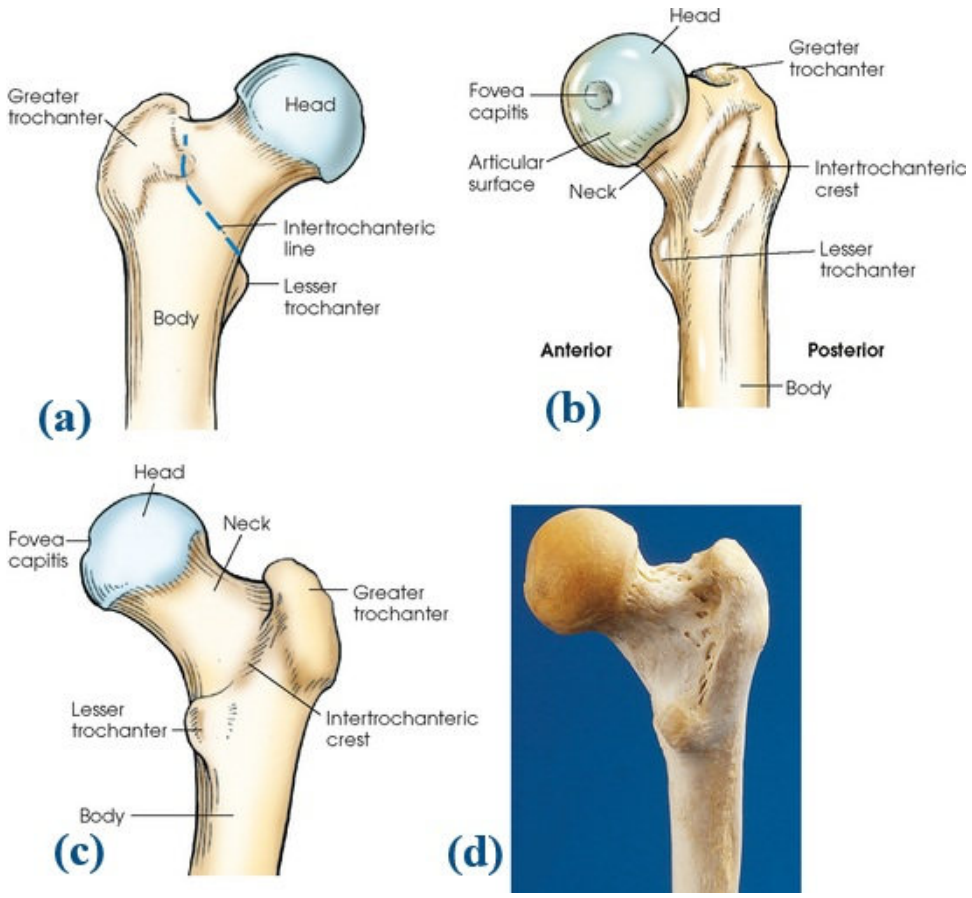

FIGURE 1.2: Proximal right femur. (a) Anterior aspect. (b) Medial aspect. The body is positioned 15 to 20 degrees posterior from head, (c) Posterior aspect. (d) Posterior aspect of right proximal human femur [5]

The greater trochanter and lesser trochanter serve as prominent bony projections for muscle attachments. The greater trochanter provides leverage and anchorage for the gluteal muscles (gluteus medius, gluteus minimus, and others), while the lesser trochanter is the attachment point for the iliopsoas muscle. Connecting these structures are the intertrochanteric line (anterior) and intertrochanteric crest (posterior), which reinforce the hip joint capsule and provide attachment for strong ligaments such as the iliofemoral ligament. Functionally, the proximal femur is critical for weight bearing and locomotion. Through its articulation at the hip, it transmits body weight from the pelvis to the lower limb, while its robust cortical and trabecular architecture absorbs and distributes mechanical loads

during movement. Its design also enables efficient muscle leverage for hip flexion, extension, abduction, and rotation [6].

1.2.1 Ligamentous Support of the Hip Joint

The proximal femur is anchored by a network of strong ligaments that reinforce hip stability through a variety of movements. The iliofemoral ligament, also known as the "Y ligament of Bigelow," extends from the anterior inferior iliac spine and acetabular rim to the intertrochanteric line of the femur; it is the strongest ligament of the body and plays a key role in preventing hyperextension while maintaining upright posture, even without muscular effort. Just inferior and medial to this, the pubofemoral ligament spans from the pubic bone to the lower intertrochanteric line, reinforcing the anterior–inferior capsule and restricting excessive abduction and extension. Posteriorly, the ischiofemoral ligament arises from the ischial part of the acetabular rim, spirals to the base of the greater trochanter, and limits extension while stabilizing the joint's back side. Within the joint capsule lies the ligamentum teres, which connects the acetabular fossa to the fovea capitis femoris; although it does not significantly constrain movement, it carries a small artery critical for blood supply to the femoral head in early life. Together, these ligaments ensure that the proximal femur remains firmly positioned within the acetabulum throughout the hips' range of motion [7].

1.2.2 Critical Load-Bearing Regions of the Proximal Femur

In the proximal femur, the trabecular network is organized along principal stress trajectories and is typically divided into four major groups; primary compressive, primary tensile, secondary compressive, and secondary tensile trabeculae as shown in Figure 1.3. The primary compressive trabeculae form a vertical, triangular-like pattern extending from the medial cortex through the femoral neck, efficiently

transmitting load from the femoral head toward the shaft. By contrast, the primary tensile trabeculae trace an arcuate path from the greater trochanter across the superior cortex of the neck and head, resisting tensile forces. Secondary compressive branches emanate from the calcar and lesser trochanter toward the greater trochanter, offering supplemental reinforcement under compressive stress, while secondary tensile elements further reinforce the structure under tensile stress. The region of intersection among these systems, Ward's triangle, represents an area of reduced trabecular density where compression and tension forces balance each other out [8].

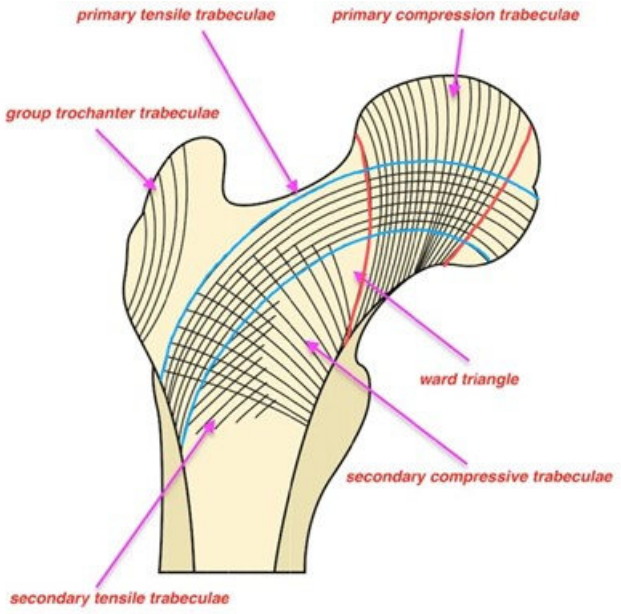

FIGURE 1.3: Regional division of the femoral trabecular bone based on principal stress directions

1.2.3 Fractures, Pathologies, and Surgical Indications of the Proximal Femur

The proximal femur commonly experiences several forms of structural compromise. Fractures, including femoral neck (subcapital, mid cervical, basicervical), intertrochanteric, and subtrochanteric types, are especially prevalent in older adults and are typically categorized by classification systems such as Garden, Pauwels,

and AO [9]. In addition to trauma-induced fractures, degenerative wear mechanisms, such as osteoarthritis, rheumatoid arthritis, and osteonecrosis, gradually deteriorate the cartilage and subchondral bone of the femoral head and acetabulum, leading to pain, stiffness, and joint dysfunction. Pathological conditions, including bone tumors and metastatic lesions, cause progressive weakening and structural loss in the proximal femur, increasing the risk of pathological fracture or the need for complex reconstruction [10].

The femoral neck and intertrochanteric region are among the most frequently compromised anatomical areas, particularly due to their biomechanical vulnerability and reduced vascular supply, making displaced femoral neck fractures, especially Garden type III and IV, poor candidates for fixation and more appropriate for prosthetic replacement. Indications for hip arthroplasty (total or partial) typically include advanced degenerative or necrotic conditions unresponsive to conservative management, femoral neck fractures with high necrosis risk, pathological fractures, non unions or malunions, infection, or malignancy involving the proximal femur. In such stages, where pain, functional loss, compromised bone integrity, or risk of failure of fixation are prominent, the use of implants like total hip replacements, hemiarthroplasty, or modular proximal femoral prostheses becomes unavoidable for restoring structural stability and preserving patient mobility.

1.3 Global Statistics of Total Hip Arthroplasty (THA)

Despite their strength, bones remain vulnerable to permanent damage from trauma or disease when injuries surpass their self-repair capacity. Osteoarthritis (OA), one of the most prevalent musculoskeletal disorders, predominantly affects the hands, knees, and hips in individuals aged 60 and above [11]. Globally, an estimated 250 million people suffer from OA, with rising prevalence linked to an aging population [13]. In addition to degenerative diseases, bone fractures pose a significant risk, particularly among the elderly. Both OA and fractures severely restrict mobility

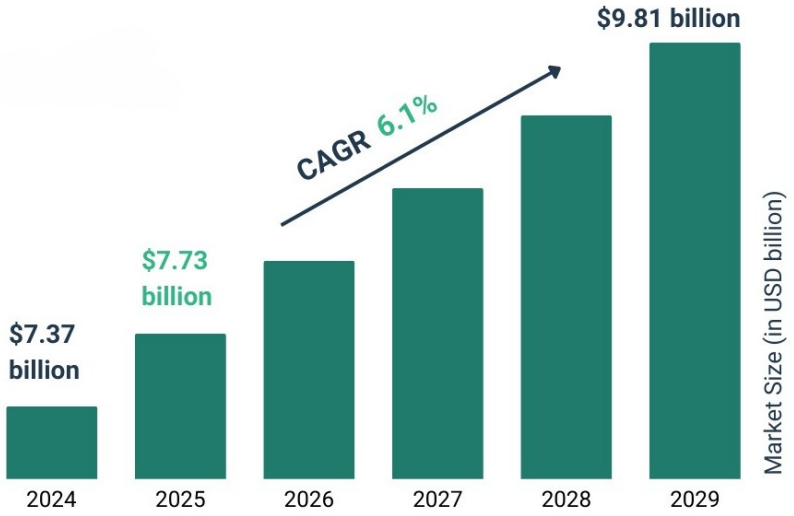

FIGURE 1.4: Global hip replacement market size in 2025 [12]

and impose substantial economic burdens on patients and their families. Total hip arthroplasty (THA) has seen substantial global growth driven by aging populations, rising osteoarthritis prevalence, and advancements in surgical outcomes. Between 2000 and 2019, THA volumes increased by 177% worldwide [14]. Global hip replacement market size in 2025 is shown in Figure 1.4. Implant survival rates improved from 85% (2009) to 90% (2021) over 15 years. Cementless implants dominate in regions like Italy (96%), while Sweden prefers cemented THA (50%) [15]. In 2023, the global hip replacement market was valued at USD 7.72 billion and is projected to expand from USD 8.05 billion in 2024 to USD 11.59 billion by 2032, growing at a compound annual growth rate (CAGR) of 4.7% over the forecast period. North America held the largest market share in 2023, accounting for 34.33% of the global market [16].

1.4 Evolution of Femoral Stem Design

The design of femoral stems in total hip arthroplasty has evolved from simple, cemented, monoblock stems in the 1960s—such as the Charnley stem—to advanced, modular, and bone-preserving implants used today. Early designs relied on cement fixation and basic geometries, but issues like loosening and stress shielding led to innovations in the 1980s and 1990s, including the use of titanium alloys, porous

and hydroxyapatite coatings, and uncemented, press-fit stems to encourage biological fixation. In recent decades, the focus has shifted to shorter stems, modularity for anatomical customization, and minimally invasive techniques to preserve bone and improve patient outcomes. Each phase of development reflects a response to clinical challenges and a drive for better longevity, stability, and function [17, 18].

Bone resorption, a common complication after THA, arises from factors such as osteolysis and stress shielding. Osteolysis occurs when macrophage-induced osteoclast activity is triggered by wear particles from loose implants. Stress shielding results from the stiffness mismatch between the implant and bone, causing mechanical load to concentrate on the implant and reducing bone stimulation. According to Wolf's Law, diminished stress leads to bone remodeling, increasing porosity and decreasing mass and density. Mitigating stress shielding involves reducing implant stiffness through optimized design, including adjustments to femoral head/neck dimensions, offset, neck angle, stem geometry, and length to better match host bone properties [19]. An overview of femoral stem design classifications is summarized in Table 1.1.

Throughout the past century, the advancement of materials used in modern hip stems has followed a well-defined progression, as illustrated in Table 1.2. Early clinical use centred on cobalt-chromium "Vitallium" hemiarthroplasty heads developed by Moore and Thompson in the late 1930s and early 1940s. In the 1950s and 1960s polished stainless steel stems with acrylic cement defined the first reliable total hip systems under Charnley. From the 1970s titanium alloys rose to prominence for cementless fixation because of lower modulus and strong biocompatibility. The 1980s introduced porous coatings and the first hydroxyapatite coatings to accelerate bone fixation. The 1990s brought wider adoption of hydroxyapatite-coated titanium stems, the arrival of porous tantalum for highly porous fixation, and early exploration of polymer composites and beta-titanium. Since 2010, additively manufactured titanium with controlled lattice porosity has enabled patient-specific designs and stiffness tuning, while long-term results continue to accumulate for hydroxyapatite-coated stems.

TABLE 1.1: Classification Systems of Femoral Stem Designs [20–22]

Authors	**Year**	**Categories**	**Description**	**Rationale/Basis of Classification**
McTighe et al.	2013	Head stabilized	Resurfacing implants.	Assessment of length and method of achieving primary stability of the stem.
		Neck stabilized	Short curved neck-sparing stems, and standard-length stems preserving the femoral neck but engaging the neck, metaphysis, and diaphysis.	
		Metaphyseal stabilized	Short metaphyseal stems including anatomical, straight, and tapered designs.	
		Conventional (metaphyseal/diaphyseal) stabilized	Conventional stems engaging both metaphysis and diaphysis.	
Feyen & Shimmin	2014	Type I	Resurfacing.	Assessment of the osteotomy level for neck resection and implant fixation principles.
		Type II	Mid-head resection stems, characterized by osteotomy through the mid-femoral head.	

(Continued on next page)

Authors	Year	Categories	Description	Rationale/Basis of Classification
		Type III	Short stems with subcapital (IIIA) or standard (IIIB) osteotomy.	
		Type IV	Traditional stems.	
		Type V	Diaphyseal fixation stems.	
Van Oldenrijk et al.	2014	Collum	Conical or cylindrical ultra-short stems, with complete anchorage in the femoral neck.	Assessment of the osteotomy level for neck resection and implant fixation principles.
		Partial collum	Partial femoral neck-sparing curved designs.	
		Trochanter-sparing	Trochanter-sparing but not neck-sparing, and shortened tapered stems.	
Khanuja et al.	2014	Tapered proximal fixation (Single wedge)	Narrows medially-laterally. Proximally coated. Flat stem, thin in anterior-posterior plane.	Assessment of location of loading and implant fixation principles.
		Tapered proximal fixation (Tapered, round)	Rounded tapered conical stem with porous coating at proximal two-thirds.Rounded tapered conical stem with porous coating at proximal two-thirds.	

(Continued on next page)

Authors	Year	Categories	Description	Rationale/Basis of Classification
		Distally fixed (Cylindrical, fully coated)	Extensive porous coating. Proximal collar to enhance proximal bone loading and axial stability.	
		Type I (Femoral neck fixation)	Stems from IA to IC based on geometry.	
		Type II (Calcar loading)	Stems from IIA to IID based on geometry.	
		Type III (Calcar loading with lateral flare)	Stems with lateral flare.	
		Type IV (Shortened tapered)	Shortened tapered stems.	
Falez et al.	2015	Collum	Conical or cylindrical ultra-short stems, with complete anchorage in the femoral neck.	Assessment of the osteotomy level for neck resection and implant fixation principles.
		Partial collum	Partial femoral neck-sparing curved designs. Partial femoral neck-sparing curved designs.	

(Continued on next page)

Authors	Year	Categories	Description	Rationale/Basis of Classification
		Trochanter-sparing	Trochanter-sparing but not neck-sparing, and shortened tapered stems.	
		Trochanter-harming	Short stems interrupting the circumferential integrity of the femoral neck and violating the trochanteric region.	
Cortis et al.	2022	Type I (Single wedge)	Anterior-posterior direction ending with a spherical distal edge. 130° neck-shaft angle, vertically shaped in the lateral portion.	Assessment of Stress Shielding and Structural Integrity
		Type II (Single wedge with collar)	Proximal collar with a prominent semi-circular disc shape in the medial portion of the sagittal plane.	
		Type III (Single anatomical wedge)	Deeper curvature and narrow wedge.	
Stadler et al.	2025	Neck-resecting vs partially neck-sparing (cementless short stems)	Retrospective study: 345 THAs; Group A: Fitmore neck-resecting (160), Group B: ANA NOVA neck-sparing (185)	Templating adherence: Group A 26.9%, Group B 36.2%; improved planning accuracy in neck-sparing design

TABLE 1.2: Historical evolution of femoral stem materials, their advantages, and limitations across different eras.

Era	Stem material used or introduced	Main advantages	Main limitations	Refs
1930 to 1939	Cobalt chromium molybdenum Vitallium in early hemiarthroplasty	Better corrosion resistance than earlier metals, acceptable biocompatibility for the time	Very high stiffness and rudimentary fixation concepts led to variable clinical results	[23, 24]
1940 to 1949	Moore style cobalt chromium stems for hemiarthroplasty; early stainless steel stems appear	Strong alloy, manufacturing reliability improves	Loosening common, fixation and biomechanics not yet optimized	[24, 25]
1950 to 1959	Stainless steel 316L stems in growing use	Widely available, high strength, polishable for cemented designs	Reports of corrosion and occasional fracture in some series	[25, 26]
1960 to 1969	Charnley style polished stainless steel stems with acrylic cement	Reliable fixation concept that enables consistent total hip arthroplasty results	Cement related issues and long term wear at the bearing couple	[25–27]
1970 to 1979	Titanium alloys introduced for femoral stems, especially Ti6Al4V, while stainless steel and cobalt chromium continue	Lower modulus than steel or cobalt chromium, excellent biocompatibility for cementless concepts	Poor sliding wear, requires suitable head and cup combinations and surface finishes	[28, 29]
1980 to 1989	Cementless stems with porous coated titanium or cobalt chromium; first reports of hydroxyapatite coating	Biological fixation through bone ingrowth or ongrowth; faster early stability with hydroxyapatite	Coating adhesion and technique sensitivity vary between designs	[29, 30]

(Continued on next page)

Era	Stem material used or introduced	Main advantages	Main limitations	Refs
1990 to 1999	Hydroxyapatite coated titanium stems become common; porous tantalum introduced late in the decade; early polymer composite work with CFR PEEK; research on beta titanium alloys	Faster bone fixation with hydroxyapatite, high porosity surfaces closer to bone stiffness, exploration of lower modulus alloys	Cost and brittleness concerns at very high porosity, mixed outcomes with composites, limited long term beta titanium stem data	[26, 27]
2000 to 2009	Titanium alloy cementless stems dominate; porous tantalum adopted especially in revisions	Durable osseointegration and good primary stability in difficult cases	Stiffness mismatch persists for some designs, tantalum cost considerations	[27, 29]
2010 to 2019	Additively manufactured Ti6Al4V lattices for porous coatings and custom stems; continued study of beta titanium families	Tailored porosity for bone ingrowth, potential to tune stiffness toward bone	Process control and fatigue performance are critical, long term clinical evidence still maturing	[28, 31]
2020 to 2025	Continued dominance of titanium alloys with additively manufactured lattices and topology optimization; ongoing work on low modulus titanium systems; hydroxyapatite variants	Design optimization, patient specific options, improved early fixation	Need for rigorous quality control and longer follow up across designs	[24, 32]

1.5 Lattice Structures in Biomedical Applications

Lattice structures are categorized by their geometric configurations, primarily divided into two types: strut-based and surface-based designs as shown in Figure 1.5. Each type exhibits distinct mechanical properties and energy absorption capabilities, making them suitable for specific applications [33].

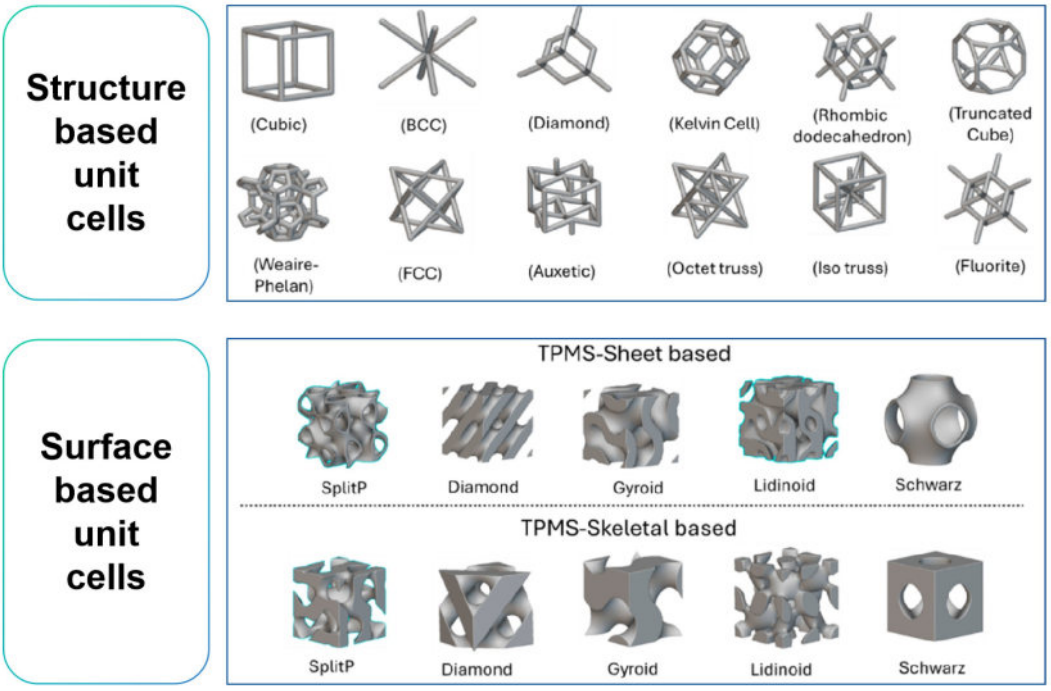

FIGURE 1.5: Classification of lattice structures based on structures and surfaces [33]

Biomimetic scaffold design has emerged as a promising approach in tissue engineering, with Triply Periodic Minimal Surfaces (TPMSs) recently gaining significant interest for the fabrication of porous biomimetic scaffolds. Initially introduced by Schwarz in the 19th century, TPMS are 3D patterns that minimize local surface area while maintaining periodicity. TPMS lattices are classified into two types: sheet-based and skeleton-based. Their absence of nodal points and curvature discontinuities mitigates stress concentrations and improves mechanical strength [34]. Compared to conventional lattice-based structures like strut-based lattices, TPMS-based scaffolds exhibit superior properties, including a high surface-area-to-volume ratio, reduced stress concentration, and enhanced permeability, all of which promote improved cell adhesion, migration, and proliferation [35, 36].

Building on these properties, TPMS architectures can be used in two ways to tune implant mechanics and transport to host bone. A uniform porosity design applies one pore size and one volume fraction throughout the stem, which gives a single effective stiffness and permeability. This is simple to design and manufacture and it supports bone ingrowth, yet it cannot reproduce the natural change in stiffness from the proximal to the distal femur, so the trade off between stability and stress shielding may persist. A graded porosity design varies unit cell size, strut thickness, or volume fraction along the stem to create spatial changes in stiffness and permeability. Higher porosity in the proximal region lowers stiffness to share load with bone and promote ingrowth, while lower porosity in the distal region preserves strength and primary stability. Grading can also adjust pore size to aid fluid flow and early vascularization without sacrificing structural safety. The main challenges are process control, fatigue resistance at high porosity, and consistent surface quality for reliable biological fixation.

1.6 Conventional Manufacturing Techniques

Conventional manufacturing techniques for femoral stems primarily include casting, forging, and machining. Historically, femoral stems were produced as monoblock components using materials such as stainless steel, cobalt-chromium alloys, or titanium alloys. Casting involves pouring molten metal into a mold shaped like the stem, allowing it to solidify before undergoing various finishing processes. Forging, on the other hand, uses mechanical force to shape heated metal billets into the desired form, resulting in improved mechanical properties due to grain alignment. Machining, often performed on advanced multi-axis CNC machines, is then used to achieve precise dimensions and surface finishes, particularly for titanium alloy stems [37].

Despite their widespread use, these conventional techniques present several limitations. One of the primary challenges is the inability to create complex internal

geometries or controlled porosity within the stem. Traditional methods are restricted to producing dense, solid implants, which can lead to a mismatch in stiffness between the implant and the surrounding bone. This stiffness mismatch often results in stress shielding, where the implant bears most of the load, causing bone resorption and potentially leading to implant loosening over time. Additionally, the lack of interconnected pores in conventionally manufactured stems limits bone ingrowth and biological fixation, reducing the potential for long-term secondary stability. Another limitation is the difficulty in customizing implants for individual patients. Conventional manufacturing is typically suited for mass production of standard sizes and shapes, making it challenging to accommodate anatomical variations or specific clinical requirements. Furthermore, processes like casting and forging can introduce defects such as porosity, inclusions, or residual stresses, which may compromise the mechanical integrity of the implant. Machining complex features or undercuts is also time-consuming and costly, further restricting design flexibility [38].

1.7 Additive Manufacturing

Additive Manufacturing (AM) and metal 3D printing technologies enable innovative approaches to femoral stem design optimization. These techniques allow not only for weight reduction through internal geometric modifications, but also for enhanced functional performance by strategically engineering the implant's internal architecture. Researchers have demonstrated that mechanical properties can be precisely tuned by incorporating bio-inspired features such as porous structures [39, 40], lattice frameworks [41, 42], or trabecular patterns [43]. Metal AM techniques for manufacturing of implants are illustrated in Figure 1.6.

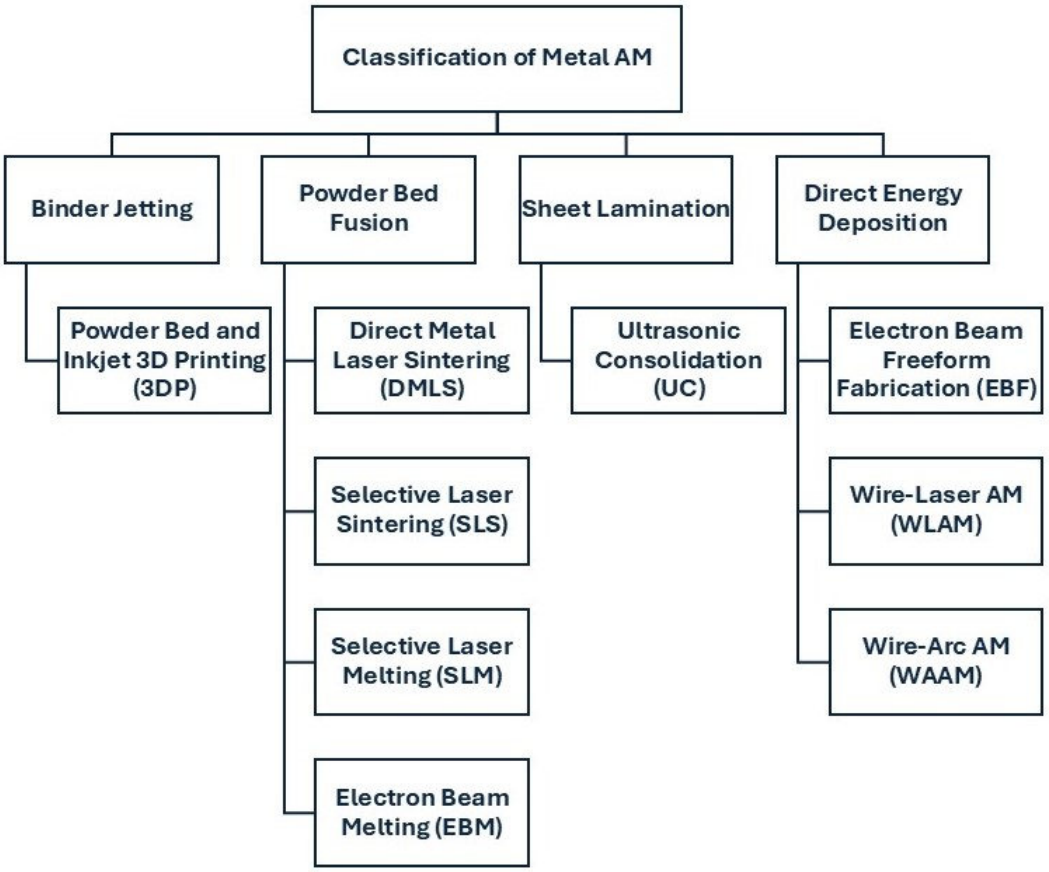

FIGURE 1.6: Metal AM techniques for manufacturing of implants [44]

1.8 Surface Roughness for Osseointegration

Surface roughness significantly improves osseointegration by enhancing bone-to-implant contact and promoting osteoblast activity. Rough implant surfaces increase the surface area for bone cells to adhere, migrate, and differentiate, leading to stronger biological fixation compared to smooth surfaces. Studies show that moderately rough surfaces, typically with microroughness in the range of 1–10 microns, optimize osteoblast differentiation and bone interlocking, accelerating the healing process. Surface treatments such as blasting, acid etching, and oxidation create these micro- and nano-scale irregularities, which improve protein adsorption and cell attachment. While rough surfaces improve secondary stability through better bone integration, they do not significantly affect primary mechanical stability. Therefore, roughened surfaces facilitate faster and more reliable osseointegration by providing a favorable environment for bone growth and implant anchorage [45, 46].

Current femoral stems still fall short of durable fixation and physiologic load sharing. Fully solid metal stems are much stiffer than trabecular bone, so load shifts away from the proximal femur, bone resorbs, and the interface weakens, which promotes micromotion and aseptic loosening over time. Uniform porous stems were proposed as a fix, but one porosity level cannot reproduce the natural gradients in stiffness and architecture, so they struggle to give both strength and bone ingrowth where each is needed. Many designs also do not give equal priority to permeability and surface biology. Without controlled pathways for fluid and vessels, and without surfaces that drive rapid, stable osseointegration, ingrowth is patchy and slow. In short, current stems do not balance three needs at once: structural safety under load, transport for tissue viability, and surface features for firm biological fixation.

1.9 Problem Statement

Conventional solid metallic stems exhibit excessive stiffness, causing bone resorption, while uniform porous designs lack the graded mechanical properties needed to match natural bone behavior. Furthermore, existing implants do not optimally balance structural integrity, permeability for vascularization, and surface characteristics for biological fixation. Although additive manufacturing enables complex geometries, the systematic design of functionally graded femoral stems, integrating optimized porosity, lattice architectures, and surface modifications, remains underexplored. Through computational modeling, this work aims to overcome the limitations of current designs and provide a more durable and biologically compatible solution for hip arthroplasty.

1.10 Research Objectives

The research objectives are given below:

- To design a functionally graded femoral stem incorporating porous and solid regions for improved biomechanical performance.
- To identify optimal lattice structures and porosity levels through homogenization analysis for matching bone-like mechanical properties.
- To perform finite element analysis to evaluate stress distribution and deformation under physiological loading.
- To assess permeability of the porous region using computational fluid dynamics for evaluating bone ingrowth potential.

1.11 Thesis Organization

This thesis is structured into five main chapters, each addressing a critical stage of the research, design, and analysis process for developing a functionally graded femoral stem for hip arthroplasty. Chapter 1 provides the introduction, presenting the anatomical background, clinical relevance, and engineering challenges associated with femoral implants. It also outlines the evolution of femoral stem design, the limitations of conventional approaches, and the potential of lattice structures, before concluding with the research problem and objectives. Chapter 2 reviews the existing literature, covering femoral anatomy, biomechanics, bone remodeling, and implant design strategies, with particular emphasis on porous structures. It also examines key studies on finite element analysis, permeability, surface roughness, and highlights the need for functionally graded implants. Chapter 3 details the methodology, describing the computational framework and modeling techniques employed in this research. This includes asymptotic homogenization, CAD modeling, TPMS integration, application of surface roughness, and the simulation setups for both finite element and CFD analysis. Chapter 4 presents the results and discussion, reporting the findings from FEA and CFD simulations and comparing different TPMS structures in terms of mechanical behavior, stress distribution, and permeability, while also interpreting the implications of these results for implant design and biological performance. Finally, Chapter 5 concludes the work by

summarizing the main findings, emphasizing the novelty of the proposed design, and suggesting directions for future experimental validation and clinical application of the developed implant concept.

Chapter 2

Literature Review

2.1 Anatomical and Biomechanical Basis of the Proximal Femur

The proximal femur comprises a spherical femoral head, a cylindrical femoral neck, and two prominent muscle attachment sites - the quadrilateral greater trochanter and conical lesser trochanter. In healthy hips, articular cartilage covers both the femoral head and acetabulum, enabling low-friction movement while providing critical shock absorption. The joint's stability is maintained by three principal ligaments: the iliofemoral ligament (extending from ilium to femur, serving as the primary stabilizer), the ischiofemoral ligament (connecting the ischium to the posterior femur), and the pubofemoral ligament (linking the pubis to the femur while blending with the iliofemoral ligament). This complex anatomical arrangement ensures both mobility and structural integrity of the hip joint [47].

The success of joint arthroplasty critically depends on the quality and quantity of host bone tissue. Effective evaluation of orthopedic prostheses requires comprehensive understanding of bone biomechanics and physiology. As the primary component of the musculoskeletal system, bones perform essential functions including weight-bearing, load resistance, movement facilitation, and organ protection. Additionally, they play vital roles in calcium homeostasis and hematopoiesis. Bone

tissue consists of a composite matrix containing both organic (primarily type I collagen, providing tensile strength and structural framework) and inorganic components (hydroxyapatite crystals, predominantly calcium phosphate, conferring compressive strength). The human skeleton comprises two distinct bone types differentiated by density and porosity: cortical bone (low porosity, <30%) predominates in high-stress regions, while cancellous (trabecular) bone (higher porosity, >30%) occurs in lower-stress areas. This structural adaptation optimizes mechanical performance while minimizing weight [48].

The distinction between cortical and trabecular bone microarchitecture reveals critical differences in porosity, stiffness, and strength that significantly influence overall bone integrity [49]. Cortical bone, which forms the outer layer of the femur, is characterized by a dense structure and lower porosity compared to trabecular bone, which is more porous and located at the ends of long bones, including the femur. For example, Bittner-Frank et al. [50] highlight that cortical bone typically exhibits greater thickness than trabecular bone, resulting in relatively high stiffness and strength. On the other hand, trabecular bone is more susceptible to changes caused by physiological or pathological conditions, as indicated by reduced trabecular number and trabecular thickness, which negatively affect its mechanical properties [51]. Notably, studies have shown that microarchitectural deficits in trabecular bone can significantly impair mechanical performance under load-bearing conditions [52, 53].

2.2 Bone Remodeling Theory

Bone remodeling is a continuous, dynamic process in which old or damaged bone is resorbed by osteoclasts and replaced by new bone formed by osteoblasts, maintaining skeletal integrity and adapting bone architecture to mechanical and metabolic demands. The remodeling cycle involves several phases: activation (triggered by mechanical damage or osteocyte apoptosis), resorption (osteoclast-mediated bone breakdown), reversal (preparation of the resorbed surface by reversal cells), formation (osteoblast deposition of new bone matrix), and resting, during which the

bone surface is covered by lining cells until the next remodeling cycle. This tightly coupled process occurs within basic multicellular units (BMUs), which coordinate the cellular activities to renew bone without altering its shape [54].

Under physiological loads, bone remodeling is regulated by mechanobiological signals sensed primarily by osteocytes, which respond to strain and microdamage by modulating osteoclast and osteoblast activity to optimize bone strength and repair microdamage. Mechanical loading stimulates bone formation in high-strain regions, while disuse or reduced loading leads to bone resorption, reflecting Wolff's law of bone adaptation. Thus, remodeling balances local mechanical stimuli with systemic hormonal and biochemical factors (e.g., parathyroid hormone, growth factors) to maintain bone mass and structural competence. This process ensures that bone architecture adapts dynamically to changing mechanical environments, preserving skeletal function and minimizing fracture risk [55, 56].

2.3 Solid to Porous Femoral Stem Design: Finite Element Studies

According to ISO 5832, orthopedic metallic implants are made from stainless steel, cobalt-chromium (Co-Cr) alloys, or titanium alloys. Titanium alloys are the most commonly used due to its biocompatibility, corrosion resistance, ductility, and lower elastic modulus than steel [57]. However, even titanium alloys have 5–10 times higher stiffness than bone, reducing load transfer to surrounding bone. According to Wolff's Law, bone adapts to mechanical stress by remodeling, strengthening under high stress and weakening under low stress [58]. This stiffness mismatch between solid metallic implant and bone can cause stress shielding, resulting in bone resorption near the prosthesis due to reduced load transfer, as well as distal femoral cortical hypertrophy (DFCH) from increased strain at the stem tip. These biomechanical complications raise the risk of implant failure, including loosening or periprosthetic fracture, which are critical concerns in hip arthroplasty [59].

A promising approach to overcome the limitations of solid metallic implants is the use of lattice structures as substitutes. Lattice structures can be broadly classified into two categories: strut-based and surface-based designs. Strut-based lattices, the more conventional type, consist of repeating units formed by interconnected beams or struts. However, their design flexibility is limited to adjusting strut length and radius, restricting property optimization. Additionally, the abrupt connections between cells create stress concentrations, which can compromise structural integrity. In contrast, emerging research focuses on surface-based lattices derived from TPMS, offering superior design versatility and smoother stress distribution compared to traditional strut-based approaches [60]. To enhance the fatigue resistance of TPMS-based scaffolds, Liu et al. [61] proposed a combined post-treatment of hot isostatic pressing (HIP) and electropolishing (ELP). They investigated two Ti6Al4V scaffolds fabricated via electron beam melting: a stretching-dominated diamond (AD) and a bending-dominated gyroid (IG), both at 20% relative density. Fatigue tests revealed that untreated IG and AD had fatigue ratios of 0.11 and 0.59, respectively, which improved to 0.26 and 0.69 after HIP+ELP. Finite element analysis and microstructural characterization demonstrated that topological design had the greatest influence on fatigue performance, surpassing surface quality and defect reduction. Furthermore, Rezapourian et al. [62] performed the investigation of SLM Ti6Al4V Split-P TPMS lattices, examining two cell morphologies (CM) at five relative densities (RD). SEM analysis confirmed print fidelity, while mechanical testing revealed stretch-dominated behavior with elastic modulus (1.50–3.50 GPa), yield strength (57.95–152.74 MPa), and ultimate strength (93–170 MPa) tunable via RD and CM. The lattices exhibited load-bearing capacities of 0.04–0.17, energy absorption (22–61 MJ/m^3), and plateau stress (30–63 MPa), aligning with trabecular/cortical bone properties. Finite element analysis and homogenization highlighted isotropic behavior for zero-isovalue designs and anisotropy for non-zero variants. The study establishes Split-P's unique potential for bone implants, leveraging its high surface area-to-volume ratio and Gibson-Ashby-compliant mechanical scalability.

Corona-Castuera et al. [63] developed a partial hip implant using tomography data and gyroid/double gyroid TPMS structures to match patient bone density.

Under uniaxial compression, the gyroid outperformed the double gyroid in mimicking bone mechanics. The prosthesis, fabricated via SLM with 17-4 PH stainless steel, was lightweight (72 g) compared to solid designs. Patrik et al. [64] addressed stress shielding in hip implants by developing a computationally efficient topology optimization framework for patient-specific lattice endoprostheses. Using homogenized FE models, they achieved 81% and 66% reductions in stress deviation root mean square error (vs. physiological bone) in Gruen zones 6-7 compared to conventional implants. Results of different simulation methods are shown in Figure 2.1. Furthermore, Moghariya and Gurrala [65] investigated TPMS structures for

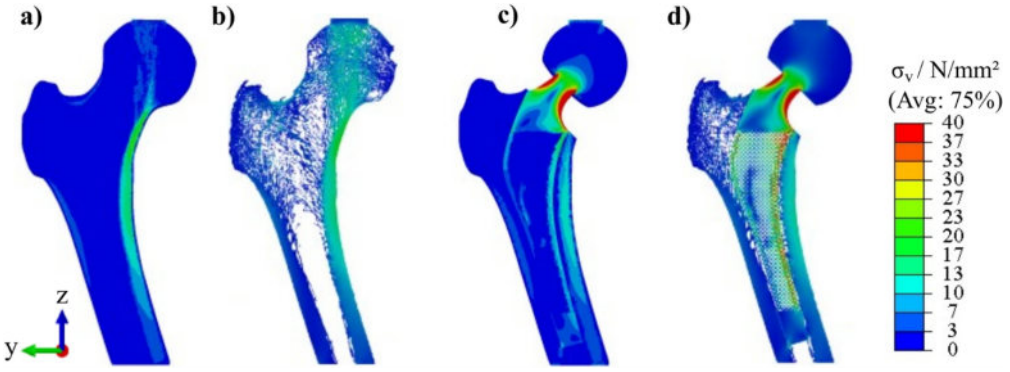

FIGURE 2.1: Results of the different simulation methods, (a) physiological hFEA, (b) physiological µFEA, (c) optimized-THA hFEA, (d) optimized-THA µFEA.

improving total hip arthroplasty outcomes through computational analysis. Using patient-specific femur models derived from CT scans and finite element analysis (ISO 7206-4:2010), they compared Gyroid and Split-P porous implants against conventional solid designs, as shown in Figure 2.2. Their results demonstrated that the Gyroid structure outperformed others, showing 28% weight reduction and 70% porosity while maintaining safe stress levels, in contrast to Split-P's higher stress concentrations. The study concluded that Gyroid-based implants offer optimal balance of mechanical performance and osteointegration potential, presenting a promising solution to address stress shielding and bone regeneration challenges in hip replacements.

Salaha et al. [66] investigated the design of a porous hip implant to enhance osteointegration, medullary revascularization, and blood circulation. Through topology optimization and material selection, they developed lightweight implant

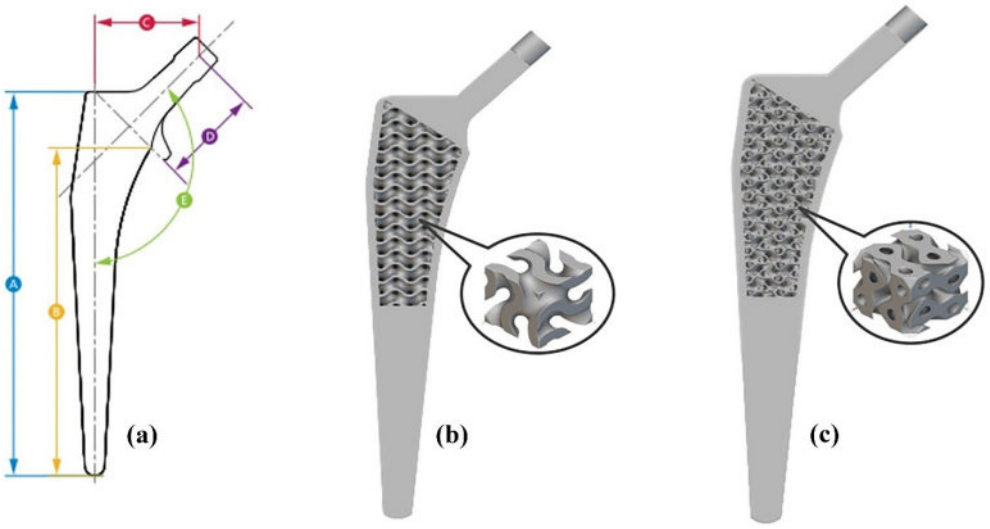

FIGURE 2.2: Design of implants (a) Solid implant (b) Gyroid based implant (c) SplitP based implant

designs featuring Gyroid and Voronoi lattice structures, alongside a solid control model (Figure 2.3), using SolidWorks and nTopology (v2.31). Under simulated stance-phase loading conditions (x = 320 N, y = 170 N, z = 2850 N), finite element analysis in Marc Mentat software revealed that the titanium-based Voronoi lattice exhibited the lowest von Mises stress (313.96 MPa) and displacement (1.50 mm), maintaining mechanical integrity.

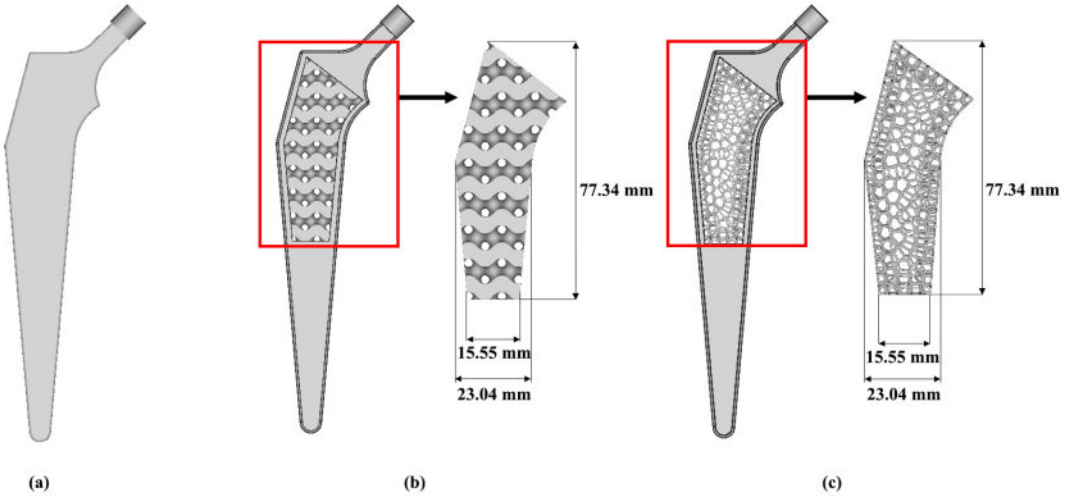

FIGURE 2.3: Hip implants model for (a) Solid (b) Gyroid and (c) Voronoi design [66]

Additionally, Rahmat et al. [67] evaluated the performance of femoral stems with triply periodic minimal surface (TPMS) structures (IWP and Gyroid) using FEA, focusing on stress shielding and bone-implant micromotion. Their study compared

homogeneous and axially graded designs, IAGS (increasing volume fraction) and DAGS (decreasing volume fraction), to assess their influence on stress transfer and bone resorption. Results indicated that axial stiffness directly affected stress shielding, with an inverse correlation to micromotion. The IWP structure exhibited higher bone resorption than Gyroid at identical volume fractions, while axially graded stems (particularly DAGS-IWP and DAGS-Gyroid) improved proximal-medial stress transfer. Notably, high-porosity homogeneous stems (80% IWP, 70% Gyroid) and DAGS designs minimized stress shielding and maintained micromotion within acceptable ranges for bone ingrowth, suggesting their potential for optimizing femoral stem performance. Furthermore, Bruno et al. [68] developed a diamond cubic lattice-based porous femoral stem using Ti-6Al-4V alloy via laser powder-bed fusion to reduce stiffness while promoting osseointegration. The pore geometry was optimized to simultaneously satisfy biomechanical strength requirements and bone ingrowth criteria as shown in Figure 2.4. Through ISO 7206-4 standard static testing validated by digital image correlation, the porous stem demonstrated 31% reduced stiffness compared to its solid counterpart. Numerical models showed strong correlation with experimental displacement and strain field data, confirming model validity. The study further established that diamond lattice architectures exhibited favorable surface-to-volume and strength-to-stiffness ratios, suggesting their efficacy as biomimetic structures for load-bearing orthopedic applications.

Naghavi et al. [69] proposed a low-stiffness porous Ti6Al4V hip prosthesis fabricated via SLM to mitigate stress shielding and bone resorption post-implantation. Through combined FEA and in vitro quasi-physiological testing, the porous implant's performance was compared against a solid control. Compression tests revealed stiffness values of 2.15 kN/mm (porous) and 2.76 kN/mm (solid), while fatigue simulations confirmed a safety factor >2 under dynamic loading. At 2,300 N compressive load, peak von Mises stresses (112 MPa at medial neck; 290 MPa at distal restriction) remained below the endurance limit of 3D-printed Ti6Al4V (375 MPa), as shown in Figure 2.5. The porous design reduced stress shielding by 70% and bone mass loss by 60%, achieving more physiological stress distribution. By optimizing strut thickness, the study demonstrated the porous stem's potential as

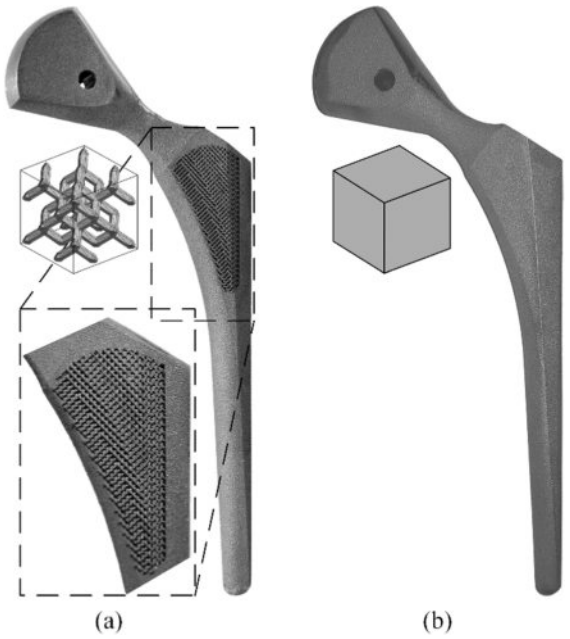

FIGURE 2.4: (a) Stem body filled with the diamond cubic porous structure (b) fully dense stem [68]

a superior alternative to conventional solid implants. Furthermore, Kladovasilakis et al. [70] explored the application of bioinspired lattice structures for the topological optimization of Inconel 718 orthopedic hip implants. Through finite element analysis (FEA) under in vivo loading conditions, three distinct lattice architectures were evaluated, with functional gradation employed to optimize cellular material distribution. The study demonstrated that functionally graded lattice structures achieved optimal stress distribution while simultaneously reducing implant weight and increasing porosity. Remarkably, the optimized design withstood loads up to twice typical in vivo conditions, maintaining mechanical integrity. These findings suggest that functionally graded lattice structures present a viable and potentially superior alternative to conventional solid hip implants, offering improved performance without compromising structural stability. Davoodi et al. [71] examined functionally graded Ti-6Al-4V implants using TPMS, engineered via SLM method to optimize both biological integration and mechanical performance. Their design strategically implemented high surface porosity (up to 90%) at the tissue interface to enhance cellular response, with gradually decreasing porosity toward the core to maintain structural integrity. Through systematic unit cell optimization,

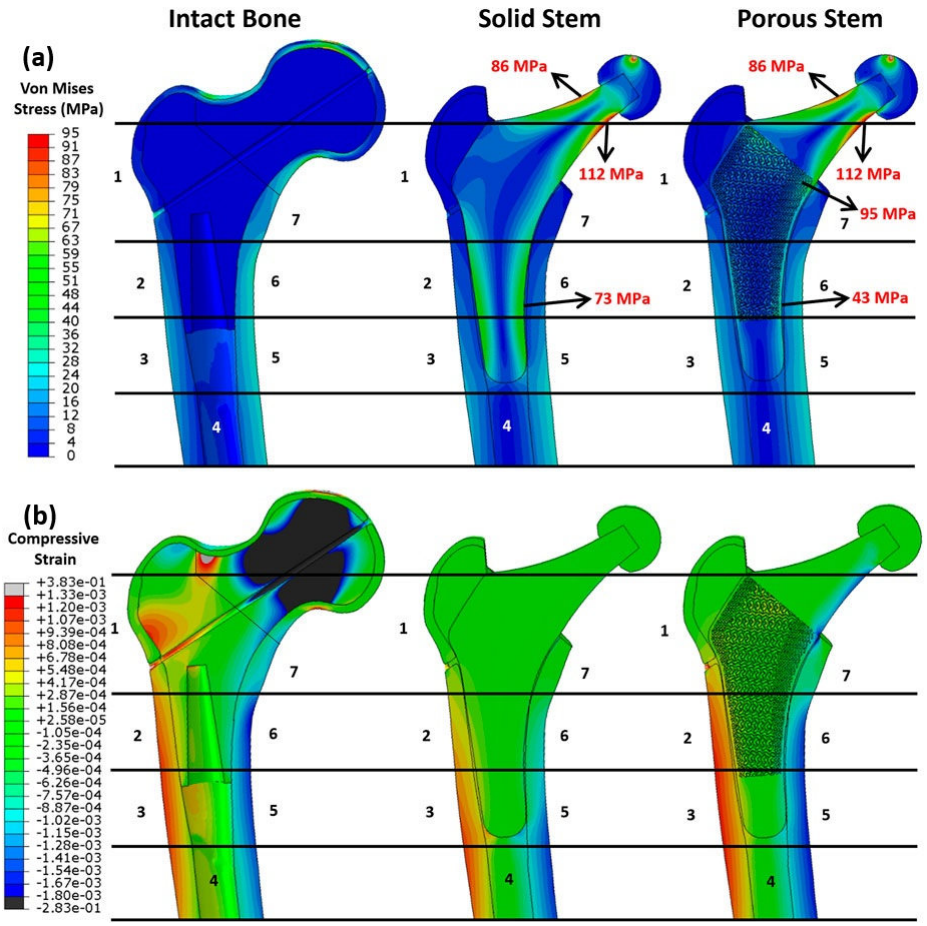

FIGURE 2.5: FEA results of stems (a) Von Mises stress and (b) Compressive strain

they identified bending-dominated TPMS architectures as superior to stretching-dominated designs, offering 40% greater strength-to-weight ratios while maximizing specific surface area. Finite element modeling demonstrated exceptional predictive accuracy (±13%) of implant behavior under physiological loads. Complementary in vitro studies revealed enhanced 2D cell attachment correlated with controlled surface roughness, and excellent 3D cell viability (>95%) when scaffolds were infused with GelMA hydrogel. These findings establish TPMS-based gradient porosity as a transformative approach for load-bearing orthopedic implants. Viet et al. [72] developed a computational framework to evaluate the mechanical performance of functionally graded (FG) TPMS titanium-bone interpenetrating phase composites (IPCs) under uniaxial compression. Through FEA and computational homogenization, validated against 3D-printed PLA-PVA model composites, the

study systematically quantified how gradient coefficient (-0.5 to +0.5), bone ingrowth length (20-100%), TPMS architecture (Gyroid/Primitive/Diamond/IWP), loading direction (axial/transverse), and relative density (30-70%) govern effective yield strength (YS) and stiffness. Key findings revealed: (1) IWP topologies demonstrated 15-20% higher YS than other TPMS structures at equivalent porosity; (2) Negative gradient coefficients enhanced YS by up to 35% versus positive gradients; (3) Complete bone ingrowth increased IPC stiffness by 2.3 times compared to 50% ingrowth; and (4) Anisotropic sensitivity showed 40% higher YS under axial versus transverse loading. These results establish design principles for optimizing load-bearing FG implants through controlled porosity gradients and topological bone-implant integration. Additionally, Tunca et al. [73] conducted a systematic finite element analysis of shelled hip implants with five distinct TPMS lattice infills (Gyroid, Diamond, Lidinoid, Schwarz, and SplitP) using magnesium AZ91 alloy. Under standardized loading conditions and identical unit cell sizes, results demonstrated that the Lidinoid structure exhibited the lowest von Mises stress concentrations, indicating superior load distribution capabilities, while the Schwarz topology showed the highest stress values. Furthermore, Naghavi et al. [74] developed bone-mimetic porous metallic scaffolds using gyroid and diamond TPMS architectures fabricated via additive manufacturing. With a constant sheet thickness of 300 m, the study systematically varied unit cell sizes to achieve controlled porosity (54-72%) and pore sizes (600-1500 m). Comprehensive mechanical characterization through experimental testing and finite element analysis demonstrated that both scaffold types exhibited stiffness and strength properties comparable to cortical bone across compression, tension, bending, and torsion loading conditions. The results indicate these TPMS-based scaffolds effectively replicate the physical and mechanical properties of natural bone, making them promising candidates for orthopedic implants, with structure selection dependent on specific application requirements.

Naghavi et al. [75] investigated novel hip stem designs to reduce bone resorption and implant instability through stiffness optimization. The study developed two approaches: a low-stiffness PEEK stem and a 3D-printed titanium lattice

stem with graded stiffness. Comparative analysis using experimental and computational methods demonstrated that both designs significantly reduced stress shielding and bone resorption compared to conventional solid titanium stems, particularly in proximal femoral regions. The titanium lattice structure provided controlled stiffness variation while maintaining mechanical integrity, offering improved load transfer characteristics.

2.4 Permeability

An essential factor in evaluating fluid flow behavior is permeability [76, 77]. Montazerian et al. [78] highlighted the significance of radial flow direction in scaffold design, contrasting it with conventional longitudinal permeability. Using computational models of lattice and TPMS geometries, they analyzed structure-property relationships across varying porosities. Key structures, Hexagonal and Rhombic Dodecahedron, were 3D-printed for experimental validation. Results revealed a 51.2% and +39.4% change in normalized radial permeability (vs. longitudinal) for the two structures, demonstrating the need to incorporate radial flow in scaffold design. Permeability-porosity relationships were modeled via power-law and Kozeny-Carman equations, with experimental conditions' effects also discussed. Similarly, Zhianmanesh et al. [79] investigated radially graded porosity scaffolds as a means to enhance both mechanical and biological performance. Using TPMS, they numerically and experimentally evaluated fluid permeability across different pore shapes and porosity distributions. Among uniform porosity scaffolds, the P* (P surface) and Y** (G surface) designs exhibited the highest permeability. For radially graded scaffolds with linear porosity distribution, permeability was approximately twice as sensitive to peripheral porosity compared to central porosity. The study revealed that permeability-gradient relationships vary with pore shape, deviating from conventional uniform porosity scaffolds and necessitating tailored design maps. Experimental validation via constant head permeability tests confirmed the findings, with the influence of fluid height on measurements

also analyzed. Furthermore, Montazerian et al. [80] developed polydimethylsiloxane (PDMS) porous scaffolds using minimal surface architectures fabricated via an FDM 3D-printed sacrificial mold method. Their study examined pore characteristics' influence on compressive properties and fluid permeability, revealing that radially gradient pore distributions outperformed uniform porosity designs, exhibiting higher elastic modulus and enhanced permeability while maintaining strain-reversibility up to 40% cyclic compression. Among triply periodic minimal surfaces (TPMS), P-surface scaffolds demonstrated greater stiffness but lower permeability and densification strain compared to D and G-surfaces. Biocompatibility tests using mouse embryonic fibroblasts in gelatin methacryloyl (GelMA) showed >90% cell viability after 4 days, confirming the method's potential for creating complex organ-shaped scaffolds with tunable pore features for regenerative medicine applications.

Ma et al. [81] used computational fluid dynamics (CFD) to analyze the pressure and flow velocity in gyroid scaffold channels. The CFD results demonstrated that gyroid structures exhibit good fluid flow characteristics, with accelerated fluid movement observed in the middle of the channels. The study concluded that these flow properties make the structures suitable for nutrient transport. The authors proposed that CFD simulations can predict scaffold permeability prior to manufacturing, ensuring appropriate permeability for bone scaffold applications. Asbai-Ghoudan et al. [82] developed an analytical framework to predict permeability of TPMS structures (Fisher-Koch S, Gyroid, Schwarz P) based on architectural parameters. Using CAD models with varied cell sizes and porosities, they calculated permeability via CFD under laminar flow. Results demonstrated architecture-dependent permeability trends, with all structures showing porosity-permeability correlations (R^2>0.99, p<0.001 for model fit). The derived geometry-based model predicted permeability within <5% error, enabling combined optimization of structural and flow properties for biomedical scaffolds.

Ali et al. [83] compared gyroid and lattice-based rectangular scaffolds with porosities ranging from 65% to 90%. Permeability, calculated via Darcy's law using

CFD-derived pressure drops, increased with porosity while wall shear stress decreased. Lattice-based models demonstrated higher permeability and lower wall shear stress than gyroid models at equivalent porosity levels. The study identified optimal scaffold models that best mimicked cancellous bone properties in terms of both elastic modulus and permeability. Santos et al. [84] experimentally evaluated the permeability of three TPMS scaffolds (Schwartz Diamond (SD), Gyroid (SG), and Schwartz Primitive (SP)) with porosities ranging from 50% to 80%. The study found that SG scaffolds exhibited the highest permeability, while SD scaffolds showed the lowest. Permeability measurements also confirmed the presence of microscopic inertial pressure losses, and Forchheimer's law was validated as an effective extension of Darcy's law for permeability calculations. However, the weak-inertia regime proved difficult to detect or quantify. Montazerian et al. [85] identified TPMS geometries with optimal permeability characteristics for scaffold design. At the critical 30% relative density for bone tissue engineering, P* and Ixxx-J* structures demonstrated the highest permeability while maintaining mechanical integrity. Among low-stiffness geometries, Fxyz-Fxxx2 exhibited superior permeability. The study established that strut orientation significantly influences permeability, with 45° inclined linkages promoting bending-dominated deformation patterns that affect fluid flow characteristics.

Yu et al. [86] evaluated permeability in Ti-6Al-4V porous scaffolds (65% porosity) with primitive, gyroid, and BCC architectures fabricated by SLM technique. Permeability measurements using the falling head method revealed significant architectural dependence, with gyroid scaffolds exhibiting approximately 20% the permeability of BCC structures. CFD simulations corroborated these experimental findings. The study demonstrated that internal scaffold architecture critically influences permeability characteristics in orthopedic implants, independent of its established effects on mechanical properties. Furthermore, Li et al. [87] investigated how TPMS unit configurations and parameters affect scaffold permeability through CFD simulations. The study established normalized permeability values as key performance indicators, demonstrating that architectural parameters significantly influence fluid flow characteristics. Experimental validation was performed using SLM-fabricated Primitive and IWP scaffolds (12mm cubes with

2×2×2 units). Both simulations and experiments confirmed that unit configuration critically determines permeable properties, providing a basis for optimizing TPMS designs for specific tissue engineering needs. Ali et al. [88] computationally designed eight bone scaffold models with 80% porosity using TPMS and lattice-based structures, analyzing their fluid flow characteristics through CFD. The study revealed that scaffold architecture significantly influences permeability, with variations up to threefold between different designs. Scaffolds exhibiting minimal channel size variation demonstrated the highest permeability values. While analyzing wall shear stress distribution, the results showed no correlation between scaffold architecture and shear stress patterns. Luo et al. [89] conducted pore-scale numerical studies of fluid flow in bicontinuous Gyroid structures using the lattice Boltzmann method (LBM). The analysis of pore-scale velocity fields enabled the prediction of macroscopic permeability, revealing distinct transport properties between the two continuous phases of the Gyroid. Results demonstrated that one phase exhibits significantly lower transport resistance than the other, suggesting that selecting the phase with higher permeability can optimize fluid transport efficiency. Shahid et al. [90] computationally analyzed the fluidic properties of Diamond and SplitP scaffolds with porosities of 55%, 65%, and 75% for bone tissue engineering. Using a power law model to simulate non-Newtonian blood flow, the study evaluated permeability, pressure drop, and wall shear stress (WSS). Results showed that increasing porosity significantly enhanced permeability while reducing both pressure drop and WSS. These findings indicate that Diamond and SplitP scaffolds, particularly at higher porosities, can be optimized to improve fluid transport, creating favorable conditions for cell adhesion, migration, and proliferation. The study highlights the critical role of porosity in tuning permeability for tissue engineering applications.

2.5 Surface Roughness

The Ti6Al4V alloy has long been the dominant material for metallic implants in THA and remains widely utilized, particularly in the United States. However,

in recent years, the Ti6Al7Nb alloy has gained significant prominence as a preferred alternative due to its superior biocompatibility. This improvement stems from the substitution of vanadium (which can release toxic ions at elevated concentrations) with niobium, a more biologically compatible element. As a result, Ti6Al7Nb has emerged as the leading material for femoral stems in both hip and knee endoprostheses [91].For cementless hip implants to function effectively, achieving maximal bonding strength between the femoral bone and implant is essential. Surface roughness plays a critical role in enhancing osseointegration and long-term stability of hip implants, particularly in cementless femoral stems [92]. Vulović et al. [93] demonstrated that rough implant surfaces can minimize micromovement between the femoral implant and the surrounding bone, facilitating stronger integration and reducing the likelihood of loosening. The authors also found that specific surface topographies influence shear stress distribution at the bone-implant interface, playing a significant role in determining the stability of cementless implants. Kawai et al. [94] highlighted that the surface finish of non-cemented implants, particularly based on their roughness ranging from 1.0 to 2.5 micrometers, substantially affects fixation rates following surgery. While rough surfaces can enhance the biological fixation process, excessive roughness or poorly designed surfaces may lead to complications [95]. Schuh et al. [96] argue that increasing surface roughness does not always improve integration and may instead raise the risk of abrasion, ultimately leading to weaker bone-implant bonding. Ali et al. [97] investigated surface roughness effects on scaffold permeability and WSS using CFD analysis. Three scaffolds with square pores (300, 600, and 900 m) at 63% porosity were modeled with six roughness levels (0–20 m). Results showed increased roughness reduced permeability and WSS in all scaffolds. A significant WSS reduction occurred between smooth and maximum roughness (20 m) models. Permeability remained stable across roughness variations, except in the 300 m pore scaffold. Similarly, Hoffman et al. [98] produced surface roughness levels varying from Ra=0.07 µm to 6 µm on commercially pure titanium (CpTi) and Ti6Al4V specimens. Their findings indicated that higher surface roughness promotes improved osseointegration and enhances the likelihood of mechanical interlocking between the bone and implant interface. Furthermore, Rupp et al. [99]

demonstrated that surface roughness improves the osseointegration of titanium implants and can influence wettability behavior. Cooper [100] conducted in vitro and in vivo studies, concluding that higher surface roughness on commercially CpTi implants enhances bone integration at the interface.

Janeczek et al. [101] developed nanostructured Ti6Al7Nb implants via SLM for bone regeneration. Two surface treatments were compared: chemical polishing (nitric acid/fluoride mixture) and control cleaning (distilled water/isopropyl alcohol). Structural analysis (XRD, TEM, SEM) confirmed nanoparticle sizes of 25–90 nm (Rietveld method). In vivo testing in New Zealand rabbits (skull implantation) demonstrated superior osseointegration in chemically polished implants versus controls at 1–3 month intervals, as confirmed by macroscopic/microscopic evaluation.

Taken together, prior studies demonstrate clear progress but still leave important practical gaps. Cemented and cementless stems made from high-stiffness alloys often cause stress shielding and proximal bone loss. Uniformly porous stems improve early fixation, yet they do not match the femur's site-specific mechanics. Designs based only on dense or porous regions usually trade biological integration for stability, or the other way around, and distal micromotion remains a concern when stem geometry does not manage load transfer effectively. These limitations highlight the need for stem designs with radially graded porosity, where the inner and outer parts of the stem are varied to provide both strength and support for bone healing.

2.6 Novelty of Work

This work introduces a novel functionally graded femoral stem that combines radially graded porosity with dense regions to achieve both mechanical strength and biological fixation. Unlike conventional implants with uniform designs, the stem employs controlled radial porosity to better mimic natural bone mechanics, reducing stress shielding while supporting bone ingrowth. In addition, the incorporation

of surface roughness in the distal region enhances fixation stability, addressing a key limitation of current prostheses.

Chapter 3

Research Methodology

3.1 Methodology Flowchart

The detailed methodology adopted in this study is illustrated in Figure 3.1. The proposed methodology for developing and analyzing a TPMS-based femoral stem design follows a comprehensive, multi-stage workflow, beginning with homogenization and culminating in FEA and CFD analyses. The process initiates with the homogenization of the TPMS unit cell to determine its effective mechanical properties, particularly Young's modulus. This involves defining the design space and unit cell geometry, adjusting wall thickness and relative density, and performing surface and volume meshing until mesh convergence is achieved. Periodic boundary conditions are applied to solve the model, and the extracted material properties are later used in the finite element analysis phase.

Following homogenization, the workflow advances to the incorporation of TPMS in the proximal region of the femoral stem. The CAD model is converted into an implicit body and segmented into three anatomical regions: the neck, distal, and proximal sections. The proximal region is embedded with the selected TPMS structure, using a ramp function to modulate wall thickness for tailored porosity. This porosity is quantified using image analysis tools like Fiji to ensure it meets design criteria. If necessary, iterative adjustments are made until the target architecture is achieved. The next module addresses surface roughness generation in

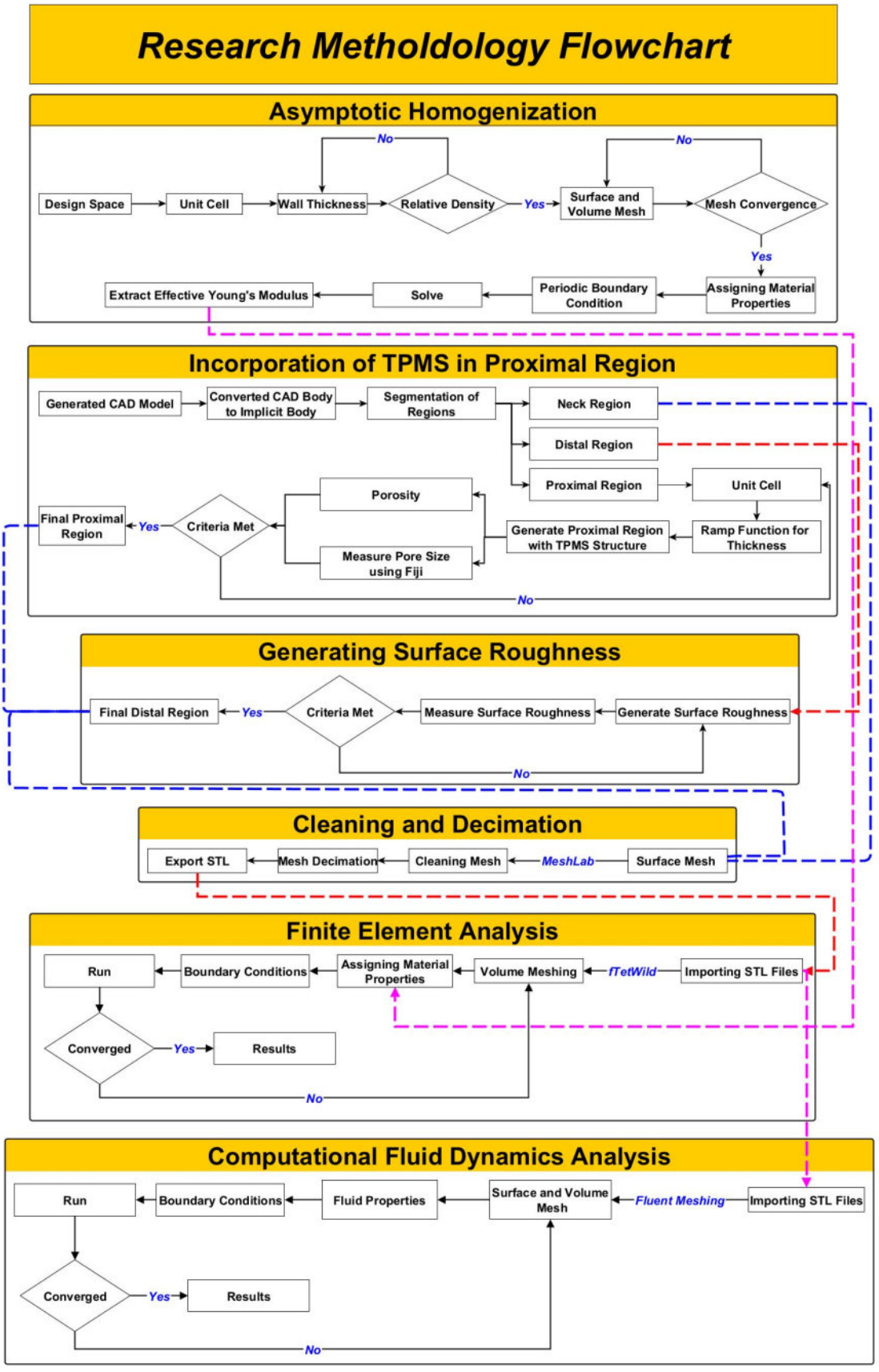

FIGURE 3.1: Research methodology integrating asymptotic homogenization, TPMS-based proximal design with porosity and roughness control, mesh cleaning and decimation, and FEA/CFD analyses for structural and fluid performance evaluation

the distal region. Surface textures are applied to promote osseointegration, and their roughness is quantitatively assessed. This process also follows an iterative pathway until predefined roughness criteria are satisfied. After finalizing the geometry, the model undergoes cleaning and decimation, where it is exported as an STL file and processed in MeshLab. This step ensures the mesh is simplified and free of artifacts, producing a clean and optimized surface mesh for simulation purposes.

Subsequently, FEA is performed to assess the mechanical performance of the femoral stem under physiological loading, following ISO 7206-4 standards. The STL geometry is imported into FEA software such as fTetWild, followed by volume meshing and the assignment of material properties obtained during homogenization. Boundary conditions replicating hip joint loads are applied, and the simulation is run to evaluate von Mises stress, deformation, and stress distribution. If the solution does not converge, meshing or boundary conditions are adjusted accordingly.

Lastly, for studies requiring biological or flow-related assessments, the CFD analysis module is included. Here, the surface and volume meshes are generated using Fluent Meshing, and fluid properties, such as viscosity and flow rate, are defined. Simulations are run to understand nutrient or fluid transport behaviors through the porous structures, with convergence checks ensuring result reliability.

3.2 Asymptotic Homogenization (AH) Method

Asymptotic homogenization (AH) is a mathematical method used to determine the effective macroscopic properties of periodic microstructures by analyzing the behavior of their unit cells [102]. This method is particularly suitable for triply periodic minimal surface (TPMS) structures because of their inherent periodicity and geometric complexity. By applying AH, the heterogeneous lattice of TPMS can be replaced with an equivalent homogeneous material that possesses effective elastic properties, which can then be used in structural simulations.

The key concept of AH is that all field quantities, such as displacement or strain, vary on two distinct scales: the macroscopic scale x, which describes smooth variations across the whole structure, and the microscopic scale $y = \frac{x}{\epsilon}$, which describes rapid oscillations inside a repeating unit cell. Here, ϵ is a small parameter representing the ratio of unit-cell size to the overall structure size. In this way, the material is assumed to behave smoothly on the large scale while simultaneously exhibiting periodic fluctuations at the micro scale.

Based on this two-scale framework, the displacement field $\mathbf{u}$ can be expressed as an asymptotic expansion in powers of ϵ:

$$u^{\epsilon}(x) = u_0(x, y) + \epsilon u_1(x, y) + \epsilon^2 u_2(x, y) + \cdots \tag{3.1}$$

Here, $u^{\epsilon}(x)$ is the actual displacement in the porous structure, $u_0(x, y)$ represents the smooth, average displacement observed at the macroscopic scale, and $u_1, u_2, \ldots$ are higher-order periodic corrections that arise from the detailed pore geometry. Physically, u_0 describes how the femoral stem implant deforms under loading when the fine details of the pores are ignored, while u_1 and u_2 capture local adjustments in displacement within each repeating cell. This concept is visualized in Figure 3.2, where the straight line corresponds to $u_0(x)$ and the oscillating curve represents the microstructural corrections $\varepsilon u_1(x, y) + \varepsilon^2 u_2(x, y)$.

Differentiating the displacement expansion gives the expression for the small-strain tensor:

$$\varepsilon(u) = \tfrac{1}{2}\left(\nabla u_0^T + \nabla u_0\right)_x + \tfrac{1}{2}\left(\nabla u_1^T + \nabla u_1\right)_y + O(\epsilon) \tag{3.2}$$

The $\frac{1}{2}\left(\nabla u_0^T + \nabla u_0\right)_x$ term represents the macroscopic strain derived from the smooth displacement field u_0, showing how the entire implant deforms under applied loading. The $\frac{1}{2}\left(\nabla u_1^T + \nabla u_1\right)_y$ term corresponds to microscopic strain fluctuations within the pores, reflecting bending and stress localization near the TPMS walls. Higher-order terms of $O(\epsilon)$ are much smaller and are typically ignored. In physical terms, the first term defines the global structural deformation of the stem, while the second term highlights local strain hot-spots that can influence fatigue or bone–implant interface behavior.

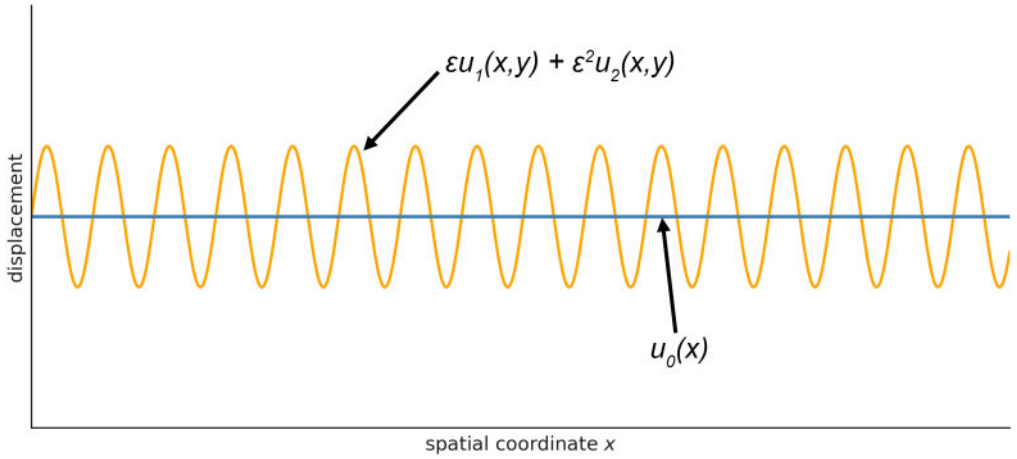

FIGURE 3.2: Graphical representation of Eq. 3.1. The displacement field $u^{\varepsilon}(x)$ is expressed as the sum of a smooth macroscopic component $u_0(x)$ and periodic microscale fluctuations $\varepsilon u_1(x, y) + \varepsilon^2 u_2(x, y)$. The smooth line represents the average displacement, while the oscillating line illustrates spatial fluctuations due to the repeating unit-cell geometry.

For clarity, the total strain can be written as the sum of an average (homogenized) strain and a fluctuating part:

$$\varepsilon(u) = \bar{\varepsilon}(u) + \varepsilon^*(u) \tag{3.3}$$

Here, $\bar{\varepsilon}(u)$ denotes the macroscopic strain that contributes to effective material properties, while $\varepsilon^*(u)$ captures the local oscillations at the micro scale. This decomposition reflects how the femoral stem carries load: the effective stiffness depends on $\bar{\varepsilon}$, while ε^* reveals localized effects that may control crack initiation, fatigue, or osseointegration.

The governing equilibrium equation for a heterogeneous elastic body with periodic microstructure can be expressed in strong form as:

$$-\nabla \cdot \big(C(x/\epsilon)\, \varepsilon(u^{\epsilon})\big) = f \quad \text{in } \Omega \tag{3.4}$$

In this equation, $C(x/\epsilon)$ is the fourth-order stiffness tensor that varies periodically with the unit cell geometry, $\varepsilon(u^{\epsilon})$ is the strain field, and f is the applied body force per unit volume. This ensures that, at every point, the internal stresses carried by the porous implant balance the external forces applied.

To make this equation solvable, especially with finite element methods, it is written in weak form. By multiplying with a virtual displacement v and integrating over the domain, we obtain:

$$\int_{\Omega^\epsilon} C_{ijkl} \left(\varepsilon^0_{ij}(v) + \varepsilon^1_{ij}(v)\right) \left(\bar{\varepsilon}_{kl}(u) + \varepsilon^*_{kl}(u)\right) \, d\Omega^\epsilon = \int_{\Gamma_t} t_i v_i \, d\Gamma \tag{3.5}$$

Here, C_{ijkl} are the stiffness components of the material, ε^0_{ij} and ε^1_{ij} are the macroscopic and microscopic strain terms, t_i is the traction applied on boundary Γ_t, and v is the admissible virtual displacement. Physically, this states that the internal work done by stresses equals the external work done by applied loads, which is the fundamental principle behind finite element analysis.

By separating macroscopic and microscopic contributions in the weak form, we obtain the following consistency condition at the microscale:

$$\int_{\Omega^\epsilon} C_{ijkl} \, \varepsilon^1_{ij}(v) \left(\bar{\varepsilon}_{kl}(u) + \varepsilon^*_{kl}(u)\right) \, d\Omega^\epsilon = 0 \tag{3.6}$$

This condition enforces that microscopic fluctuations do not generate additional unbalanced forces at the macroscopic scale. In practical terms, it means the pores may redistribute stress locally but cannot disturb the global equilibrium of the implant.

Finally, integrating over the representative volume element (RVE) leads to:

$$\int_{V_{RVE}} C_{ijkl} \, \varepsilon^1_{ij}(v) \, \varepsilon^*_{kl}(u) \, dV_{RVE} = - \int_{V_{RVE}} C_{ijkl} \, \varepsilon^1_{ij}(v) \, \bar{\varepsilon}_{kl}(u) \, dV_{RVE} \tag{3.7}$$

This expression defines the local boundary value problem at the RVE level. Solving it provides the fluctuating strain fields for imposed average strains, from which effective stiffness constants of the material can be computed. Physically, this is the step where the TPMS unit cell of the femoral stem is subjected to periodic boundary conditions, ensuring opposite faces deform compatibly. The result is a homogenized set of material properties that accurately represent the porous stem when used in finite element simulations.

3.2.1 Geometric Modelling of a Unit Cell

A systematic computational approach was employed to investigate the effective mechanical properties (Effective Young's Modulus) of six distinct TPMS lattice structures: Gyroid, Diamond, Schwarz, SplitP, Neovius, and Lidinoid. The equations for these structures are mentioned below and their graphical representations are illustrated in Figure 3.3, which highlights the unique morphological characteristics of each TPMS surface.

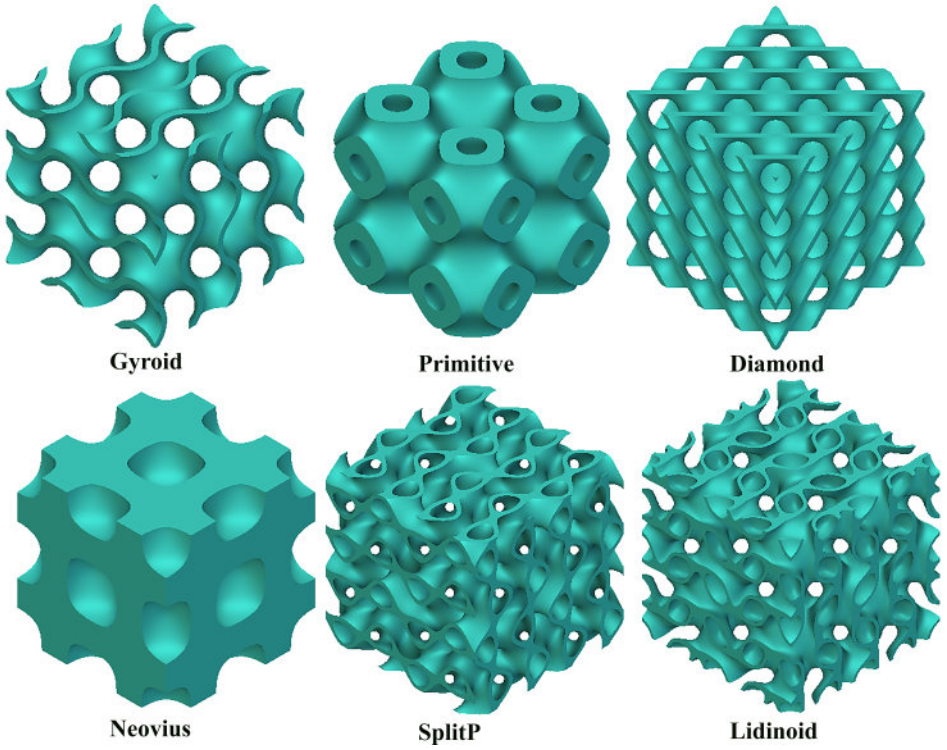

FIGURE 3.3: Graphical representation of the six TPMS structures

$$\textbf{Gyroid} \quad f(X,Y,Z) = \sin(X)\cos(Y) + \sin(Y)\cos(Z) + \sin(Z)\cos(X) \tag{3.8}$$

$$\textbf{Primitive} \quad f(X,Y,Z) = \cos(X) + \cos(Y) + \cos(Z) \tag{3.9}$$

$$\textbf{Diamond} \quad f(X,Y,Z) = \cos(X)\cos(Y)\cos(Z) \tag{3.10}$$

$$\textbf{Neovius} \quad f(X,Y,Z) = 3\left(\cos(X) + \cos(Y) + \cos(Z)\right) + 4\cos(X)\cos(Y)\cos(Z) \tag{3.11}$$

$$\begin{aligned}\textbf{SplitP} \quad f(X,Y,Z) = 1.1\Big(&\sin(2X)\cos(Y)\sin(Z) + \sin(2Y)\cos(Z)\sin(X) \\ &+ \sin(2X)\cos(X)\sin(Y)\Big) \\ &- 0.2\Big(\cos(2X)\cos(2Y)\cos(2Z) + \cos(2Z)\cos(2X)\Big) \\ &- 0.4\left(\cos(2Y) + \cos(2Z) + \cos(2X)\right) \end{aligned} \tag{3.12}$$

$$\begin{aligned}\textbf{Lidinoid} \quad f(X,Y,Z) = 0.5\Big(&\sin(2X)\cos(Y)\sin(Z) + \sin(2Y)\cos(Z)\sin(X) \\ &+ \sin(2Z)\cos(X)\sin(Y)\Big) \\ &- 0.5\Big(\cos(2X)\cos(2Y) + \cos(2Y)\cos(2Z) \\ &+ \cos(2Z)\cos(2X)\Big) \\ &- \cos(2X) + 0.15 \end{aligned} \tag{3.13}$$

Here, the coordinates X, Y, Z are defined as $2\pi n_i/L_i$, where n_i represents the number of unit cells and L_i denotes the cell size along the i-th dimension.

Each TPMS unit cell was generated within a cubic design space (domain) of dimensions $3 \times 3 \times 3\,\text{mm}$, ensuring geometric periodicity for homogenization analysis. To evaluate the influence of relative density on homogenized properties, each TPMS architecture was parametrically designed with varying wall thicknesses, corresponding to relative densities of 0.1, 0.2, 0.3, 0.4, and 0.5%. The necessary

TABLE 3.1: Wall thickness (mm) corresponding to relative density (%) for each TPMS unit cell

	Relative Density (%)				
Structure	**0.1**	**0.2**	**0.3**	**0.4**	**0.5**
Diamond	0.13	0.26	0.39	0.516	0.643
Gyroid	0.16	0.32	0.465	0.617	0.767
Lidinoid	0.08	0.16	0.24	0.347	0.48
Neovius	0.027	0.054	0.0791	0.113	0.18
Schwarz	0.09	0.18	0.263	0.35	0.437
SplitP	0.12	0.23	0.344	0.457	0.573

wall thickness to attain a given relative density differs among TPMS architectures because of their distinct geometric characteristics. Through an iterative approach, the exact thickness values matching each relative density were determined.

Table 3.1 presents the finalized thickness parameters for all six TPMS structures across the five relative density levels. The material used for the unit cell was Ti6Al7Nb, whose mechanical properties are listed in Table 3.2.

TABLE 3.2: Mechanical properties of Ti6Al7Nb [103, 104]

Mechanical properties	Unit	Values
Elastic constants	GPa	113
Poisson ratio	-	0.32
Density	g/cm^3	4.52
Ultimate tensile strength	MPa	862
Yield tensile strength	MPa	800
Elongation at break	%	10

3.2.2 Mesh Independence Study

A mesh independence study was conducted on the Diamond TPMS unit cell to identify an optimal mesh resolution that ensures computational accuracy while maintaining reasonable simulation efficiency as shown in Figure 3.4. The nu-

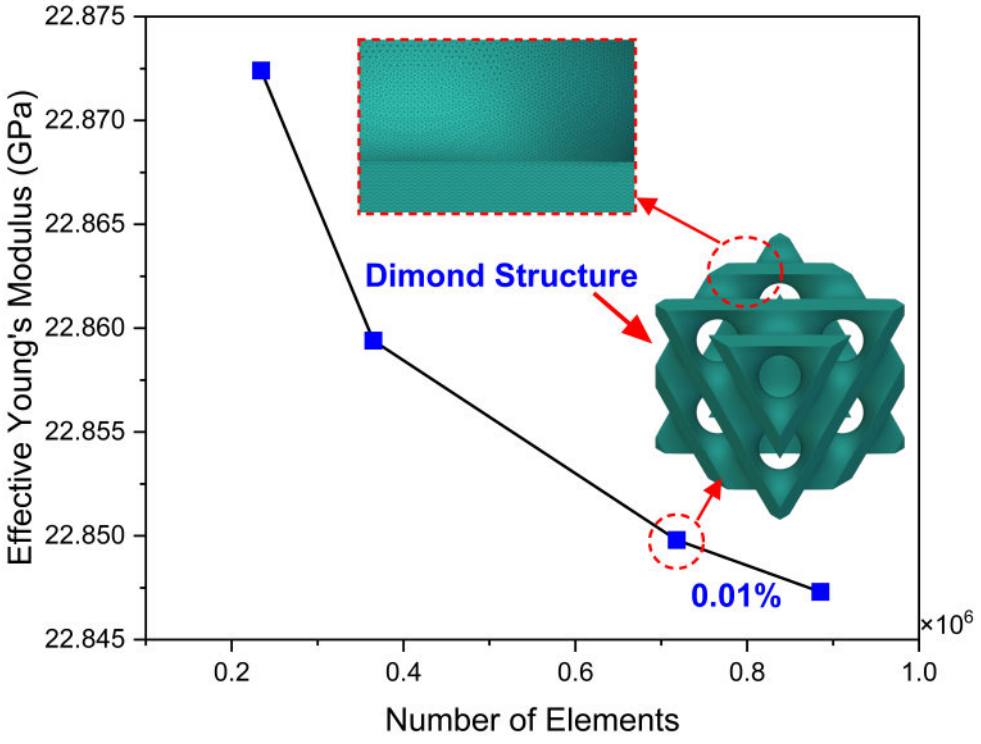

FIGURE 3.4: Mesh independence study for homogenization

merical analysis was performed using quadratic tetrahedral elements within the

nTop software environment, with the effective Young's modulus selected as the key convergence criterion. Through iterative mesh refinement, it was observed that increasing the number of finite elements from 718,054 to 885,368 resulted in a marginal deviation of merely 0.01% in the computed Young's modulus. This negligible variation confirms that numerical convergence was achieved at 718,054 elements, beyond which further mesh refinement yielded no significant improvement in solution accuracy. Consequently, this mesh configuration was adopted for all subsequent finite element simulations to ensure reliable and computationally efficient results.

3.2.3 Effective Modulus Evaluation in TPMS Structures

In this study, AH was used to evaluate the effective Young's modulus of six different TPMS structures (Diamond, Gyroid, Lidinoid, Neovius, Schwarz, and SplitP) at five relative density values: 0.1, 0.2, 0.3, 0.4, and 0.5 as shown in Figure 3.5. The purpose was to identify a scaffold configuration whose mechanical properties are comparable to those of natural human bone, specifically the femoral bone, which generally exhibits a young's modulus ranging from 0.02 to 22.3 GPa [105, 106].

Figure 3.5 shows contour plots of stiffness distribution for each structure. Structures with relative densities of 0.1, 0.2, and 0.3 fall within the acceptable physiological range for human bone. At a relative density of 0.4, certain configurations result in effective Young's moduli nearing or slightly exceeding the upper physiological limit. In contrast, a density of 0.5 usually exceeds this range, posing a risk of stress shielding. We opted for a relative density of 0.3 for further analysis, as it offers a balanced comparison: all structures at this density remain within the physiological range and provide significantly greater stiffness than those at 0.1–0.2, which exhibit noticeably lower moduli. Therefore, a relative density of 0.3 achieves an optimal compromise between structural rigidity and physiological compatibility without substantially heightening the risk of stress shielding. Diamond, Neovius, and Schwarz show a conical pattern at low relative density that rounds toward a more circular form as density increases, consistent with a shift from bending of thin

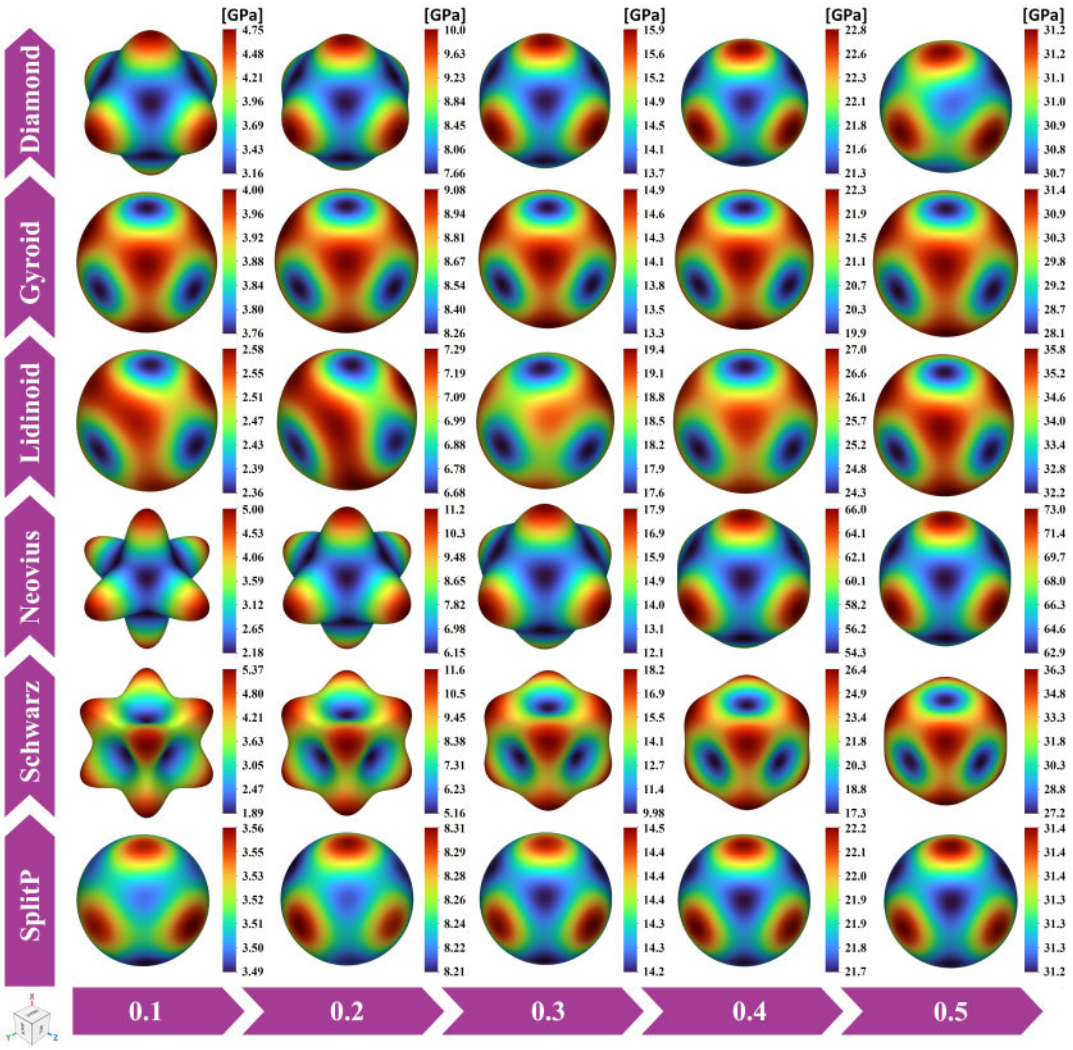

FIGURE 3.5: Effective young's modulus (GPa) distribution of six TPMS structures (Diamond, Gyroid, Lidinoid, Neovius, Schwarz and SplitP) across relative densities (0.1–0.5)

curved features to more continuous axial load transfer through connected regions. Gyroid and SplitP remain nearly circular across the densities considered, and Lidinoid is also largely circular, indicating a more uniform directional response. In all cases the lower stiffness directions correspond to paths that pass through thin curved regions of the cell, whereas the higher stiffness directions align with the more connected parts of the surface that carry load primarily by direct axial load transfer. At the chosen density of 0.3 these patterns are sufficiently uniform across topologies to support consistent downstream testing and comparison. In addition, the value of 0.3 lies comfortably within the mid-range of acceptable physiological densities, further justifying its use as it avoids the extremes that may lead either to insufficient stiffness or to excessive rigidity.

3.3 Geometric Modelling

3.3.1 CAD Modelling

In this study, a commercially available femoral stem from Stryker's *Secur-Fit® Advanced Femoral Hip System* was selected for CAD modelling. Stryker is a leading global manufacturer of orthopaedic implants, and the *Secur-Fit Advanced* system represents a widely adopted cementless press-fit design. The system is available in two neck angle configurations: 132° (standard offset) and 127° (high offset), which provide flexibility for restoring individual patient biomechanics. The geometric specifications of each variant are provided in the official Stryker product catalog [107].

For this work, the 127° high-offset version (Catalog No. 1601-11127) was chosen. This configuration increases femoral offset and improves the abductor lever arm while maintaining leg length; factors that are essential for restoring physiological muscle function and joint stability. Previous studies have demonstrated that modest increases in femoral offset enhance hip biomechanics and contribute to improved implant performance [108]. The key dimensional parameters of the selected implant are summarized in Table 3.3.

TABLE 3.3: Geometric specifications of the selected femoral stem [107]

Property	**Value**
Stem	Secur-Fit Advanced 127°
Catalog number	1601-11127
Neck angle (°)	127
Stem size	11
Stem length (mm)	155
Neck length (mm)	40
Femoral offset with +0mm head (mm)	52.6
Distal tip diameter (mm)	9.7

The CAD model of the femoral stem was reconstructed in SolidWorks 2024 using parametric modelling, based directly on the dimensional data reported in the manufacturer's catalog. This ensured that the taper geometry, neck angle, and overall contours were faithfully reproduced for accurate biomechanical simulation.

A labeled diagram of the implant is shown in Figure 3.6, which highlights the principal geometric features used for CAD modelling.

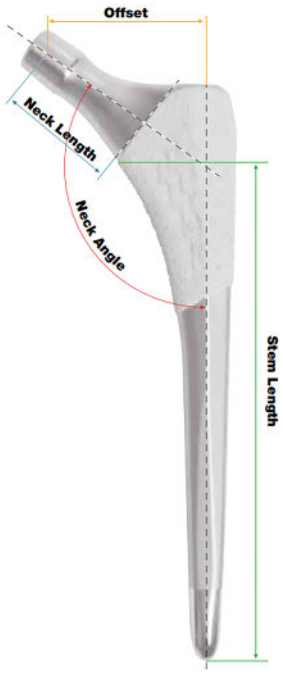

FIGURE 3.6: Labeled diagram of the selected stem indicating key geometric features

3.3.2 Regional Segmentation of the Femoral Stem

Figure 3.6 shows the stem divided into three anatomically and functionally distinct regions: neck, proximal, and distal. This segmentation supports targeted finite element simulations by allowing region specific material definitions, load application points, and boundary conditions. Boundaries were placed at geometric and anatomical transitions on the catalogued reference implant that guided the CAD model: the neck region runs from the head taper to the neck to body junction, the proximal region spans the metaphyseal flare and ends where the section becomes near constant, and the distal region continues from this transition to the stem tip. The model was created in SOLIDWORKS using a scaled manufacturer image and catalogue dimensions cited earlier; any missing values were taken by proportional measurement on the scaled image, and the segmentation planes were inserted normal to the stem axis at the stated transitions so that the regions in the model match the functional zones of the reference implant.

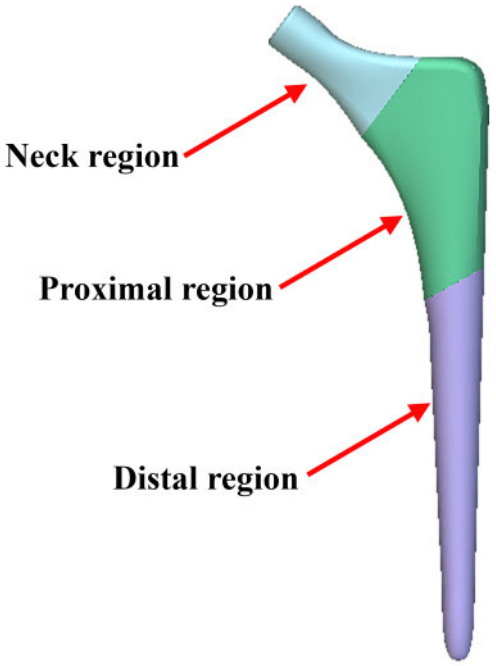

FIGURE 3.7: Regions of femoral stem

3.3.3 Implicit Modeling for Functionally Graded Biomimetic Structure

To optimize the mechanical and biological performance of the femoral implant, a TPMS structure was incorporated into the proximal region of the stem. This design strategy aims to mimic cancellous bone behavior and enhance osseointegration while minimizing stress shielding. To implement the TPMS geometry with controlled gradation of porosity and thickness, implicit modelling techniques were employed. Unlike traditional mesh-based approaches, implicit modelling allows smooth, continuous variation of features like wall thickness and pore size through scalar fields and mathematical functions. In conventional mesh-based modelling, porous structures are usually built from predefined unit cells or surface meshes that are repeated, which can lead to abrupt changes, discontinuities, or artifacts when adjusting pore size or wall thickness. By contrast, implicit modelling is function-based: the geometry is described using scalar fields and mathematical equations instead of fixed meshes. A scalar field is simply a mathematical function that assigns a numerical value (such as density or thickness) to every point

in 3D space. By controlling these values, features like pore size and wall thickness can be varied smoothly and continuously across the implant, without sharp transitions or distortions.

For this purpose, the Ramp Block function was utilized to define a scalar field, enabling spatial control over the internal architecture of the structure. In nTop, this type of design is referred to as a field-driven implicit structure, meaning that the geometry is not created from fixed meshes or predefined unit cells, but is instead generated directly from mathematical fields. These fields assign values (e.g., thickness, porosity) at every point in space, and the structure is then shaped according to those values. This allows precise and gradual variation of features across the model, making it possible to tailor the implant's porosity and thickness distribution according to the design requirements. Initially, the proximal region defined in the CAD model was scaled down and imported into nTop to accurately apply the field-driven implicit structure. Once inside nTop, the same CAD geometry (the already scaled proximal region) was further reduced by a factor of two along the x-direction only. This secondary downscaling was performed to correctly align the model and fit it within the working domain before applying the implicit field.

A systematic evaluation of different wall thickness values was carried out to generate pore sizes within the range of 300–600 μm [19], while maintaining an overall porosity of approximately 70%. Literature suggests that pores around 300 μm or larger are necessary to allow vascularization, as blood vessels require sufficient space to form and support nutrient transport for tissue regeneration. On the other hand, pores closer to 600 μm have been shown to enhance osteoblast activity and accelerate bone ingrowth [109]. The selected porosity level of 70% falls within the physiological range of human cancellous bone, balancing the biological requirements for bone ingrowth and vascularization with the mechanical stability needed for compatibility with native bone tissue.

The selection of a 70% porosity level was supported by homogenization studies, which demonstrated that the corresponding effective Young's modulus closely

matches the mechanical behavior of cancellous bone. A detailed correlation between wall thickness and pore size is provided in Table 3.4, while Figure 3.8 illustrates the scalar field distribution used to control thickness variation, with the maximum and minimum thickness values indicated. This field-driven implicit modelling approach enabled a smooth and accurate gradation of pore architecture within the proximal region of the femoral stem.

TABLE 3.4: Wall thicknesses and pore sizes of selected structures

Structure	**Smallest wall thickness (Pore size)**	**Largest wall thickness (Pore size)**
Gyroid	0.38 mm ($375\ \mu m$)	0.164 mm ($592\ \mu m$)
Lidinoid	0.17 mm ($375\ \mu m$)	0.109 mm ($438\ \mu m$)

To quantitatively evaluate the pore sizes of the generated TPMS structures, Fiji® software was used. The process began by exporting high-resolution 2D images of representative sections of the lattice structures. These images were then imported into Fiji, where a smaller sub-region of interest was extracted for detailed analysis. The selected region was first converted to 8-bit grayscale, after which a color threshold was applied to differentiate the solid phase from the voids. Fol-

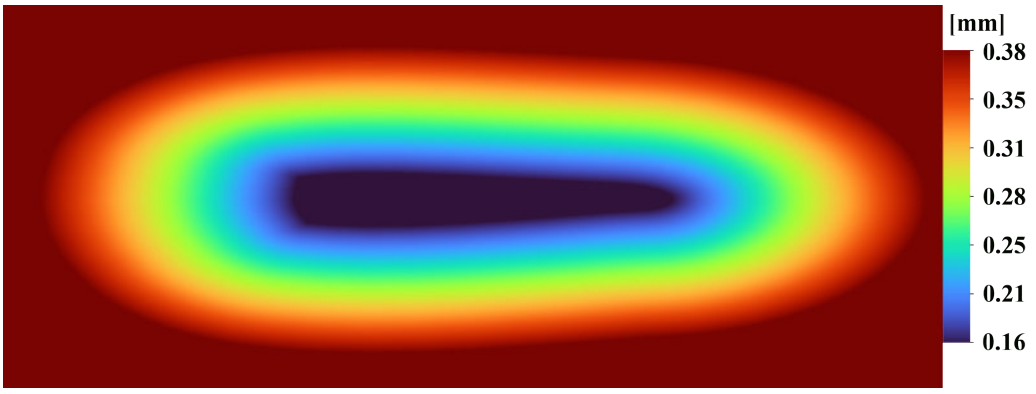

FIGURE 3.8: Scalar field of thickness distribution

lowing thresholding, the Analyze Particles function was applied to quantify the geometry of individual pores. Among the available output parameters, the Feret diameter was selected to represent pore size. The Feret diameter, also referred to as the caliper diameter, is defined as the maximum distance between two parallel

tangents on opposite sides of a pore. This parameter is particularly suitable for TPMS structures because the pores are often irregular and non-circular, making simple diameter measurements less representative. The measured Feret diameters were then compared across samples with different wall thickness values, allowing the relationship between wall thickness and pore size to be directly quantified. These measurements formed the basis for defining the design parameters used in the porous region of the implant. To identify suitable TPMS structure for the

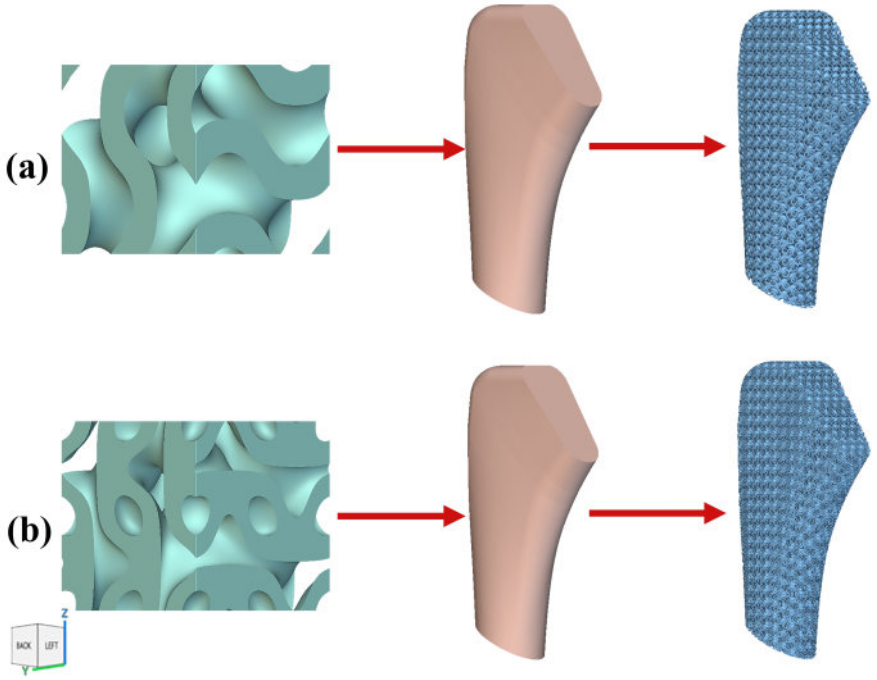

FIGURE 3.9: TPMS integration into proximal region (a) Gyroid (b) Lidinoid

proximal region of the femoral stem, six candidate structures were initially modeled and tested under the defined pore size and porosity constraints. During the integration process, four of these structures proved infeasible: when applied to the complex geometry of the proximal stem, their surfaces either collapsed, distorted, or resulted in wall thicknesses too thin to be manufacturable. After repeated parametric adjustments and iterative refinements, only the Gyroid and Lidinoid structure could be successfully incorporated without geometric breakdown. These two structures maintained the required porosity and pore size distribution, while also ensuring structural continuity and manufacturable wall thickness. Their ability to withstand these rigorous design constraints, together with their interconnected

porosity and favorable stress distribution characteristics, justified their final selection for integration into the implant design. The incorporated Gyroid and Lidinoid TPMS structures within the proximal femoral region are illustrated in Figure 3.9.

3.3.4 Surface Roughness on the Distal Region

To introduce micro-scale surface roughness on the distal region of the femoral stem, the Simplex Noise 3D function in nTop was applied. This function procedurally generates irregular surface patterns that replicate the micro-topography known to enhance bone–implant integration. The frequency parameter, set to 1000, controlled the density of the surface texture: higher values create finer, closely spaced irregularities, while lower values produce broader, more widely spaced variations. The noise output was then scaled by a factor of 0.0065 (defined as the texture

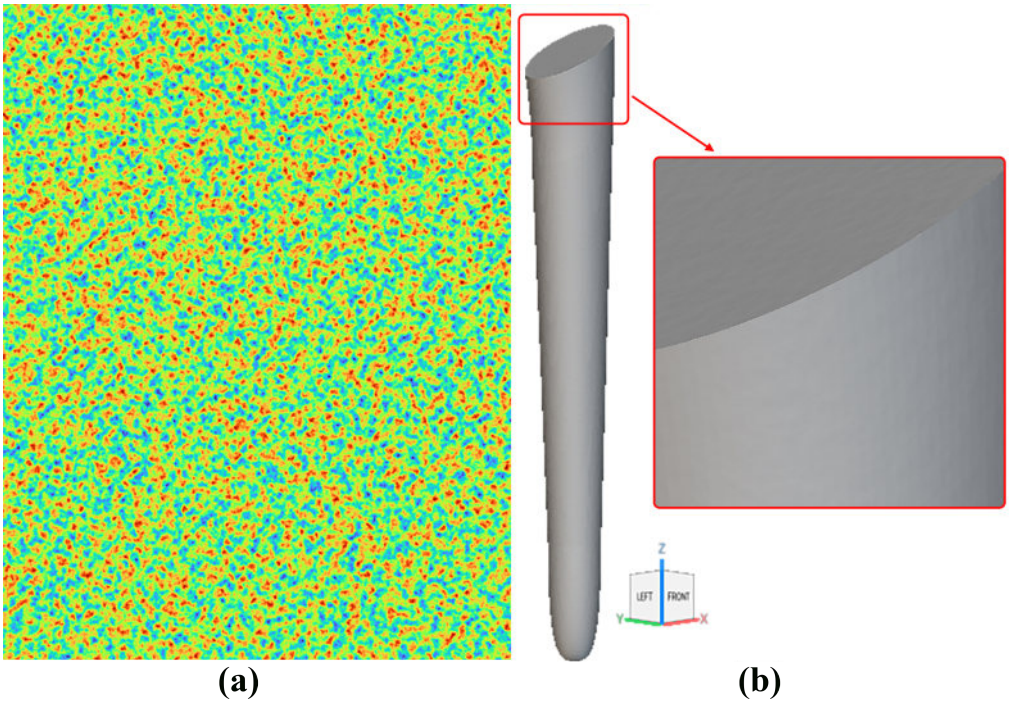

FIGURE 3.10: (a) Scalar field for surface roughness (b) Visulaization of surface roughness on distal region

amplitude) to regulate the height of the generated features. This adjustment resulted in an average roughness level of approximately 1.5 μm, which falls within the optimal range reported in literature for promoting osseointegration [110].

As shown in Figure 3.10 (a), the scalar field visualization confirms the consistent distribution of the applied roughness across the targeted region, while Figure 3.10 (b) presents the generated surface profile on the distal part of the stem. The introduction of this controlled microtexture increases the effective surface area of the implant, thereby improving bone–implant contact and supporting cellular attachment. Previous studies have reported that surface roughness within the range of 1–2 μm enhances osteoblast adhesion and proliferation, which contributes to faster and more stable biological fixation [110]. The selected roughness level was therefore incorporated to improve the implant's secondary stability and long-term clinical performance.

3.4 FEA Setup

3.4.1 Material Properties and Boundary Conditions

In this study, the FEA of the femoral stem was performed using ANSYS 2025 R1 to investigate the mechanical behavior of a customized femoral implant. The geometry comprised a femoral stem with a solid neck and distal region, while the proximal region incorporated TPMS structures with 70% porosity. The effective elastic modulus for the porous region was derived through a homogenization approach and assigned as a material property in the simulation.

Figure 3.11 illustrates the boundary conditions used to simulate physiological loading, where a static compressive load of 2300 N was applied to the femoral head. This replicates hip joint contact forces experienced during routine activities, approximately 2.5–3 times body weight for an 800 N individual, consistent with ISO 7206-4 guidelines [111, 112]. The stem was embedded within an epoxy block, with a bonded constraint applied at the stem–epoxy interface to replicate standard experimental setups. The bottom surface of the epoxy block was fully fixed to restrict translation and rotation.

The epoxy block was assigned a linear elastic modulus of 3.7 GPa, and the dense Ti-6Al-7Nb alloy regions (neck and distal) were modeled with an elastic modulus of 113 GPa. The proximal porous section was assigned an effective elastic modulus (obtained from homogenization).

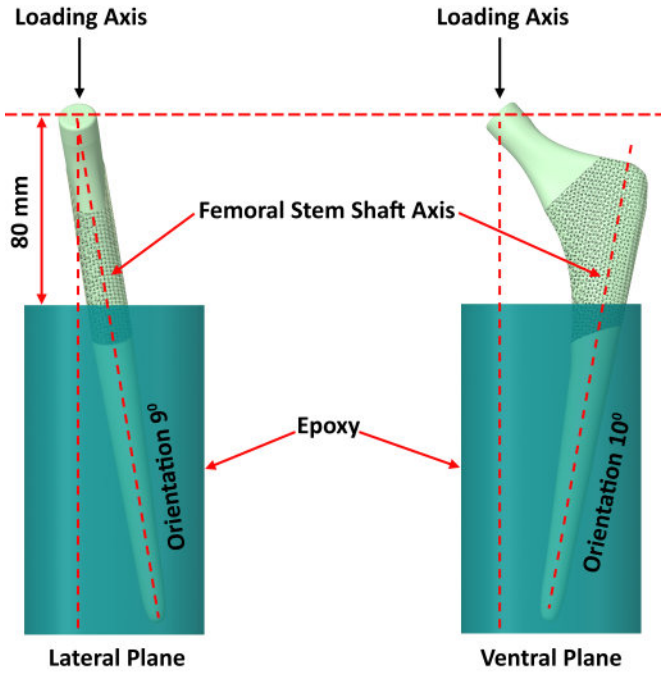

FIGURE 3.11: Boundary conditions on femoral stem according to ISO 7206-4 standard

3.4.2 Mesh Generation and Mesh Independence

The Gyroid structure was first modeled and surface meshed in nTop. The resulting surface mesh was exported as an STL file and imported into MeshLab, where geometric inconsistencies such as self-intersections were identified and corrected to ensure mesh quality. After cleaning, the corrected STL file was re-exported. The cleaned STL was then imported into fTetWild for volume meshing. Since fTetWild only generates linear tetrahedral elements, the linear mesh was exported and subsequently converted into quadratic elements using Gmsh to improve accuracy during finite element analysis. The quadratic mesh was then imported into the solver for structural simulations. The meshing process was computationally demanding due to the complexity of the gyroid structure. All meshing operations

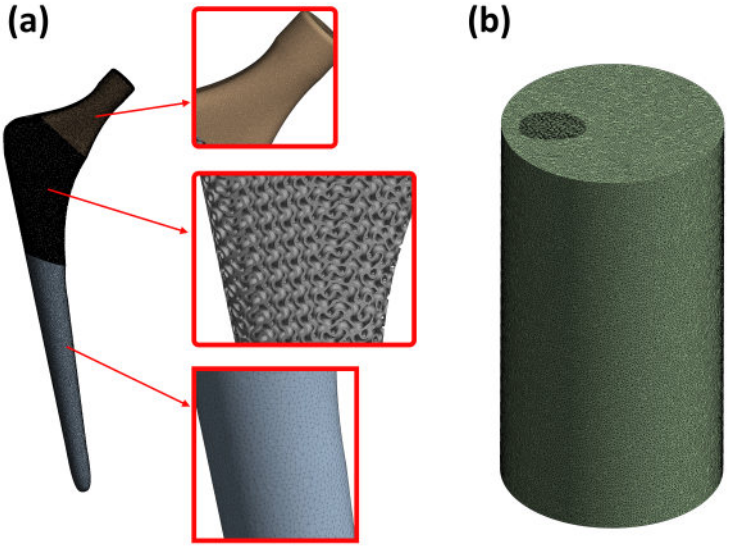

FIGURE 3.12: Mesh generation for FEA (a) Femoral Stem (b) Epoxy Base

were performed on a workstation equipped with an Intel® Core™ i5-7200U processor (4 cores) and 16 GB of RAM. Under these conditions, the generation of the complete volume mesh required approximately 14 hours. Figure 3.12 illustrates the detailed finite element mesh of the femoral stem model, highlighting the meshing of the solid, gyroid porous, and distal regions to capture the complex geometry accurately for analysis. A mesh convergence study was performed on the

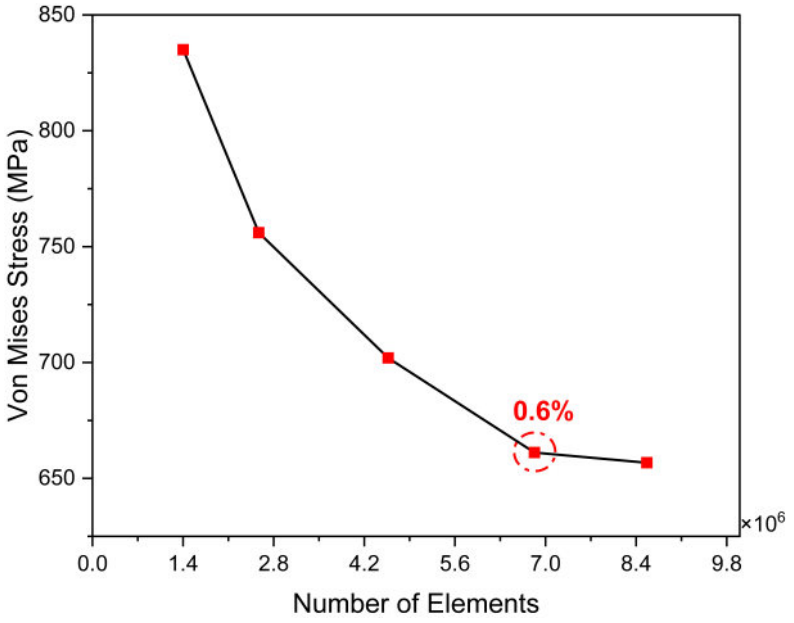

FIGURE 3.13: Mesh independence for FEA

gyroid structure by progressively refining the mesh and comparing the resulting

von Mises stress values. The convergence was achieved when the relative difference between the last two mesh refinements was approximately 0.6%, confirming the mesh independence of the simulation results and validating the selected mesh density for accurate and efficient analysis as shown in Figure 3.13.

3.4.3 Validation Study for FEA

The finite element model was validated by comparing the force–displacement response of two configurations: (i) a porous femoral stem, in which the gyroid lattice was explicitly modeled with its actual geometry and assigned bulk titanium properties, and (ii) an effective porous femoral stem, in which the lattice region was not modeled geometrically but instead represented as a solid domain with equivalent homogenized material properties derived from the porous structure. This approach, consistent with prior studies [113], allows the porous region to be computationally simplified while retaining its effective mechanical response. The com-

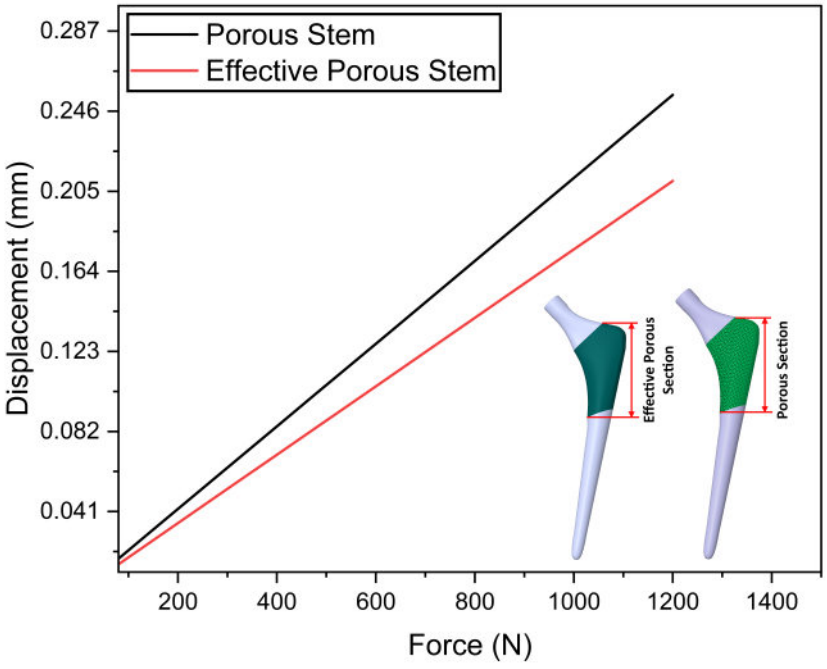

FIGURE 3.14: Validation study for FEA

parison showed close agreement between the two models, with the detailed porous stem displacement reaching 0.25 mm and the effective porous stem 0.21 mm under a 1200 N load. These results confirm that the effective porous stem can reliably

reproduce the structural response of the complex porous geometry while significantly reducing computational cost, as illustrated in Figure 3.14. This validation supports the adoption of the effective porous model for subsequent simulations in this study.

3.5 CFD Setup

3.5.1 Governing Equations

Considering a steady, incompressible, laminar fluid flow with constant density, the governing equations of fluid motion can be expressed as follows.

The momentum equation is given by:

$$\rho\frac{\partial \mathbf{v}}{\partial t} - \mu\nabla^2\mathbf{v} + \rho(\mathbf{v}\cdot\nabla)\mathbf{v} + \nabla p = \mathbf{F} \tag{3.14}$$

The continuity equation is expressed as:

$$\nabla\cdot\mathbf{v} = 0 \tag{3.15}$$

In this context, ρ represents the fluid density (kg/m^3), $\mathbf{v}$ denotes the fluid flow velocity (m/s), μ refers to the dynamic viscosity of the fluid (kg/(m·s)), ∇ is the del operator, p stands for pressure (Pa), and $\mathbf{F}$ indicates other forces, such as gravity or centrifugal force (where $\mathbf{F} = 0$ in this case) [114, 115].

In a laminar flow system, the wall shear stress (WSS, τ_w) is defined as the normal velocity gradient at the wall [90]:

$$\tau_w = \mu\frac{\partial \mathbf{v}}{\partial m} \tag{3.16}$$

where m indicates the x, y, and z directions.

The Reynolds number is expressed as:

$$Re = \frac{\rho v L}{\mu_a} \tag{3.17}$$

where ρ, v, L, and μ_a denote the fluid density, the magnitude of velocity, characteristic length, and apparent viscosity, respectively.

3.5.2 Blood Rheology Models

Both Newtonian and non-Newtonian simulations was conducted because bone is a highly vascularized tissue, and fracture events result in the rupture of blood vessels along the fracture line. This disruption causes extravasation of blood into the interstitial space between the fractured bone segments [116–118]. Consequently, upon scaffold implantation, blood permeates the porous structure of the scaffold. Incorporating the rheological properties of blood in fluid flow analyses within scaffolds is essential for improving the accuracy of such models. Although blood is frequently approximated as a Newtonian fluid with constant viscosity in parametric studies to simplify computational analyses [119, 120], its composition, including cellular elements, proteins, lipoproteins, and ions, imparts non-Newtonian characteristics [121].

3.5.2.1 Newtonian Case

For the CFD models, blood density was held constant at 1050 kg/m^3, and blood was approximated as a Newtonian fluid with a dynamic viscosity of 0.004 kg/(m·s) [122, 123]. The Darcy's classic equation was used to calculate the permeability (k_o) of Newtonian fluid [124].

$$k_0 = \frac{u\mu L}{\Delta p} \tag{3.18}$$

where L and Δp are the length of the model (m) and the pressure drop (Pa), respectively.

3.5.2.2 Non-Newtonian Case

For the analysis in which blood was treated as a non-Newtonian fluid, the viscosity of the fluid was computed utilizing the power law model as follows [125]:

$$\mu = K\gamma^{n-1}, \quad \mu_{\min} < \mu < \mu_{\max} \tag{3.19}$$

where K (kg·s^{n-2}/m) represents the consistency index, while γ (s^{-1}) denotes the shear rate. The power law exponent, n, indicates the type of fluid: $n = 1$ for Newtonian fluids, $n > 1$ for shear-thickening fluids, and $n < 1$ for shear-thinning fluids. The values of K and n chosen were 0.017 mPa·s and 0.708, respectively [126, 127]. Additionally, the lower and upper viscosity cutoffs, $\mu_{\min}$ and $\mu_{\max}$, were set at 0.001 and 0.1 kg/(m·s), respectively [125].

To calculate permeability for the non-Newtonian case, Morais et al. [128] presented an equation as follows:

$$k = uK\left(\frac{L}{\Delta p}\right)^{1/n} \tag{3.20}$$

3.5.3 Mesh Generation and Mesh Independence

In this study, fault-tolerant meshing was employed to ensure robust and error-free mesh generation for complex TPMS geometries. The geometry was discretized using polyhexahedral (poly-hexcore) elements in ANSYS Fluent, which provided a practical compromise between numerical accuracy and computational cost for porous structures. To better capture the intricate morphology of TPMS surfaces, curvature-based refinement was applied locally in regions of high curvature (Figure 3.15). This refinement strategy preserved the geometric features critical for resolving wall shear stress distributions and flow pathways within the porous domains.

To evaluate the reliability of the mesh, a mesh independence study was performed on the Lidinoid-based implant under steady-state fluid flow conditions. Five different mesh densities were tested, ranging from approximately 4.8 million to 11

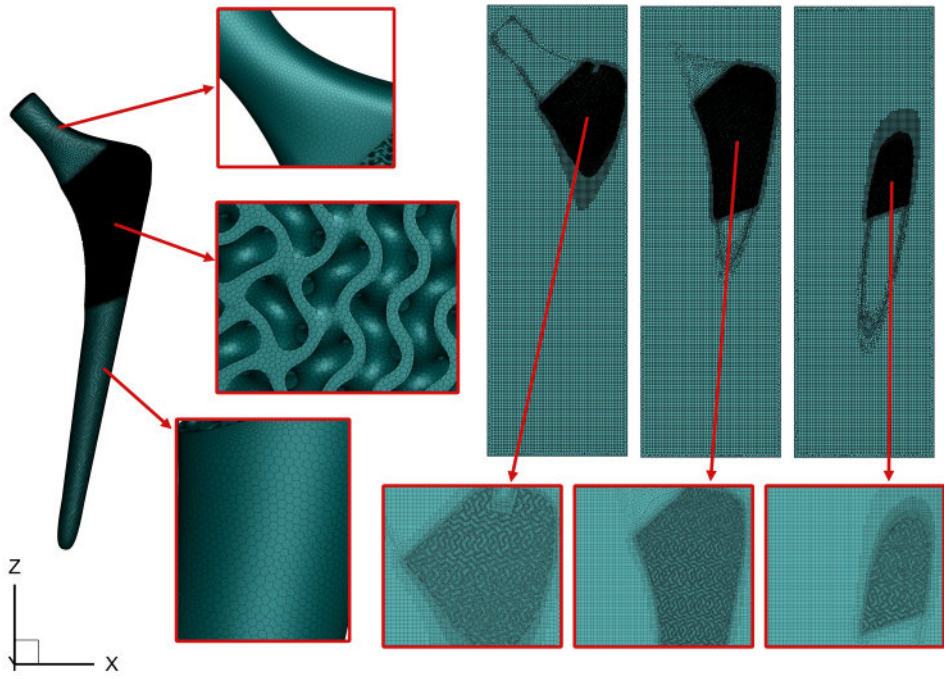

FIGURE 3.15: Mesh generation for CFD

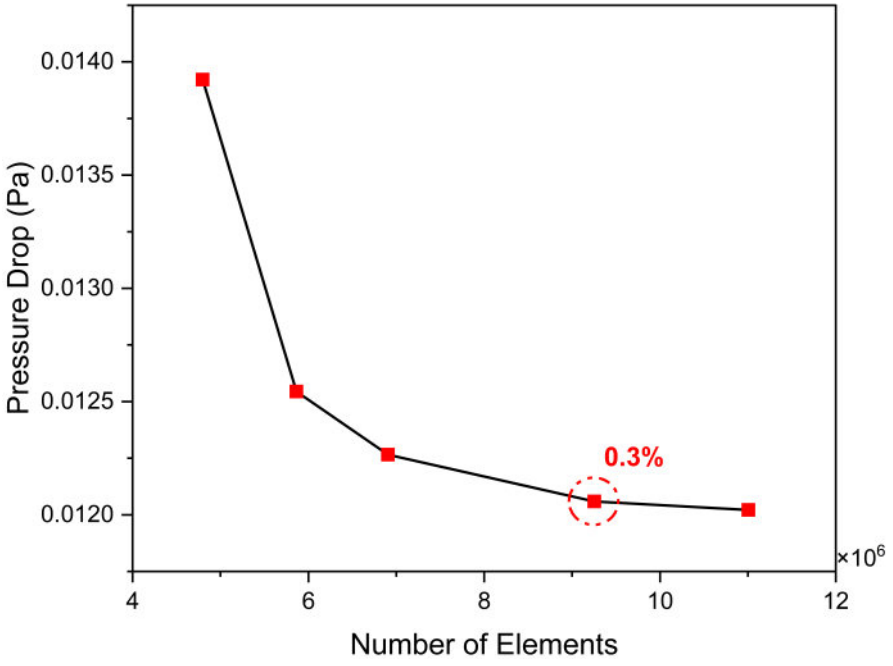

FIGURE 3.16: Mesh independence study for CFD analysis

million elements. The pressure drop across the structure was calculated for each mesh, and percentage differences were determined relative to the next finer mesh. Results showed an initial sensitivity to element size: the difference in pressure drop between 4.8 million and 5.8 million elements was 9.89%. Beyond this point, the results stabilized, with only a 0.3% change between 9.2 million and 11 million

elements. On this basis, a mesh with 9.2 million elements was adopted for all subsequent CFD simulations, since the variation in pressure drop was within the acceptable threshold of less than 1% compared to the finer mesh (Figure 3.16).

The mesh generation process was computationally demanding. All simulations were executed on a workstation equipped with an Intel Core i5-7200U processor (4 cores) and 16 GB RAM. Generating the final mesh with 9.2 million elements required approximately 32 hours. This specification highlights the balance achieved between computational feasibility and numerical accuracy in the adopted meshing strategy.

3.5.4 Boundary Conditions

Four inlet velocities ranging from 0.5 to 0.8 mm/s were selected for CFD simulation. This is the range of blood flow velocities reported in the literature [129, 130]. No-slip boundary condition was applied at the wall of the body, and zero-gauge pressure was applied at the outlet. Two TPMS-based femoral stems that were previously selected were used for CFD simulation. Assuming that the metallic-based scaffolds experienced negligible deformation during fluid flow enabled us to disregard any potential fluid-wall interactions in the CFD analysis [131].

3.5.5 Numerical Schemes

A coupled pressure–velocity scheme was employed to solve the governing equations. This scheme simultaneously computes the momentum and continuity equations, ensuring correct pressure–velocity coupling for incompressible flows. In the present case, this approach provided stable convergence, whereas segregated schemes showed slower or inconsistent convergence for the porous TPMS geometries considered. For gradient calculations, the Green–Gauss node-based method was selected. Alternative methods such as Green–Gauss cell-based or least-squares

cell-based were tested, but they did not converge the solution reliably for the current mesh configuration. The node-based approach provided consistent convergence and accurate reconstruction on the unstructured poly-hexcore mesh. Pressure interpolation was carried out using a second-order scheme to capture pressure variations across the domain. For the momentum equations, a first-order upwind scheme was adopted. In this case, attempts to use second-order upwind discretization led to divergence during the solution process. The first-order scheme, however, consistently provided stable convergence while maintaining acceptable accuracy for flow predictions.

3.5.6 Validation Study

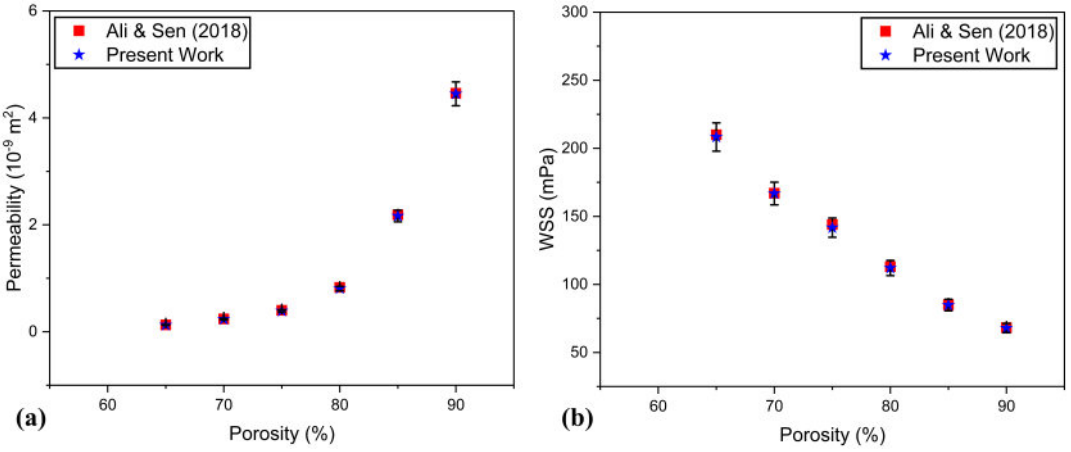

FIGURE 3.17: Numerical model validation (a) Permeability (b) WSS

The CFD model for non-Newtonian flow was validated by reproducing the gyroid TPMS geometry and simulation parameters reported by Ali and Sen [132], employing a power-law fluid model to represent non-Newtonian blood flow. Identical boundary conditions and material properties were used to ensure consistency with the reference study. The resulting permeability and WSS values showed strong agreement, with a maximum deviation of 2.5% in permeability and 1.6% in WSS, as presented in Figure 3.17. This validation, along with the adoption of a methodology consistent with our previous works [90, 131], confirms the accuracy of the CFD framework for simulating non-Newtonian fluid behavior in TPMS-based scaffold structures.

Chapter 4

Results and Discussion

4.1 FEA of Femoral Implant

4.1.1 Total Deformation in Femoral Stem

The finite element analysis (FEA) conducted on three distinct Ti–6Al–7Nb femoral stem designs (solid, Gyroid lattice, and Lidinoid lattice) yielded notable differences in total deformation under standardized physiological loading conditions (ISO 7206-4), as shown in Figure 4.1. The solid stem exhibited a maximum total deformation of 0.32 mm, serving as the baseline for comparison. By introducing internal porous structures, deformation significantly increased to 0.53 mm for the Gyroid lattice stem, marking an approximately 66% increase compared to the solid stem. The Lidinoid lattice stem further increased deformation to 0.68 mm, representing an additional 28% increment from the Gyroid-based design and a cumulative 113% increase compared to the solid baseline.

The lowest deformation observed in the solid stem design (0.32 mm) aligns with expectations for fully dense metallic implants, which typically possess higher stiffness and minimal compliance. Although such stiffness is beneficial from a purely structural perspective, minimizing risk of mechanical failure, it may adversely affect the implant's long-term clinical success. Specifically, the high stiffness of solid stems

limits the transfer of physiological loads to the adjacent femoral bone. As a result, these implants are associated with stress shielding, a condition in which reduced mechanical stimulus leads to decreased bone density, progressive bone resorption, and eventual loosening of the implant as reported in the literature [19, 38, 133]. In comparison, introducing a Gyroid-based lattice structure markedly increased

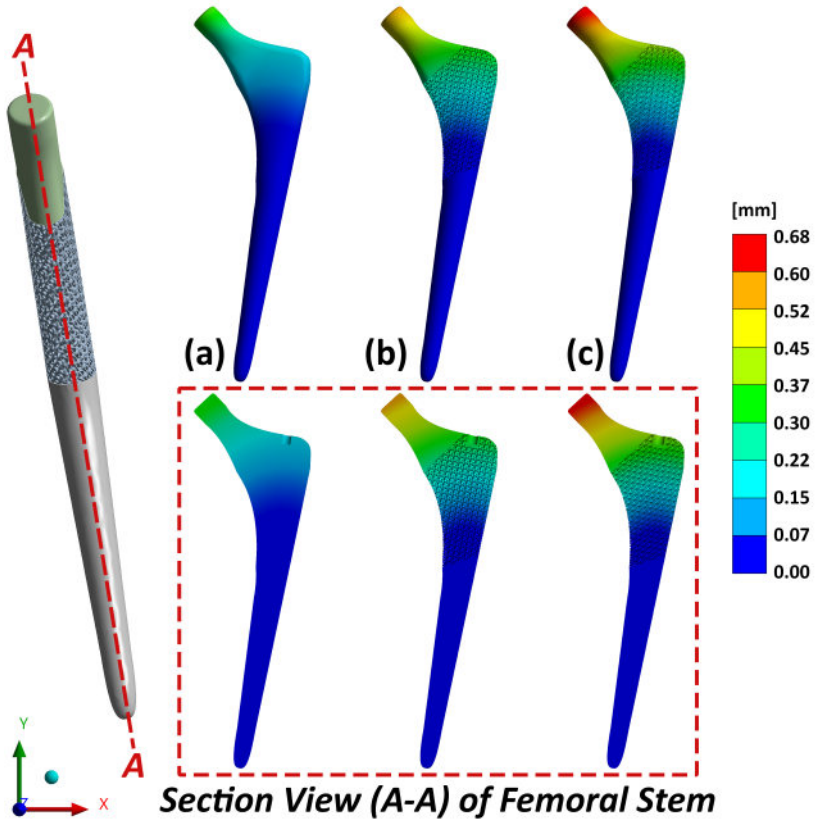

FIGURE 4.1: Total deformation (a) Solid femoral stem (b) Gyroid based femoral stem (c) Lidinoid based femoral stem

the total deformation to 0.53 mm. This increase in deformation arises due to the unique geometric characteristics of the Gyroid lattice, which includes smooth, continuous surfaces interconnected throughout the internal structure. Such geometry allows the Gyroid structure to better distribute mechanical loads and more closely replicate the biomechanical behavior of the natural bone environment. As a result, the Gyroid lattice significantly reduces the stiffness mismatch between the implant and surrounding bone. This reduction in stiffness mismatch promotes physiological loading, which can facilitate optimal stress distribution to the femoral bone, potentially improving long-term bone remodeling and reducing the likelihood and severity of stress shielding.

The highest deformation was observed with the Lidinoid lattice structure (0.68 mm). This further increase in compliance relative to the Gyroid structure results from the inherent geometric features of the Lidinoid topology, characterized by larger pore spaces, more elongated struts, and an open network structure. Such a highly porous design maximizes the deformation and flexibility of the stem, enhancing load transfer capabilities. Although this deformation is significantly higher than that of the solid and Gyroid designs, it remains within the acceptable deformation range that previous studies have associated with effective stress transfer [65]. The Lidinoid structure's high compliance could thus further diminish stress shielding by closely matching the mechanical behavior of native bone tissue, promoting a more physiological strain environment around the implant.

From a clinical standpoint, the deformation characteristics identified in this study have essential implications for implant design. Solid stems, despite their robust structural integrity, risk severe stress shielding, potentially compromising long-term bone health and implant fixation. In contrast, both Gyroid and Lidinoid porous designs enhance mechanical compatibility and physiological loading. Gyroid structures, showing moderate compliance (0.53 mm deformation), are highly favorable due to their balanced mechanical behavior, ensuring adequate physiological stimulus for the femoral bone. Lidinoid structures, while demonstrating even greater flexibility (0.68 mm deformation), also hold substantial potential for reducing stress shielding.

4.1.2 Von Mises Stress on Femoral Stem

The von Mises stress distribution was evaluated for three femoral stem designs (solid, Gyroid TPMS, and Lidinoid TPMS) under physiological loading conditions as defined by ISO 7206-4, are shown in Figure 4.2. All stems were modeled using the titanium alloy Ti–6Al–7Nb and effective Young's modulus values obtained from asymptotic homogenization (AH).

The solid stem recorded the lowest maximum von Mises stress at 294.51 MPa, with an average stress of only 3.74 MPa, reflecting its highly stiff and non-compliant

structure. In comparison, the Gyroid TPMS stem exhibited a maximum stress of 661.17 MPa, which is approximately 124.5% higher than that of the solid stem. The average stress for the Gyroid stem was 177.91 MPa, indicating a notable enhancement in internal load transfer. The Lidinoid TPMS stem demonstrated the highest maximum von Mises stress of 917.3 MPa, representing a 211.5% increase over the solid stem and about 38.8% higher than the Gyroid structure. Its average stress was 204.04 MPa, slightly greater than that of the Gyroid stem. The

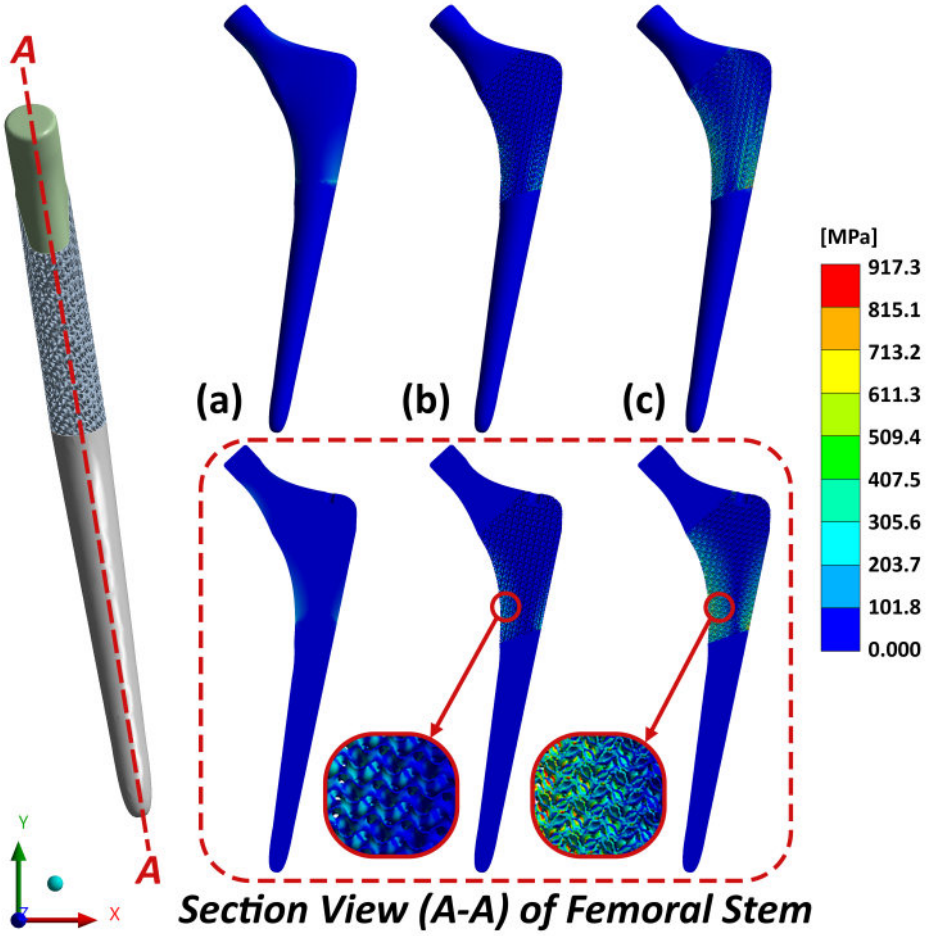

FIGURE 4.2: Von-mises stress (a) Solid femoral stem (b) Gyroid based femoral stem (c) Lidinoid based femoral stem

solid femoral stem, composed entirely of dense Ti–6Al–7Nb, exhibited the lowest average and maximum stress values, as expected from a structure with minimal internal compliance. While this ensures excellent mechanical strength and structural reliability, it also implies minimal physiological stress transfer to the surrounding bone, thereby raising concerns about stress shielding. The low average von Mises stress (3.74 MPa) suggests that most of the load is absorbed by the implant itself,

reducing mechanical stimulation to the surrounding femur, a key contributor to periprosthetic bone resorption over time.

In contrast, the Gyroid TPMS-based stem showed a substantial increase in both maximum and average von Mises stresses. The Gyroid's mathematically smooth and continuous surface allows for homogeneous stress propagation across its periodic unit cells. With an average stress of 177.91 MPa, the Gyroid stem facilitates much greater physiological load transfer to adjacent bone. This behavior is favorable in preventing stress shielding, maintaining bone density, and improving osseointegration. Importantly, its maximum stress (661.17 MPa) remains well below the yield strength of Ti–6Al–7Nb, ensuring mechanical safety under normal physiological loads.

The Lidinoid TPMS stem exhibited even higher stress levels, with an average von Mises stress of 204.04 MPa and a peak value of 917.3 MPa. The Lidinoid surface, defined by more spatially complex minimal surfaces and less uniform load paths, allows more localized stress accumulation. This could improve load sharing but also introduces regions where stress exceeds the material's yield strength, suggesting a narrower safety margin compared to the Gyroid design. However, due to the absence of stress concentrators (as in strut-based lattices), even high stresses in TPMS structures are generally more tolerable under fatigue conditions [134].

The von Mises stress outcomes of the solid, Gyroid, and Lidinoid femoral stems hold critical implications for the long-term clinical performance of hip implants. The low stress values in the solid stem, while indicating high structural stability, pose a considerable risk of stress shielding, a phenomenon wherein the surrounding bone experiences diminished mechanical loading. Over time, this can result in bone resorption, reduced osseointegration, and eventually implant loosening, a major cause of revision surgeries in total hip arthroplasty (THA) [133]. In contrast, the elevated average von Mises stresses in the Gyroid (177.91 MPa) and Lidinoid (204.04 MPa) stems suggest improved physiological load transfer to the bone, which is crucial for maintaining bone density and ensuring long-term fixation stability. TPMS-based designs, by mimicking the mechanical behavior of

cancellous bone, foster biomechanical compatibility and promote adaptive bone remodeling, thereby reducing periprosthetic bone loss. Among these, the Gyroid stem appears to offer the best balance, promoting load transfer while maintaining mechanical safety margins. The Lidinoid, while promising, may require careful geometric optimization to prevent potential overloading in localized regions.

4.2 CFD of Femoral Implant

4.2.1 Newtonian Fluid

4.2.1.1 Fluidic Characteristics

The analysis of pressure drop across both the Gyroid and Lidinoid structures under Newtonian fluid flow reveals a clear trend that aligns with fundamental fluid dynamics principles. As expected, the pressure drop increases with fluid velocity in both structures, indicating that higher velocities result in greater fluid resistance. This phenomenon is a natural outcome of laminar flow behavior in porous media, where resistance increases with velocity. The Gyroid structure, with its continuous, interlinked pores, demonstrates a relatively lower pressure drop, with values ranging from 0.0120217 Pa at 0.5 mm/s to 0.01962521 Pa at 0.8 mm/s. This smooth increase in pressure drop with velocity is consistent with the laminar flow regime, where pressure drop is proportionally linked to velocity for Newtonian fluids. Table 4.1 shows the pressure drop values at different velocities for Gyroid and Lidinoid structures. In contrast, the Lidinoid structure exhibits slightly higher pressure drop values for each corresponding velocity, with values ranging from 0.01205901 Pa at 0.5 mm/s to 0.019649 Pa at 0.8 mm/s. This indicates that despite the similar porosity between the two structures, the Lidinoid introduces greater resistance to fluid flow. The higher pressure drop in the Lidinoid structure is likely due to the more complex geometry of its pore network, which may create more local resistance to flow. This is consistent with findings in the literature, where complex pore geometries have been shown to cause higher resistance and

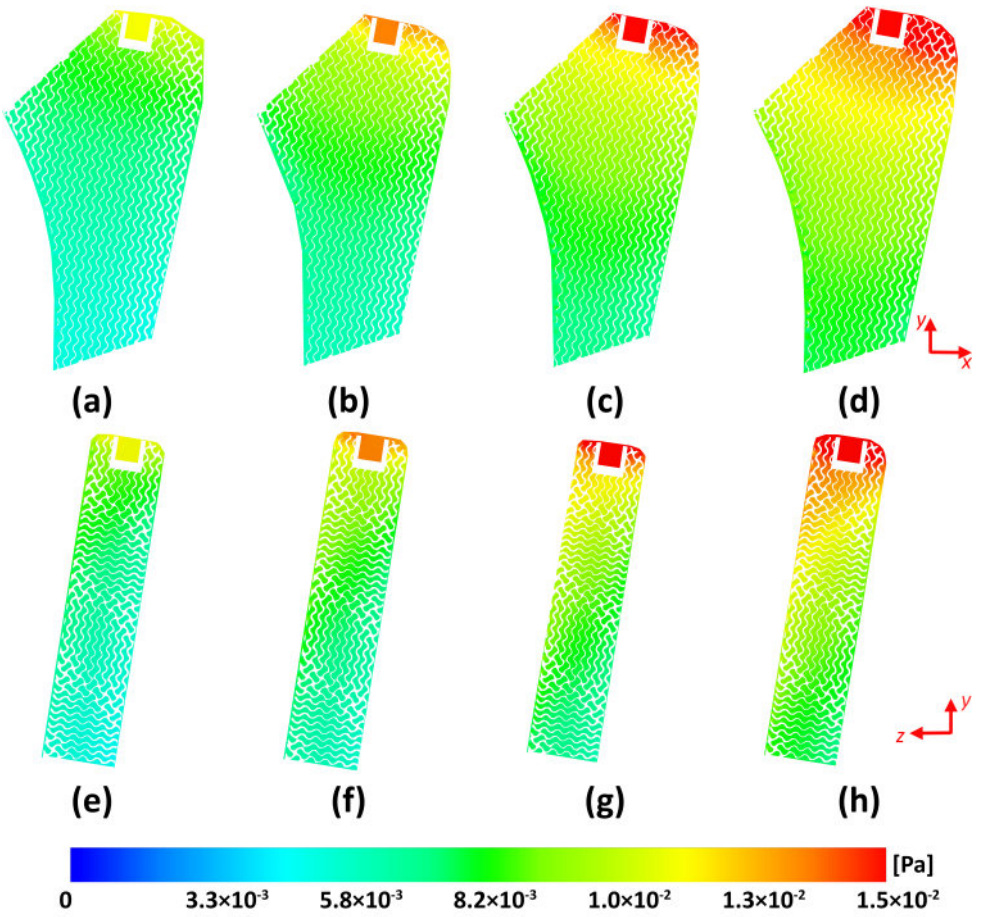

FIGURE 4.3: Pressure contour distribution of newtonian fluid through gyroid structure at varying inlet velocities: (a) 0.5 mm/s, (b) 0.6 mm/s, (c) 0.7 mm/s, and (d) 0.8 mm/s. (e)–(h) represent alternate views of the same simulations, showing pressure variations along yz axes.

greater pressure drop due to turbulence and irregular flow paths [77, 90]. For instance, in bone scaffolds, similar effects have been observed where complex lattice geometries increase the friction and resistance to fluid flow, thereby increasing pressure drops and limiting fluid transport efficiency [135]. The pressure and velocity contours further elucidate the fluid dynamics within both the Gyroid and Lidinoid structures, offering insight into how the scaffold's geometry influences fluid flow in the femoral stem implants. Pressure contours in both structures reveal that the highest pressure occurs at the inlet, where the fluid enters the scaffold (Figures 4.3 and 4.4). From there, the pressure gradually decreases toward the outlet. This is typical behavior, reflecting the resistance to flow within the scaffold. However, the Gyroid structure demonstrates a smoother and more uniform pressure distribution compared to the Lidinoid structure. The Gyroid's

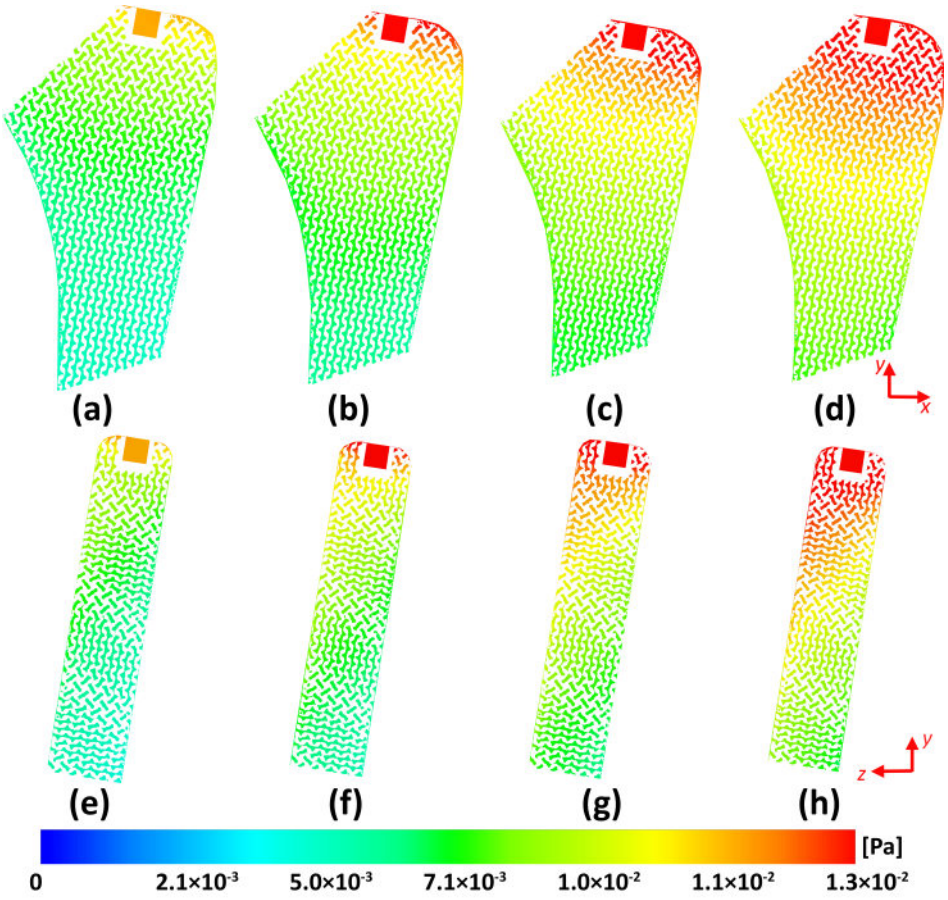

FIGURE 4.4: Pressure contour distribution of newtonian fluid through lidinoid structure at varying inlet velocities: (a) 0.5 mm/s, (b) 0.6 mm/s, (c) 0.7 mm/s, and (d) 0.8 mm/s. (e)–(h) represent alternate views of the same simulations, showing pressure variations along yz axes.

continuous pore network allows the fluid to flow more efficiently, leading to a lower pressure drop across the structure. This suggests that the Gyroid would facilitate more uniform fluid distribution across the femoral stem, which is beneficial for enhancing the biological fixation of the implant.

The Lidinoid structure, with its more abrupt changes and less optimized flow pathways, shows steeper pressure gradients in the contours (Figure 4.4). These regions of high pressure are typically indicative of flow restrictions, where the fluid faces resistance due to the complex geometry of the scaffold. This could potentially create localized high-pressure zones that might hinder the fluid flow needed for optimal vascularization and nutrient exchange in the early stages following implantation. The pressure variations within the Lidinoid structure suggest that

TABLE 4.1: Pressure drop at different velocities for Gyroid and Lidinoid structures

Structure Type	Velocity (mm/sec)	Pressure Drop (Pa)
Gyroid	0.5	0.0120217
	0.6	0.01452074
	0.7	0.01705492
	0.8	0.01962521
Lidinoid	0.5	0.01205901
	0.6	0.01455632
	0.7	0.01708596
	0.8	0.019649

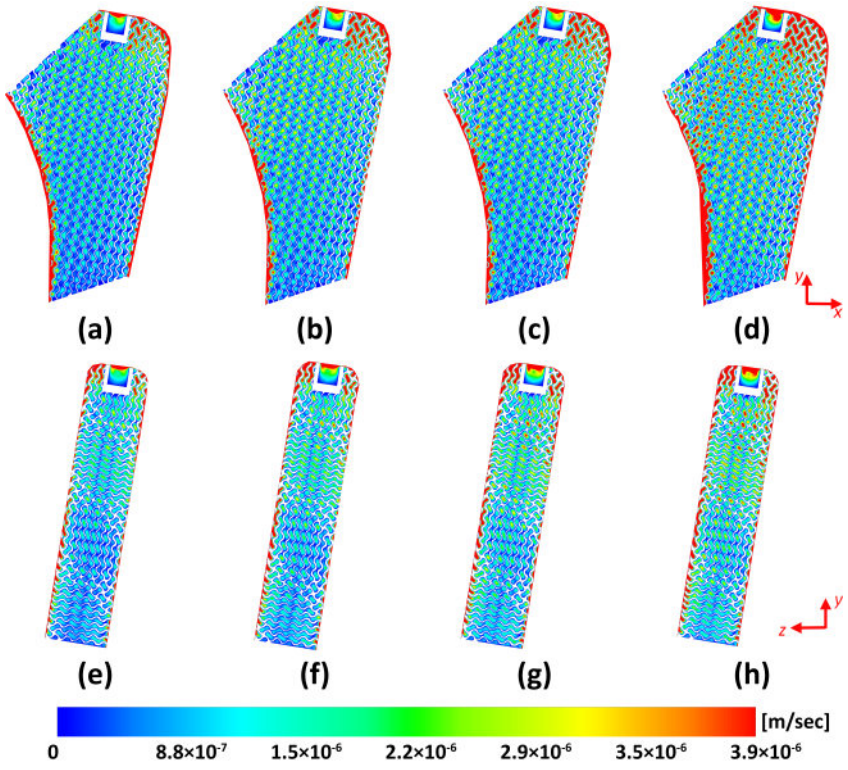

FIGURE 4.5: Velocity contour distribution of newtonian fluid through gyroid structure at varying inlet velocities: (a) 0.5 mm/s, (b) 0.6 mm/s, (c) 0.7 mm/s, and (d) 0.8 mm/s. (e)–(h) represent alternate views of the same simulations, showing velocity variations along yz axes.

while it might still perform adequately, its efficiency in promoting osseointegration might be compromised in comparison to the Gyroid structure.

When the velocity contours were examined, the Gyroid structure exhibits a more uniform velocity profile, suggesting that the fluid flows steadily through the scaffold with minimal obstructions as shown in Figure 4.5. This is particularly advantageous in a femoral stem, where fluid flow within the scaffold plays a significant

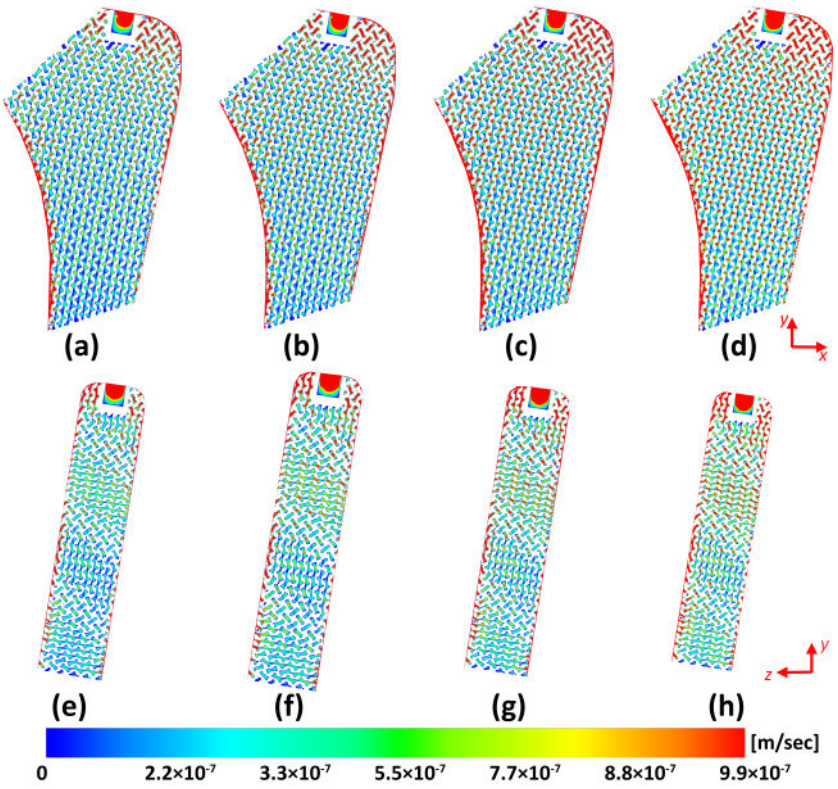

FIGURE 4.6: Velocity contour distribution of newtonian fluid through lidinoid structure at varying inlet velocities: (a) 0.5 mm/s, (b) 0.6 mm/s, (c) 0.7 mm/s, and (d) 0.8 mm/s. (e)–(h) represent alternate views of the same simulations, showing velocity variations along yz axes.

role in bone cell migration and osteoblast proliferation, crucial for the biological fixation of the implant. In comparison, the Lidinoid structure displays localized high-velocity regions within larger pores, while smaller pores exhibit lower velocities, leading to non-uniform fluid movement as shown in Figure 4.6. This irregular flow could hinder the homogeneous distribution of nutrients and oxygen, which are vital for promoting bone ingrowth and the overall success of the femoral stem.

The trends observed in both pressure drop and velocity have significant implications for the design of femoral stems. In THA, the femoral stem is designed not only to provide mechanical support but also to facilitate biological processes such as osseointegration. Efficient fluid transport is essential for the early stages of implant integration, where the delivery of nutrients and oxygen to the bone tissue is critical for proper healing. The Gyroid structure, with its optimized flow properties, is well-suited for applications where vascularization and bone growth are prioritized, making it a more favorable option for biocompatible femoral stem

designs. Conversely, while the Lidinoid structure may provide structural strength, its less efficient fluid dynamics could limit its ability to promote biological fixation as effectively as the Gyroid. This makes the Gyroid structure a better choice for the stem, especially where nutrient and oxygen delivery to the surrounding bone is critical.

4.2.1.2 Permeability

The permeability analysis under Newtonian fluid flow conditions provides further insight into the effectiveness of scaffold geometries for facilitating interstitial fluid transport, an essential requirement for bone regeneration and osseointegration in femoral stem. The permeability values, calculated using Darcy's law, are shown in the Table 4.2 for both Gyroid and Lidinoid structures at different inlet velocities. The results reveal that the permeability values for both scaffold types decrease

TABLE 4.2: Permeability at different velocities for Gyroid and Lidinoid structures

Structure Type	**Velocity (mm/sec)**	**Permeability (m^2)**
Gyroid	0.5	1.208×10^{-5}
	0.6	1.200×10^{-5}
	0.7	1.192×10^{-5}
	0.8	1.184×10^{-5}
Lidinoid	0.5	1.204×10^{-5}
	0.6	1.197×10^{-5}
	0.7	1.190×10^{-5}
	0.8	1.182×10^{-5}

gradually as the inlet velocity increases. This trend is also reported in the literature [135]. This inverse relationship between velocity and permeability is expected, as Darcy's law assumes a linear flow regime, but local flow disturbances and resistance can lead to reduced effective permeability at higher velocities. Importantly, the Gyroid structure consistently shows slightly higher permeability compared to the Lidinoid across all velocities.

This trend is indicative of the Gyroid's superior fluidic architecture, where its smooth, periodic surface geometry offers more direct and continuous pathways for fluid transport. The nature of the Gyroid structure results in minimal curvature

discontinuities and the absence of sharp pore junctions, which reduces viscous dissipation and promotes better fluid flow. Such features are particularly favorable in femoral stems, where consistent and unhindered nutrient diffusion through the porous lattice is essential for initiating and sustaining bone cell viability and angiogenesis post-implantation.

In contrast, the Lidinoid structure, while also a TPMS variant, may contain more tortuous paths or higher surface area contact points that increase hydraulic resistance. This results in marginally lower permeability values, e.g., at 0.5 mm/s, the Lidinoid permeability is 1.20408×10^{-5} m^2, slightly below the Gyroid's 1.20782×10^{-5} m^2. Although the difference is subtle, it can have meaningful biological implications. Therefore, even small gains in permeability, particularly in anatomically sensitive regions like the femoral canal, can accelerate bone ingrowth and biological fixation.

Moreover, the decline in permeability with increasing velocity in both structures aligns with the findings of Ali and Sen [135], who demonstrated that scaffold permeability measured under Newtonian assumptions decreases under conditions of higher flow-induced resistance, particularly in dense or complex lattice geometries. While Darcy's law is valid under low-Reynolds laminar conditions, deviations occur as micro-scale inertial effects become significant. In the current study, the relatively stable permeability across all velocities reflects good lattice design within both the Gyroid and Lidinoid, but the Gyroid's architecture still maintains a functional advantage, making it more suitable for high-performance femoral stem scaffolds.

From a clinical design perspective, femoral stems incorporating a Gyroid-based porous structure may facilitate superior fluid exchange between the implant surface and bone marrow cavity. This would enhance early-stage healing, reduce the risk of aseptic loosening, and support the long-term success of uncemented total hip arthroplasty (THA). By contrast, the slightly lower permeability in Lidinoid-based stems may hinder early-stage vascularization and cellular penetration, especially under limited physiological loading conditions.

4.2.1.3 Wall Shear Stress (WSS)

The wall shear stress (WSS), which quantifies the tangential force exerted by the fluid on the surface of the scaffold, plays a crucial role in influencing osteoblast behavior, vascularization, and bone tissue regeneration. WSS is one of the key mechanical cues that regulates cellular activities such as cell attachment, differentiation, and proliferation, all of which are essential for the osseointegration process in femoral stem. Table 4.3 presents the WSS values for both the Gyroid and Lidinoid structures across a range of velocities.

TABLE 4.3: WSS at different velocities for Gyroid and Lidinoid structures

Structure Type	**Velocity (mm/sec)**	**Wall Shear Stress (Pa)**
Gyroid	0.5	1.75214×10^{-4}
	0.6	2.10976×10^{-4}
	0.7	2.47027×10^{-4}
	0.8	2.83380×10^{-4}
Lidinoid	0.5	1.64196×10^{-4}
	0.6	1.97610×10^{-4}
	0.7	2.31259×10^{-4}
	0.8	2.65156×10^{-4}

The results show that wall shear stress (WSS) increases with fluid velocity in both scaffold types, as anticipated in laminar flow regimes where the shear stress is directly proportional to the fluid velocity. This increase in WSS with velocity is a typical response, reflecting the increased friction between the fluid and the scaffold surface.

In terms of scaffold geometry, the Gyroid structure consistently exhibits higher WSS values than the Lidinoid structure. For example, at a velocity of 0.5 mm/s, the Gyroid scaffold generates 1.75214×10^{-4} Pa of shear stress, which increases to 2.8338×10^{-4} Pa at 0.8 mm/s. By comparison, the Lidinoid scaffold at 0.5 mm/s produces 1.64196×10^{-4} Pa, which increases to 2.65156×10^{-4} Pa at 0.8 mm/s.

The Gyroid structure's higher wall shear stress values can be attributed to its continuous, interconnected pore network, which allows for smoother fluid flow. As a result, the fluid is able to achieve higher velocities at the scaffold walls, generating a higher shear stress. The Gyroid structure's geometry is highly efficient for

facilitating osteoblast activation and vascular growth within the scaffold, as higher shear stress has been linked to enhanced bone regeneration and angiogenesis.

Conversely, the Lidinoid structure, with its more complex and potentially less optimized flow pathways, generates lower shear stress compared to the Gyroid. Although the Lidinoid still exhibits an increasing trend in shear stress with increasing velocity, its values are consistently lower than those of the Gyroid for the same velocity. For instance, at 0.5 mm/s, the Lidinoid WSS is 1.64196×10^{-4} Pa, compared to 1.75214×10^{-4} Pa in the Gyroid. This lower shear stress in the Lidinoid structure might result in less stimulating force on osteoblasts, potentially leading to slower osseointegration and bone regeneration. However, the Lidinoid structure's lower shear stress could be beneficial in preventing excessive mechanical stress on the implant, which could be important in scenarios where gentler shear forces are required to avoid damage to delicate cellular structures during the initial stages of healing.

Recent studies have explored the impact of wall shear stress on osseointegration in scaffolds, confirming the significance of moderate shear stress in cellular differentiation and bone regeneration [136]. Ali et al. [88], using TPMS scaffolds, showed that higher shear stress promotes vascularization and osteoblast activation, essential for successful osseointegration.

In femoral stem design for total hip arthroplasty (THA), the Gyroid scaffold's higher wall shear stress is particularly advantageous. Wall shear stress is a key factor in stimulating osteoblast activation, bone remodeling, and vascular ingrowth, all of which are critical for the successful biological fixation of the femoral stem. The Gyroid scaffold, with its higher shear stress, is likely to enhance osseointegration and early-stage healing, making it an ideal candidate for femoral stem designs where biological fixation is prioritized.

In contrast, the Lidinoid scaffold, while still showing an increase in wall shear stress with velocity, produces lower values compared to the Gyroid. While it may still support osseointegration, it may not be as effective in promoting rapid vascularization and osteoblast differentiation during the early stages of implantation.

Therefore, Gyroid-based femoral stems are likely to provide faster and more reliable fixation, ensuring better long-term outcomes for patients undergoing hip replacement surgery.

4.2.2 Non-Newtonian Fluid

4.2.2.1 Fluidic Characteristics

The results of the pressure drop and velocity distribution for the Non-Newtonian fluid flow case reveal important insights into the fluid dynamics within the Gyroid and Lidinoid scaffold architectures. The pressure drop and velocity are crucial factors for determining the permeability and efficiency of nutrient and oxygen delivery in scaffolds used for bone tissue engineering applications, especially for femoral stem implants where fluid dynamics play a key role in osteointegration and vascularization. As with the Non-Newtonian fluid flow, the pressure drop increases with the fluid velocity in both scaffold types, as shown in the Table 4.4. As the velocity increases, both the Gyroid and Lidinoid scaffolds exhibit a proportional increase in pressure drop, which is expected in laminar flow conditions. The Gyroid structure consistently shows a slightly lower pressure drop at each corresponding velocity compared to the Lidinoid structure, with values of 0.09478691 Pa at 0.5 mm/s increasing to 0.1325383 Pa at 0.8 mm/s. In comparison, the Lidinoid structure shows pressure drop values ranging from 0.09512049 Pa at 0.5 mm/s to 0.1329508 Pa at 0.8 mm/s, indicating slightly higher resistance to flow.

TABLE 4.4: Pressure drop at different velocities for Gyroid and Lidinoid structures

Structure Type	Velocity (mm/sec)	Pressure Drop (Pa)
Gyroid	0.5	0.09478691
	0.6	0.1079309
	0.7	0.1204767
	0.8	0.1325383
Lidinoid	0.5	0.09512049
	0.6	0.1082967
	0.7	0.1208687
	0.8	0.1329508

This behavior can be attributed to the differences in the structural geometry of

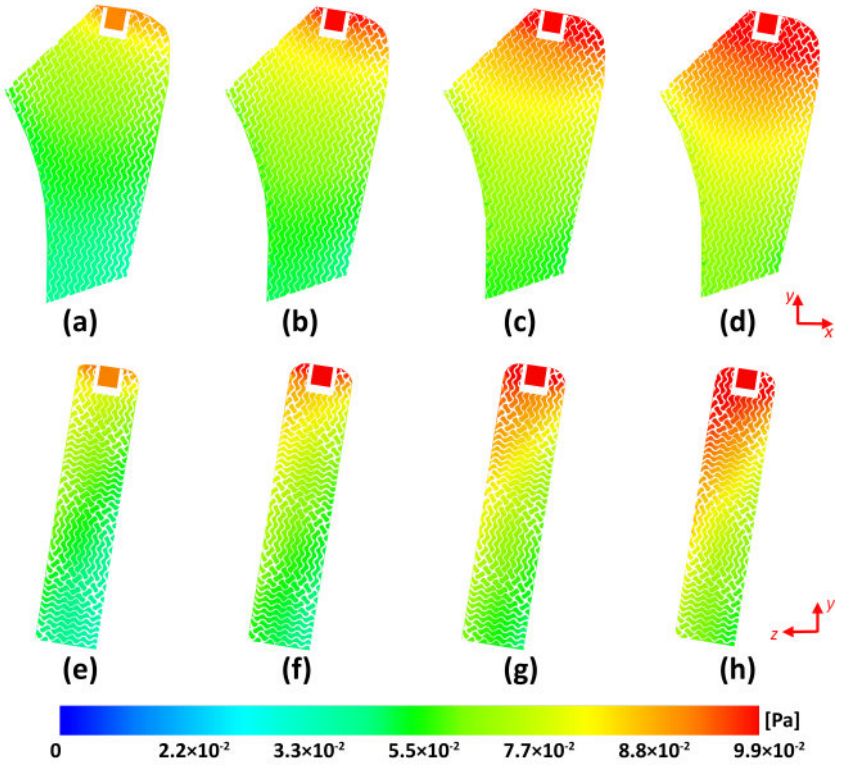

FIGURE 4.7: Pressure contour distribution of non-newtonian fluid through gyroid structure at varying inlet velocities: (a) 0.5 mm/s, (b) 0.6 mm/s, (c) 0.7 mm/s, and (d) 0.8 mm/s. (e)–(h) represent alternate views of the same simulations, showing pressure variations along yz axes.

the two scaffolds. The Gyroid structure, with its smooth, continuous pores, allows for more efficient fluid flow and lower resistance compared to the Lidinoid structure, which likely has more constricted channels that cause higher fluid resistance and a higher pressure drop at the same flow rates. These results are consistent with findings from Ali and Sen [135], who observed similar differences in pressure drop for TPMS-based scaffolds under both Newtonian and non-Newtonian fluid flow conditions. The pressure contours for both the Gyroid and Lidinoid scaffolds under non-Newtonian fluid flow exhibit significant differences due to the fluid's shear-thinning behavior. In both scaffolds, the highest pressure is observed near the inlet where the fluid first enters the scaffold, as shown in Figure 4.7 and 4.8. As the fluid travels through the scaffold, the pressure gradually decreases toward the outlet, which is consistent with expected fluid flow behavior. In the Gyroid scaffold, the pressure distribution is relatively uniform, with a smooth decline from the inlet to the outlet. This indicates that the continuous, interconnected pores

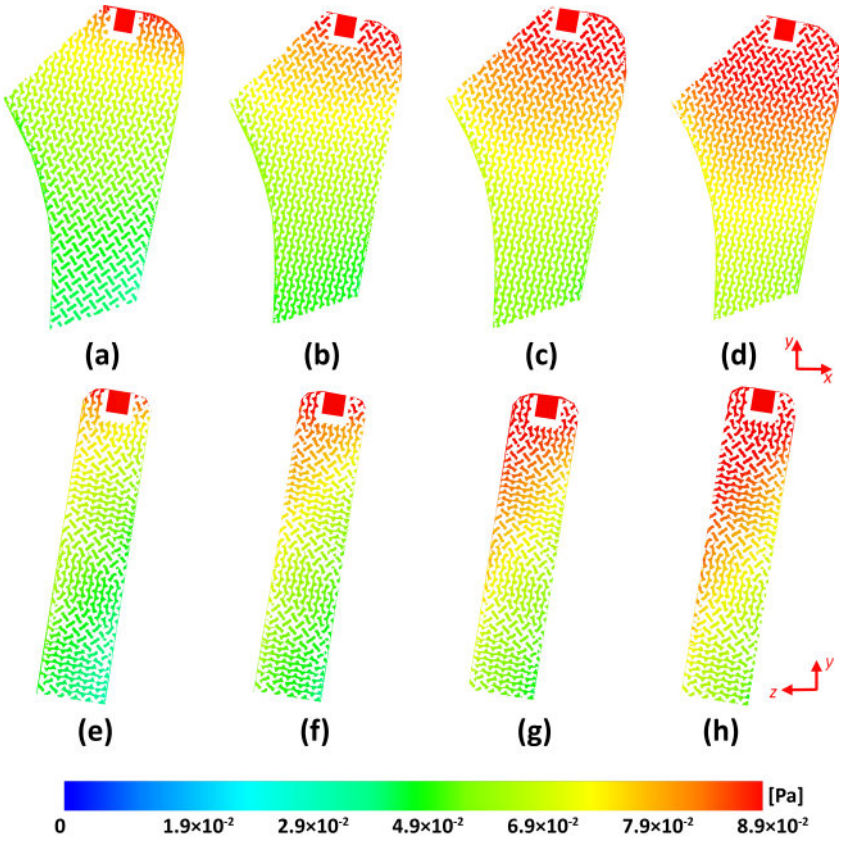

FIGURE 4.8: Pressure contour distribution of non-newtonian fluid through lidinoid structure at varying inlet velocities: (a) 0.5 mm/s, (b) 0.6 mm/s, (c) 0.7 mm/s, and (d) 0.8 mm/s. (e)–(h) represent alternate views of the same simulations, showing pressure variations along yz axes.

in the Gyroid structure allow the fluid to flow efficiently with minimal resistance, causing less fluctuation in pressure.

Conversely, in the Lidinoid scaffold, the pressure contours are steeper, indicating regions where the fluid faces greater resistance due to more complex, tortuous flow paths. These areas of high pressure are typically caused by constricted channels and sharp turns in the scaffold geometry, which hinder smooth fluid movement. This behavior aligns with the shear-thinning nature of the non-Newtonian fluid, where the viscosity decreases with increasing shear rate. The Lidinoid structure's less efficient pore network results in higher localized pressures compared to the Gyroid structure, where the flow is more streamlined. The velocity contours for non-Newtonian flow further illustrate the differences in fluid dynamics between the two scaffold geometries. In the Gyroid scaffold, the velocity is more evenly distributed, indicating smooth and consistent fluid flow as shown in Figure 4.9. This

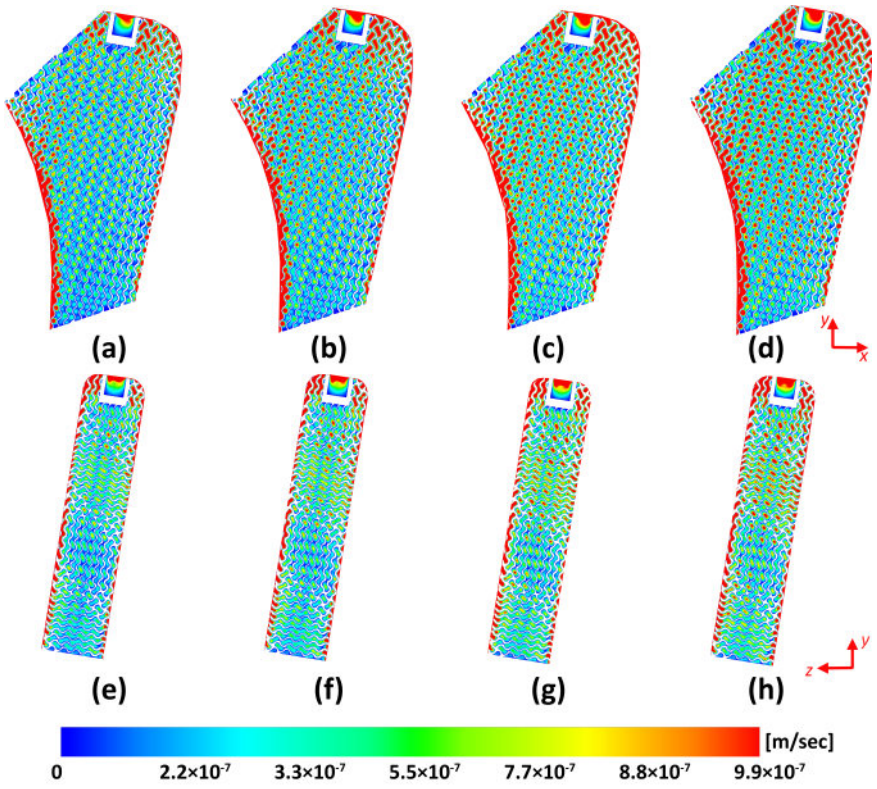

FIGURE 4.9: Velocity contour distribution of non-newtonian fluid through gyroid structure at varying inlet velocities: (a) 0.5 mm/s, (b) 0.6 mm/s, (c) 0.7 mm/s, and (d) 0.8 mm/s. (e)–(h) represent alternate views of the same simulations, showing velocity variations along yz axes.

uniformity is due to the continuous pore network of the Gyroid, which facilitates a more efficient and stable flow path for the fluid, resulting in less variation in velocity across the structure. Higher velocities are observed in the larger pores, while smaller pores show lower velocities, but the overall distribution remains relatively stable. In the Lidinoid scaffold, the velocity distribution is more non-uniform, with noticeable regions of high velocity in the larger pores and low velocity in the narrower regions. This pattern is a result of the tortuous flow paths in the Lidinoid structure, where fluid is forced to slow down in tighter channels and accelerate in more open areas, leading to significant velocity fluctuations as shown Figure 4.10. In the femoral stem design for THA, the results of this non-Newtonian fluid flow analysis have significant implications for scaffold design. Gyroid scaffolds, with their lower pressure drop and more uniform velocity distribution, are more effective at promoting vascularization and osteoblast differentiation, which are essential for successful osseointegration of the femoral stem. The higher pressure

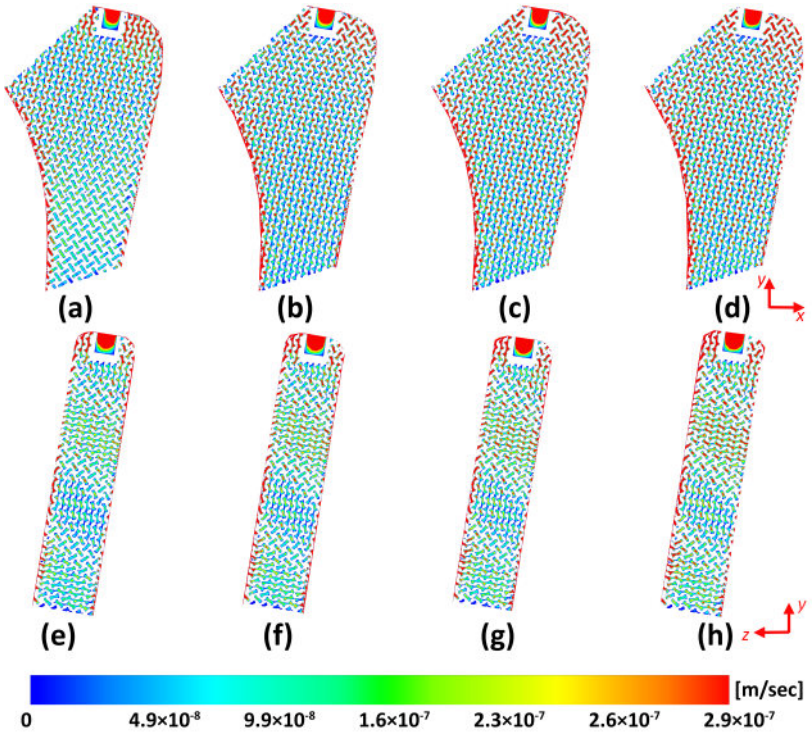

FIGURE 4.10: Velocity contour distribution of non-newtonian fluid through lidinoid structure at varying inlet velocities: (a) 0.5 mm/s, (b) 0.6 mm/s, (c) 0.7 mm/s, and (d) 0.8 mm/s. (e)–(h) represent alternate views of the same simulations, showing velocity variations along yz axes.

and velocity variations observed in the Lidinoid scaffold might hinder efficient fluid transport, making the Gyroid scaffold a more suitable choice for femoral stems that require optimal biological fixation.

4.2.2.2 Permeability

The permeability of the Gyroid and Lidinoid scaffolds under non-Newtonian fluid flow is an important factor in determining the fluid transport efficiency and overall biological performance of bone tissue engineering scaffolds. The permeability values, as shown in the Table 4.5, reflect the ability of the scaffolds to allow fluid flow through their porous structures. The permeability values for both Gyroid and Lidinoid structures are very close across all velocities, with values decreasing slightly as the velocity increases. In the Gyroid scaffold, permeability ranges from 5.83234×10^{-6} m^2 at 0.5 mm/s to 5.81197×10^{-6} m^2 at 0.8 mm/s. Similarly, in the

TABLE 4.5: Permeability at different velocities for Gyroid and Lidinoid structures

Structure Type	**Velocity (mm/sec)**	**Permeability (m^2)**
Gyroid	0.5	5.83234×10^{-6}
	0.6	5.82595×10^{-6}
	0.7	5.81915×10^{-6}
	0.8	5.81197×10^{-6}
Lidinoid	0.5	5.80347×10^{-6}
	0.6	5.79818×10^{-6}
	0.7	5.79252×10^{-6}
	0.8	5.78651×10^{-6}

Lidinoid scaffold, permeability values range from 5.80347×10^{-6} m^2 at 0.5 mm/s to 5.78651×10^{-6} m^2 at 0.8 mm/s.

While the Gyroid scaffold exhibits slightly higher permeability than the Lidinoid scaffold, the differences between the two structures are minimal. This suggests that both scaffold types have relatively similar fluid flow characteristics under non-Newtonian conditions, although the Gyroid still offers marginally better fluid transport efficiency. This slight variation can be attributed to the geometry of the scaffolds; the Gyroid, with its more continuous pore network, typically facilitates smoother fluid flow, whereas the more complex geometry of the Lidinoid structure could slightly impede flow, resulting in a slightly lower permeability.

The observed slight decrease in permeability with increasing velocity is consistent with the findings from Ali and Sen [135], who reported similar results in scaffolds for bone tissue engineering. The non-Newtonian behavior of blood means that at higher flow velocities, the fluid experiences viscosity changes, affecting the overall permeability of the scaffold.

For femoral stem design, the permeability values of both scaffolds under non-Newtonian fluid flow indicate that both the Gyroid and Lidinoid structures are capable of supporting effective nutrient and oxygen transport, although the Gyroid structure may offer a slightly better fluid flow environment for bone cell migration and osteoblast proliferation. This enhanced permeability in the Gyroid scaffold could improve vascularization and osseointegration, crucial for the success of femoral stem implants in total hip arthroplasty (THA). The Lidinoid

scaffold, while having slightly lower permeability, may still be suitable for applications where mechanical strength is prioritized over fluid transport. However, for femoral stems where rapid osteointegration and vascular growth are essential for implant success, the Gyroid scaffold's slightly better permeability would make it a more favorable choice.

4.2.2.3 Wall Shear Stress (WSS)

The wall shear stress (WSS) for both Gyroid and Lidinoid scaffolds under non-Newtonian fluid flow was calculated at different velocities. Wall shear stress is a crucial parameter in bone tissue engineering, influencing the biomechanical stimulation of cells, especially osteoblasts, and playing a key role in osteointegration and vascularization in scaffolds. Table presents the WSS values for both the Gyroid and Lidinoid structures.

TABLE 4.6: WSS at different velocities for Gyroid and Lidinoid structures

Structure Type	**Velocity (mm/sec)**	**Wall Shear Stress (Pa)**
Gyroid	0.5	1.39442×10^{-3}
	0.6	1.58717×10^{-3}
	0.7	1.77088×10^{-3}
	0.8	1.94724×10^{-3}
Lidinoid	0.5	1.30586×10^{-3}
	0.6	1.48623×10^{-3}
	0.7	1.65813×10^{-3}
	0.8	1.82312×10^{-3}

The wall shear stress (WSS) values increase with increasing velocity for both scaffolds, as expected, since higher flow velocities lead to greater fluid friction and shear forces at the walls. For the Gyroid scaffold, the WSS increases from 1.39442×10^{-3} Pa at 0.5 mm/s to 1.94724×10^{-3} Pa at 0.8 mm/s. Similarly, the Lidinoid scaffold shows a similar increase, with WSS values ranging from 1.30586×10^{-3} Pa at 0.5 mm/s to 1.82312×10^{-3} Pa at 0.8 mm/s.

However, the Gyroid scaffold consistently shows higher wall shear stress values than the Lidinoid scaffold for all velocities. The higher wall shear stress observed in the Gyroid scaffold can be attributed to its more optimized, continuous pore

structure, which allows the fluid to flow more efficiently with increasing velocity, thereby generating higher shear stress. This is supported by Shahid et al. [**?**], who found that scaffolds with interconnected pores, like those in the Gyroid, tend to generate higher shear stress, which stimulates osteoblast activity and promotes bone formation.

On the other hand, the Lidinoid scaffold, with its more tortuous pore structure, generates slightly lower shear stress for the same flow velocities. This lower shear stress might reduce the mechanical stimulation needed for osteoblast differentiation and vascularization. However, it could be beneficial in applications where gentler shear forces are preferred to avoid excessive mechanical strain on delicate bone cells in the early stages of healing.

For femoral stem implants in total hip arthroplasty (THA), the higher WSS seen in the Gyroid scaffold suggests it would be more effective in promoting osteointegration and bone remodeling. Higher WSS has been linked to increased osteoblast activity and vascularization, both of which are essential for the long-term success of the femoral stem. The Gyroid scaffold could therefore provide an optimal mechanical environment for bone regeneration, making it a suitable choice for bone tissue engineering in femoral stem.

The Lidinoid scaffold, while generating lower shear stress, may still be effective in scenarios where structural stability is prioritized over biological stimulation. It may be better suited for implants where gentler mechanical cues are required to avoid excessive forces on the surrounding bone tissue during early stages of implant integration.

Chapter 5

Conclusion and Future Recommendations

5.1 Conclusion

This study presents a multiscale design and evaluation of a functionally graded femoral stem that integrates a TPMS porous proximal region with a roughened distal segment to balance structural safety and biological integration in THA. Surface roughness was strategically applied to the distal stem region to enhance osseointegration. Six TPMS structures were analyzed through AH, after which Gyroid and Lidinoid were selected based on bone-like effective moduli, then embedded into a validated FEA and CFD workflow to evaluate the structural integrity and fluid transport through TPMS-based femoral stems.

5.1.1 Structural Response

Under ISO 7206-4 loading, introducing TPMS increases deformation relative to a solid stem while remaining within safe limits. Solid, Gyroid-based, and Lidinoid-based stems exhibited peak total deformations of 0.32 mm, 0.53 mm, and 0.68 mm respectively.

5.1.2 Stress Distribution

Von Mises stress distributions confirm adequate safety margins for Gyroid and identify a narrower margin for Lidinoid. Average stresses were 3.74 MPa for solid, 177.91 MPa for Gyroid, and 204.04 MPa for Lidinoid, with Gyroid remaining below the yield strength of Ti6Al7Nb while improving physiological load transfer.

5.1.3 Fluid Transport under Newtonian Conditions

Gyroid shows slightly higher permeability than Lidinoid across 0.5 to 0.8 mm/s, 1.20×10^{-5} to 1.18×10^{-5} $\mathbf{m^2}$ for Gyroid versus 1.20×10^{-5} to 1.26×10^{-5} $\mathbf{m^2}$ for Lidinoid. It also yields higher WSS at each inlet velocity: 0.00018–0.00028 Pa for Gyroid versus 0.00016–0.00027 Pa for Lidinoid.

5.1.4 Fluid Transport under Non-Newtonian Conditions

The Gyroid and Lidinoid stems exhibited permeability values of 5.83×10^{-6} to 5.81×10^{-6} $\mathbf{m^2}$ and 5.80×10^{-6} to 5.79×10^{-6} $\mathbf{m^2}$, while WSS increased to 0.00139–0.00195 Pa for Gyroid and 0.00131–0.00182 Pa for Lidinoid.

5.1.5 Overall Findings

The results indicate that a Gyroid-based porous proximal region offers the best combined profile of mechanical safety, load sharing to mitigate stress shielding, and a microenvironment that supports bone ingrowth.

5.2 Future Recommendations

Building upon the promising computational findings of this study, several avenues for future research and development are highlighted.

5.2.1 Additive Manufacturing and Experimental Validation

The functionally graded femoral stem designs, particularly those based on the Gyroid lattice, should be fabricated using advanced additive manufacturing techniques such as selective laser melting (SLM). Experimental mechanical testing—including compression, fatigue, and torsion tests—will be essential to validate the predicted mechanical properties and structural performance observed in the simulations.

5.2.2 Biological and Clinical Evaluation

Following successful fabrication and mechanical characterization, *in vitro* biological studies should assess cellular response, osteoblast adhesion, and proliferation on the implant surfaces. Ultimately, clinical trials will be necessary to evaluate long-term implant integration, functionality, and patient outcomes to establish the safety and efficacy of the proposed design in real-world scenarios.

5.2.3 Improved Computational Tools for TPMS Modeling

Due to the inherent geometric complexity of TPMS lattice structures, simulation and meshing present significant computational challenges. The development of specialized software or algorithmic tools tailored for efficient meshing, homogenization, and multiphysics simulation of these complex geometries would greatly facilitate future implant design workflows. Such tools should prioritize usability, scalability, and integration with existing CAD and finite element platforms.

5.2.4 Methodological Extensions

Further work can explore nonlinear, dynamic, and fatigue behavior of functionally graded TPMS implants under physiological loading conditions. Additionally,

incorporating patient-specific anatomical data and varying bone qualities will enhance the personalization and clinical relevance of the implant designs.

Bibliography

[1] A. Chang, G. Breeland, A. C. Black, and J. B. Hubbard, "Anatomy, bony pelvis and lower limb: femur," in *StatPearls*, StatPearls Publishing, 2023.

[2] I. Garrison, G. Domingue, and M. W. Honeycutt, "Subtrochanteric femur fractures: current review of management," *EFORT Open Reviews*, vol. 6, no. 2, pp. 145–151, 2021.

[3] "Femur (thigh bone): Definition, location, anatomy, & diagrams," 2025. Accessed: Aug. 23, 2025.

[4] "Femur - physiopedia," 2025. Accessed: Aug. 23, 2025.

[5] RadiologyKey, "Pelvis and upper femora." https://radiologykey.com/pelvis-and-upper-femora/. Accessed: 2025-01-12.

[6] "The femur - proximal - distal - shaft - teachmeanatomy," 2025. Accessed: Aug. 23, 2025.

[7] "Femur (thigh bone): Definition, location, anatomy, & diagrams," Aug. 2025. Accessed: Aug. 23, 2025.

[8] "Femur (thigh bone): Definition, location, anatomy, & diagrams." https://www.theskeletalsystem.net/leg-bone/femur.html, 2025. Accessed: Aug. 23, 2025.

[9] H. Fischer, T. Maleitzke, C. Eder, S. Ahmad, U. Stöckle, and K. Braun, "Management of proximal femur fractures in the elderly: current concepts and treatment options," *European journal of medical research*, vol. 26, no. 1, p. 86, 2021.

[10] R. W. Bucholz, "Indications, techniques and results of total hip replacement in the united states," *Revista Médica Clínica Las Condes*, vol. 25, no. 5, pp. 756–759, 2014.

[11] K. Allen, L. Thoma, and Y. Golightly, "Epidemiology of osteoarthritis," *Osteoarthritis and cartilage*, vol. 30, no. 2, pp. 184–195, 2022.

[12] The Business Research Company, "Hip replacement market report 2025 - insights and forecast," 2025. Accessed: 2025-04-30.

[13] E. A. Alkady, Z. I. Selim, M. M. Abdelaziz, and F. A. El-Hafeez, "Epidemiology and socioeconomic burden of osteoarthritis," *Journal of Current Medical Research and Practice*, vol. 8, no. 1, pp. 7–11, 2023.

[14] I. Shichman, M. Roof, N. Askew, L. Nherera, J. C. Rozell, T. M. Seyler, and R. Schwarzkopf, "Projections and epidemiology of primary hip and knee arthroplasty in medicare patients to 2040-2060," *JBJS Open Access*, vol. 8, no. 1, p. e22, 2023.

[15] C. Clar, L. Leitner, A. Koutp, G. Hauer, L. Rasic, A. Leithner, and P. Sadoghi, "The worldwide survival rate of total hip arthroplasties is improving: a systematic comparative analysis using worldwide hip arthroplasty registers," *EFORT Open Reviews*, vol. 9, no. 8, pp. 745–750, 2024.

[16] Fortune Business Insights, "Hip replacement market size, share — growth analysis [2032]," 2025. Accessed: 2025-04-23.

[17] L. Guo, S. A. Naghavi, Z. Wang, S. N. Varma, Z. Han, Z. Yao, L. Wang, L. Wang, and C. Liu, "On the design evolution of hip implants: A review," *Materials & Design*, vol. 216, p. 110552, 2022.

[18] A. Katakam, S. Hosseinzadeh, T. J. Humphrey, A. Collins, D. Shin, C. M. Melnic, C. Bragdon, and H. S. Bedair, "Different designs of proximal femoral stems for total hip arthroplasty: mid-term clinical and patient-reported functional outcomes," *Cureus*, vol. 13, no. 11, 2021.

[19] B. Ziaie, X. Velay, and W. Saleem, "Advanced porous hip implants: A comprehensive review," *Heliyon*, 2024.

[20] M. Loppini and G. Grappiolo, "Uncemented short stems in primary total hip arthroplasty: the state of the art," *EFORT open reviews*, vol. 3, no. 5, pp. 149–159, 2018.

[21] L. Kong, *Design of femoral implant with functionally graded TPMS for stress shielding reduction*. McGill University (Canada), 2023.

[22] C. Stadler, A. Edinger, B. Schauer, D. Haslhofer, T. Gotterbarm, and M. Luger, "Stem design affects templating adherence in total hip arthroplasty-a retrospective cohort study comparing two types of cementless short stems.," *Journal of Orthopaedic Surgery and Research*, vol. 20, no. 1, p. 383, 2025.

[23] P. Hernigou, S. Quiennec, and I. Guissou, "Hip hemiarthroplasty: from venable and bohlman to moore and thompson," *International orthopaedics*, vol. 38, no. 3, pp. 655–661, 2014.

[24] N. C. Bota, D.-V. Nistor, S. Caterev, and A. Todor, "Historical overview of hip arthroplasty: from humble beginnings to a high-tech future," *Orthopedic reviews*, vol. 13, no. 1, p. 8773, 2021.

[25] S. R. Knight, R. Aujla, and S. P. Biswas, "Total hip arthroplasty-over 100 years of operative history," *Orthopedic reviews*, vol. 3, no. 2, p. e16, 2011.

[26] H. Wellauer, R. Heuberger, E. Gautier, M. Tannast, H. Steinke, and P. Wahl, "The history of the development of the regular straight stem in hip arthroplasty," *EFORT Open Reviews*, vol. 8, no. 7, pp. 548–560, 2023.

[27] P. F. Gomez and J. A. Morcuende, "A historical and economic perspective on sir john charnley, chas f. thackray limited, and the early arthroplasty industry," *The Iowa orthopaedic journal*, vol. 25, p. 30, 2005.

[28] E. Marin and A. Lanzutti, "Biomedical applications of titanium alloys: a comprehensive review," *Materials*, vol. 17, no. 1, p. 114, 2023.

[29] L. Guo, S. A. Naghavi, Z. Wang, S. N. Varma, Z. Han, Z. Yao, L. Wang, L. Wang, and C. Liu, "On the design evolution of hip implants: A review," *Materials & Design*, vol. 216, p. 110552, 2022.

[30] Y.-Y. Chung, C.-H. Im, D.-H. Kim, J.-Y. Heo, and Y.-J. Jang, "The effect of hydroxyapatite coating on long-term results of total hip arthroplasty with hydroxyapatite-coated anatomic femoral stem," *Hip & pelvis*, vol. 26, no. 3, pp. 143–149, 2014.

[31] S. A. Tyagi and M. Manjaiah, "Additive manufacturing of titanium-based lattice structures for medical applications–a review," *Bioprinting*, vol. 30, p. e00267, 2023.

[32] A. A. Noman, M. S. Shaari, H. Mehboob, and A. H. Azman, "Recent advancements in additively manufactured hip implant design using topology optimization technique," *Results in Engineering*, p. 103932, 2025.

[33] Y. Li, D. Jiang, R. Zhao, X. Wang, L. Wang, and L. C. Zhang, "High mechanical performance of lattice structures fabricated by additive manufacturing," *metals*, 2024.

[34] J. Fu *et al.*, "Investigating the mechanical performance of the triply periodic minimal surface based metallic lattices made by micro laser powder bed fusion," 2022.

[35] S. Vijayavenkataraman, L. Zhang, S. Zhang, J. Y. Hsi Fuh, and W. F. Lu, "Triply periodic minimal surfaces sheet scaffolds for tissue engineering applications: An optimization approach toward biomimetic scaffold design," *ACS Applied Bio Materials*, vol. 1, no. 2, pp. 259–269, 2018.

[36] G. Savio, R. Meneghello, and G. Concheri, "Design of variable thickness triply periodic surfaces for additive manufacturing," *Progress in Additive manufacturing*, vol. 4, no. 3, pp. 281–290, 2019.

[37] B. Rawal, R. Ribeiro, R. Malhotra, and N. Bhatnagar, "Design and manufacturing of femoral stems for the indian population," *Journal of Manufacturing Processes*, vol. 14, no. 3, pp. 216–223, 2012.

[38] B. Liu, H. Wang, N. Zhang, M. Zhang, and C.-K. Cheng, "Femoral stems with porous lattice structures: a review," *Frontiers in Bioengineering and Biotechnology*, vol. 9, p. 772539, 2021.

[39] K. B. Hazlehurst, C. J. Wang, and M. Stanford, "A numerical investigation into the influence of the properties of cobalt chrome cellular structures on the load transfer to the periprosthetic femur following total hip arthroplasty," *Medical engineering & physics*, vol. 36, no. 4, pp. 458–466, 2014.

[40] S. Arabnejad, B. Johnston, M. Tanzer, and D. Pasini, "Fully porous 3d printed titanium femoral stem to reduce stress-shielding following total hip arthroplasty," *Journal of Orthopaedic Research*, vol. 35, no. 8, pp. 1774–1783, 2017.

[41] S. A. Khanoki and D. Pasini, "Fatigue design of a mechanically biocompatible lattice for a proof-of-concept femoral stem," *journal of the mechanical behavior of biomedical materials*, vol. 22, pp. 65–83, 2013.

[42] S. Arabnejad Khanoki and D. Pasini, "Multiscale design and multiobjective optimization of orthopedic hip implants with functionally graded cellular material," 2012.

[43] R. Aversa, F. I. Petrescu, R. V. Petrescu, and A. Apicella, "Flexible stem trabecular prostheses," *American Journal of Engineering and Applied Sciences*, vol. 9, no. 4, 2016.

[44] M. Meng, J. Wang, H. Huang, X. Liu, J. Zhang, and Z. Li, "3d printing metal implants in orthopedic surgery: methods, applications and future prospects," *Journal of orthopaedic translation*, vol. 42, pp. 94–112, 2023.

[45] A. Barfeie, J. Wilson, and J. Rees, "Implant surface characteristics and their effect on osseointegration," *British dental journal*, vol. 218, no. 5, pp. E9–E9, 2015.

[46] M. Romero-Serrano, M.-M. Romero-Ruiz, M. Herrero-Climent, B. Rios-Carrasco, and J. Gil-Mur, "Correlation between implant surface roughness and implant stability: A systematic review," *Dentistry Journal*, vol. 12, no. 9, p. 276, 2024.

[47] S. R. Konda, "Anatomy of the proximal femur," in *Proximal Femur Fractures: An Evidence-Based Approach to Evaluation and Management*, pp. 1–7, Springer, 2017.

[48] M. Rabbani, *Development of optimal total hip joint replacement*. PhD thesis, Birmingham City University, 2018.

[49] E. Seeman, "Bone quality: the material and structural basis of bone strength," *Journal of bone and mineral metabolism*, vol. 26, pp. 1–8, 2008.

[50] M. Bittner-Frank, A. G. Reisinger, O. G. Andriotis, D. H. Pahr, and P. J. Thurner, "Cortical and trabecular mechanical properties in the femoral neck vary differently with changes in bone mineral density," *JBMR plus*, vol. 8, no. 6, p. ziae049, 2024.

[51] J. E. Schanda, R. Kocijan, H. Resch, A. Baierl, X. Feichtinger, R. Mittermayr, F. Plachel, R. Wakolbinger, K. Wolff, C. Fialka, *et al.*, "Bone stress injuries are associated with differences in bone microarchitecture in male professional soldiers," *Journal of Orthopaedic Research®*, vol. 37, no. 12, pp. 2516–2523, 2019.

[52] C. Feng, K. Zhang, S. Zhan, Y. Gan, X. Xiang, and W. Niu, "Mechanical impact of regional structural deterioration and tissue-level compensation on proximal femur trabecular bone," *Frontiers in Bioengineering and Biotechnology*, vol. 12, p. 1448708, 2024.

[53] X. Huang, L. Zheng, D. Zheng, S. Li, Y. Fan, Z. Lin, and S. Huang, "Studying trabecular bone samples demonstrates a power law relation between deteriorated structure and mechanical properties-a study combining 3d printing with the finite element method," *Frontiers in Endocrinology*, vol. 14, p. 1061758, 2023.

[54] S. Bolamperti, I. Villa, and A. Rubinacci, "Bone remodeling: an operational process ensuring survival and bone mechanical competence," *Bone Research*, vol. 10, no. 1, p. 48, 2022.

[55] C. V. Cook, A. M. Lighty, B. J. Smith, and A. N. Ford Versypt, "A review of mathematical modeling of bone remodeling from a systems biology perspective," *Frontiers in Systems Biology*, vol. 4, p. 1368555, 2024.

[56] D. J. Hadjidakis and I. I. Androulakis, "Bone remodeling," *Annals of the New York academy of sciences*, vol. 1092, no. 1, pp. 385–396, 2006.

[57] K. Alvarez and H. Nakajima, "Metallic scaffolds for bone regeneration," *Materials*, vol. 2, no. 3, pp. 790–832, 2009.

[58] J. Wolff, *The law of bone remodelling*. Springer Science & Business Media, 2012.

[59] M. Kanto, S. Fukunishi, T. Fukui, S. Nishio, Y. Fujihara, S. Okahisa, Y. Takeda, S. Yoshiya, and T. Tachibana, "Radiological evaluation of the relationship between cortical hypertrophy and stress shielding after total hip arthroplasty using a cementless stem," *Arthroplasty Today*, vol. 6, no. 4, pp. 894–900, 2020.

[60] C. Chatzigeorgiou, B. Piotrowski, Y. Chemisky, P. Laheurte, and F. Meraghni, "Numerical investigation of the effective mechanical properties and local stress distributions of tpms-based and strut-based lattices for biomedical applications," *Journal of the mechanical behavior of biomedical materials*, vol. 126, p. 105025, 2022.

[61] Z. Liu, H. Gong, and J. Gao, "Enhancement in the fatigue resistances of triply periodic surfaces-based scaffolds," *International Journal of Mechanical Sciences*, vol. 245, p. 108119, 2023.

[62] M. Rezapourian, I. Jasiuk, M. Saarna, and I. Hussainova, "Selective laser melted ti6al4v split-p tpms lattices for bone tissue engineering," *International Journal of Mechanical Sciences*, vol. 251, p. 108353, 2023.

[63] J. Corona-Castuera, D. Rodriguez-Delgado, J. Henao, J. C. Castro-Sandoval, and C. A. Poblano-Salas, "Design and fabrication of a customized partial hip prosthesis employing ct-scan data and lattice porous structures," *ACS omega*, vol. 6, no. 10, pp. 6902–6913, 2021.

[64] P. Müller, A. Synek, T. Stauß, C. Steinnagel, T. Ehlers, P. C. Gembarski, D. Pahr, and R. Lachmayer, "Development of a density-based topology optimization of homogenized lattice structures for individualized hip endoprostheses and validation using micro-fe," *Scientific Reports*, vol. 14, no. 1, p. 5719, 2024.

[65] J. Moghariya and P. K. Gurrala, "Finite element studies on triply periodic minimal surfaces (tpms)–based hip replacement implants," *The International Journal of Advanced Manufacturing Technology*, vol. 136, no. 1, pp. 263–277, 2025.

[66] Z. F. M. Salaha, M. I. Ammarullah, N. N. A. A. Abdullah, A. U. A. Aziz, H.-S. Gan, A. H. Abdullah, M. R. Abdul Kadir, and M. H. Ramlee, "Biomechanical effects of the porous structure of gyroid and voronoi hip implants: a finite element analysis using an experimentally validated model," *Materials*, vol. 16, no. 9, p. 3298, 2023.

[67] N. Rahmat, J. Kadkhodapour, and M. Arbabtafti, "Study of cellular femoral stem for stress shielding and interface stability," *The International Journal of Artificial Organs*, vol. 46, no. 6, pp. 370–377, 2023.

[68] B. Jetté, V. Brailovski, M. Dumas, C. Simoneau, and P. Terriault, "Femoral stem incorporating a diamond cubic lattice structure: Design, manufacture and testing," *Journal of the Mechanical Behavior of Biomedical Materials*, vol. 77, pp. 58–72, 2018.

[69] S. A. Naghavi, M. Tamaddon, P. Garcia-Souto, M. Moazen, S. Taylor, J. Hua, and C. Liu, "A novel hybrid design and modelling of a customised graded ti-6al-4v porous hip implant to reduce stress-shielding: An experimental and numerical analysis," *Frontiers in bioengineering and biotechnology*, vol. 11, p. 1092361, 2023.

[70] N. Kladovasilakis, K. Tsongas, and D. Tzetzis, "Finite element analysis of orthopedic hip implant with functionally graded bioinspired lattice structures," *Biomimetics*, vol. 5, no. 3, p. 44, 2020.

[71] E. Davoodi, H. Montazerian, R. Esmaeilizadeh, A. C. Darabi, A. Rashidi, J. Kadkhodapour, H. Jahed, M. Hoorfar, A. S. Milani, P. S. Weiss, *et al.*, "Additively manufactured gradient porous ti–6al–4v hip replacement implants embedded with cell-laden gelatin methacryloyl hydrogels," *ACS applied materials & interfaces*, vol. 13, no. 19, pp. 22110–22123, 2021.

[72] N. Viet, W. Waheed, A. Alazzam, and W. Zaki, "Effective compressive behavior of functionally graded tpms titanium implants with ingrown cortical or trabecular bone," *Composite Structures*, vol. 303, p. 116288, 2023.

[73] T. E. TUNCA and N. Ü. TAŞKIN, "Effects of different tpms lattice structures on the mechanical behaviour of hip implant," in *PROCEEDINGS OF IV. INTERNATIONAL AGRICULTURAL, BIOLOGICAL & LIFE SCIENCE CONFERENCE AGBIOL 2022*, p. 725, 2022.

[74] S. A. Naghavi, M. Tamaddon, A. Marghoub, K. Wang, B. B. Babamiri, K. Hazeli, W. Xu, X. Lu, C. Sun, L. Wang, *et al.*, "Mechanical characterisation and numerical modelling of tpms-based gyroid and diamond ti6al4v scaffolds for bone implants: an integrated approach for translational consideration," *Bioengineering*, vol. 9, no. 10, p. 504, 2022.

[75] S. A. Naghavi, *Modelling and in vitro evaluation of customised Ti6Al4V and PEEK hip implants for improving osseointegration and reducing stress shielding*. PhD thesis, UCL (University College London), 2023.

[76] J. Feng, J. Fu, X. Yao, and Y. He, "Triply periodic minimal surface (tpms) porous structures: from multi-scale design, precise additive manufacturing to multidisciplinary applications," *International Journal of Extreme Manufacturing*, vol. 4, no. 2, p. 022001, 2022.

[77] J. Feng, J. Fu, X. Yao, and Y. He, "Triply periodic minimal surface (tpms) porous structures: from multi-scale design, precise additive manufacturing to multidisciplinary applications," *International Journal of Extreme Manufacturing*, vol. 4, no. 2, p. 022001, 2022.

[78] H. Montazerian, M. Zhianmanesh, E. Davoodi, A. Milani, and M. Hoorfar, "Longitudinal and radial permeability analysis of additively manufactured porous scaffolds: Effect of pore shape and porosity," *Materials & design*, vol. 122, pp. 146–156, 2017.

[79] M. Zhianmanesh, M. Varmazyar, and H. Montazerian, "Fluid permeability of graded porosity scaffolds architectured with minimal surfaces," *ACS Biomaterials Science & Engineering*, vol. 5, no. 3, pp. 1228–1237, 2019.

[80] H. Montazerian, M. Mohamed, M. M. Montazeri, S. Kheiri, A. Milani, K. Kim, and M. Hoorfar, "Permeability and mechanical properties of gradient porous pdms scaffolds fabricated by 3d-printed sacrificial templates designed with minimal surfaces," *Acta biomaterialia*, vol. 96, pp. 149–160, 2019.

[81] S. Ma, Q. Tang, Q. Feng, J. Song, X. Han, and F. Guo, "Mechanical behaviours and mass transport properties of bone-mimicking scaffolds consisted of gyroid structures manufactured using selective laser melting," *Journal of the mechanical behavior of biomedical materials*, vol. 93, pp. 158–169, 2019.

[82] R. Asbai-Ghoudan, S. R. de Galarreta, and N. Rodriguez-Florez, "Analytical model for the prediction of permeability of triply periodic minimal surfaces," *Journal of the Mechanical Behavior of Biomedical Materials*, vol. 124, p. 104804, 2021.

[83] D. Ali and S. Sen, "Finite element analysis of mechanical behavior, permeability and fluid induced wall shear stress of high porosity scaffolds with gyroid and lattice-based architectures," *Journal of the mechanical behavior of biomedical materials*, vol. 75, pp. 262–270, 2017.

[84] J. Santos, T. Pires, B. P. Gouveia, A. P. Castro, and P. R. Fernandes, "On the permeability of tpms scaffolds," *Journal of the Mechanical Behavior of Biomedical Materials*, vol. 110, p. 103932, 2020.

[85] H. Montazerian, E. Davoodi, M. Asadi-Eydivand, J. Kadkhodapour, and M. Solati-Hashjin, "Porous scaffold internal architecture design based on

minimal surfaces: a compromise between permeability and elastic properties," *Materials & Design*, vol. 126, pp. 98–114, 2017.

[86] G. Yu, Z. Li, S. Li, Q. Zhang, Y. Hua, H. Liu, X. Zhao, D. T. Dhaidhai, W. Li, and X. Wang, "The select of internal architecture for porous ti alloy scaffold: A compromise between mechanical properties and permeability," *Materials & Design*, vol. 192, p. 108754, 2020.

[87] Z. Li, Z. Chen, X. Chen, and R. Zhao, "Effect of unit configurations and parameters on the properties of ti–6al–4v unit-stacked scaffolds: a trade-off between mechanical and permeable performance," *Journal of the Mechanical Behavior of Biomedical Materials*, vol. 116, p. 104332, 2021.

[88] D. Ali, M. Ozalp, S. B. Blanquer, and S. Onel, "Permeability and fluid flow-induced wall shear stress in bone scaffolds with tpms and lattice architectures: A cfd analysis," *European Journal of Mechanics-B/Fluids*, vol. 79, pp. 376–385, 2020.

[89] J.-W. Luo, L. Chen, T. Min, F. Shan, Q. Kang, and W. Tao, "Macroscopic transport properties of gyroid structures based on pore-scale studies: permeability, diffusivity and thermal conductivity," *International Journal of Heat and Mass Transfer*, vol. 146, p. 118837, 2020.

[90] M. N. Shahid, M. M. Khan, M. U. Shahid, and S. Rasheed, "Fluidic properties of diamond and splitp structures with varying porosity levels in tissue engineering applications: A computational fluid dynamics analysis," *Engineering Proceedings*, vol. 75, no. 1, p. 39, 2024.

[91] K. Avsec, M. Jenko, M. Conradi, A. Kocijan, A. Vesel, J. Kovač, M. Godec, I. Belič, B. Šetina Batič, Č. Donik, *et al.*, "Surface properties of retrieved cementless femoral hip endoprostheses produced from a ti6al7nb alloy," *Coatings*, vol. 9, no. 12, p. 868, 2019.

[92] Y. Liu, B. Rath, M. Tingart, and J. Eschweiler, "Role of implants surface modification in osseointegration: A systematic review," *Journal of Biomedical Materials Research Part A*, vol. 108, no. 3, pp. 470–484, 2020.

[93] A. Vulović, F. G. Warchomicka, F. Pixner, and N. Filipović, "Analysis of modified surface topographies of titanium-based hip implants using finite element method," *Technology and Health Care*, vol. 32, no. 2, pp. 1123–1133, 2024.

[94] T. Kawai, K. Goto, Y. Kuroda, Y. Okuzu, and S. Matsuda, "High subsidence rate after primary total hip arthroplasty using a zweymüller-type noncemented implant with a matte surface," *JAAOS Global Research & Reviews*, vol. 6, no. 6, p. e21, 2022.

[95] L. Capitanu, L.-L. Badita, C. Tiganesteanu, and V. Florescu, "Influence of the taper on the fretting wear of the femoral stem-femoral head taper junction in total hip prosthesis," *Industrial Lubrication and Tribology*, vol. 74, no. 4, pp. 385–391, 2022.

[96] A. Schuh, U. Holzwarth, W. Kachler, J. Göske, and G. Zeiler, "Surface characterization of al2o3-blasted titanium implants in total hip arthroplasty," *Der Orthopäde*, vol. 33, pp. 905–910, 2004.

[97] D. Ali and S. Sen, "Computational fluid dynamics study of the effects of surface roughness on permeability and fluid flow-induced wall shear stress in scaffolds," *Annals of biomedical engineering*, vol. 46, pp. 2023–2035, 2018.

[98] B. Hoffmann, G. Ziegler, R. Lange, U. Beck, L. Müller, E. Conforto, F. A. Müller, U. T. Seyfert, F. Aubertin, A. Gorbunoff, *et al.*, "Topological surface modifications," *Metallic Biomaterial Interfaces*, pp. 19–50, 2008.

[99] F. Rupp, L. Scheideler, N. Olshanska, M. De Wild, M. Wieland, and J. Geis-Gerstorfer, "Enhancing surface free energy and hydrophilicity through chemical modification of microstructured titanium implant surfaces," *Journal of Biomedical Materials Research Part A: An Official Journal of The Society for Biomaterials, The Japanese Society for Biomaterials, and The Australian Society for Biomaterials and the Korean Society for Biomaterials*, vol. 76, no. 2, pp. 323–334, 2006.

[100] L. F. Cooper, "A role for surface topography in creating and maintaining bone at titanium endosseous implants," *The Journal of prosthetic dentistry*, vol. 84, no. 5, pp. 522–534, 2000.

[101] M. Janeczek, P. Szymczyk, M. Dobrzynski, O. Parulska, M. Szymonowicz, P. Kuropka, Z. Rybak, B. Zywicka, G. Ziolkowski, K. Marycz, *et al.*, "Influence of surface modifications of a nanostructured implant on osseointegration capacity–preliminary in vivo study," *RSC advances*, vol. 8, no. 28, pp. 15533–15546, 2018.

[102] A. Bensoussan, J.-L. Lions, and G. Papanicolaou, *Asymptotic analysis for periodic structures*, vol. 374. American Mathematical Soc., 2011.

[103] M. Sayahi, S. Sghaier, and H. Belhadjsalah, "Finite element analysis of ball burnishing process: comparisons between numerical results and experiments," *The International Journal of Advanced Manufacturing Technology*, vol. 67, no. 5, pp. 1665–1673, 2013.

[104] A. Schuh, C. Zeller, U. Holzwarth, W. Kachler, G. Wilcke, G. Zeiler, B. Eigenmann, and J. Bigoney, "Deep rolling of titanium rods for application in modular total hip arthroplasty," *Journal of Biomedical Materials Research Part B: Applied Biomaterials: An Official Journal of The Society for Biomaterials, The Japanese Society for Biomaterials, and The Australian Society for Biomaterials and the Korean Society for Biomaterials*, vol. 81, no. 2, pp. 330–335, 2007.

[105] L. Kong, *Design of femoral implant with functionally graded TPMS for stress shielding reduction*. McGill University (Canada), 2023.

[106] H. H. Bayraktar, E. F. Morgan, G. L. Niebur, G. E. Morris, E. K. Wong, and T. M. Keaveny, "Comparison of the elastic and yield properties of human femoral trabecular and cortical bone tissue," *Journal of biomechanics*, vol. 37, no. 1, pp. 27–35, 2004.

[107] Stryker, "Secur-fit advanced." https://www.stryker.com/us/en/joint-replacement/products/secur-fit-advanced.html. Accessed: 31 July 2025.

[108] X. Hu, N. Zheng, Y. Chen, K. Dai, D. Dimitriou, H. Li, and T.-Y. Tsai, "Optimizing the femoral offset for restoring physiological hip muscle function in patients with total hip arthroplasty," *Frontiers in Bioengineering and Biotechnology*, vol. 9, p. 645019, 2021.

[109] D. Barba, E. Alabort, and R. Reed, "Synthetic bone: Design by additive manufacturing," *Acta biomaterialia*, vol. 97, pp. 637–656, 2019.

[110] O. Mishchenko, K. Volchykhina, D. Maksymov, O. Manukhina, M. Pogorielov, M. Pavlenko, and I. Iatsunskyi, "Advanced strategies for enhancing the biocompatibility and antibacterial properties of implantable structures," *Materials*, vol. 18, no. 4, p. 822, 2025.

[111] P. Damm, I. Kutzner, G. Bergmann, A. Rohlmann, and H. Schmidt, "Comparison of in vivo measured loads in knee, hip and spinal implants during level walking," *Journal of Biomechanics*, vol. 51, pp. 128–132, 2017.

[112] G. Bergmann, G. Deuretzbacher, M. Heller, F. Graichen, A. Rohlmann, J. Strauss, and G. Duda, "Hip contact forces and gait patterns from routine activities," *Journal of biomechanics*, vol. 34, no. 7, pp. 859–871, 2001.

[113] B. Jetté, V. Brailovski, M. Dumas, C. Simoneau, and P. Terriault, "Femoral stem incorporating a diamond cubic lattice structure: Design, manufacture and testing," *Journal of the Mechanical Behavior of Biomedical Materials*, vol. 77, pp. 58–72, 2018.

[114] X. Xue, M. K. Patel, M. Kersaudy-Kerhoas, M. P. Desmulliez, C. Bailey, and D. Topham, "Analysis of fluid separation in microfluidic t-channels," *Applied Mathematical Modelling*, vol. 36, no. 2, pp. 743–755, 2012.

[115] D. Egger, M. Fischer, A. Clementi, V. Ribitsch, J. Hansmann, and C. Kasper, "Development and characterization of a parallelizable perfusion bioreactor for 3d cell culture," *Bioengineering*, vol. 4, no. 2, p. 51, 2017.

[116] A. Schindeler, M. M. McDonald, P. Bokko, and D. G. Little, "Bone remodeling during fracture repair: The cellular picture," in *Seminars in cell & developmental biology*, vol. 19, pp. 459–466, Elsevier, 2008.

[117] R. Marsell and T. A. Einhorn, "The biology of fracture healing," *Injury*, vol. 42, no. 6, pp. 551–555, 2011.

[118] J. Vimmr, A. Jonášová, and O. Bublík, "Numerical analysis of non-newtonian blood flow and wall shear stress in realistic single, double and triple aorto-coronary bypasses," *International journal for numerical methods in biomedical engineering*, vol. 29, no. 10, pp. 1057–1081, 2013.

[119] M. Nouri, F. Jalali, G. Karimi, and K. Zarrabi, "Image-based computational simulation of sub-endothelial ldl accumulation in a human right coronary artery," *Computers in biology and medicine*, vol. 62, pp. 206–221, 2015.

[120] D. Mandal, N. Manna, and S. Chakrabarti, "Numerical study of blood flow through different double bell-shaped stenosed coronary artery during the progression of the disease, atherosclerosis," *International Journal of Numerical Methods for Heat & Fluid Flow*, vol. 20, no. 6, pp. 670–698, 2010.

[121] E. K. Shang, D. P. Nathan, R. M. Fairman, J. E. Bavaria, R. C. Gorman, J. H. Gorman III, and B. M. Jackson, "Use of computational fluid dynamics studies in predicting aneurysmal degeneration of acute type b aortic dissections," *Journal of vascular surgery*, vol. 62, no. 2, pp. 279–284, 2015.

[122] S. Wang, L. Lee, and J. Lee, "A linear relation between the compressibility and density of blood," *The Journal of the Acoustical Society of America*, vol. 109, no. 1, pp. 390–396, 2001.

[123] S. Gómez, M. D. Vlad, J. López, and E. Fernández, "Design and properties of 3d scaffolds for bone tissue engineering," *Acta biomaterialia*, vol. 42, pp. 341–350, 2016.

[124] B. M. Johnston, P. R. Johnston, S. Corney, and D. Kilpatrick, "Non-newtonian blood flow in human right coronary arteries: steady state simulations," *Journal of biomechanics*, vol. 37, no. 5, pp. 709–720, 2004.

[125] M. A. Hussain, S. Kar, and R. R. Puniyani, "Relationship between power law coefficients and major blood constituents affecting the whole blood viscosity," *Journal of Biosciences*, vol. 24, no. 3, pp. 329–337, 1999.

[126] S. S. Shibeshi and W. E. Collins, "The rheology of blood flow in a branched arterial system," *Applied rheology*, vol. 15, no. 6, pp. 398–405, 2005.

[127] A. F. Morais, H. Seybold, H. J. Herrmann, and J. S. Andrade Jr, "Non-newtonian fluid flow through three-dimensional disordered porous media," *Physical review letters*, vol. 103, no. 19, p. 194502, 2009.

[128] M. G. Bixel, A. P. Kusumbe, S. K. Ramasamy, K. K. Sivaraj, S. Butz, D. Vestweber, and R. H. Adams, "Flow dynamics and hspc homing in bone marrow microvessels," *Cell reports*, vol. 18, no. 7, pp. 1804–1816, 2017.

[129] D. Ali and S. Sen, "Permeability and fluid flow-induced wall shear stress of bone tissue scaffolds: Computational fluid dynamic analysis using newtonian and non-newtonian blood flow models," *Computers in biology and medicine*, vol. 99, pp. 201–208, 2018.

[130] C. Yan, L. Hao, A. Hussein, and P. Young, "Ti–6al–4v triply periodic minimal surface structures for bone implants fabricated via selective laser melting," *Journal of the mechanical behavior of biomedical materials*, vol. 51, pp. 61–73, 2015.

[131] M. N. Shahid, M. U. Shahid, S. Rasheed, M. Irfan, and M. A. Obeidi, "Computational investigation of the fluidic properties of triply periodic minimal surface (tpms) structures in tissue engineering," *Designs*, vol. 8, no. 4, p. 69, 2024.

[132] D. Ali and S. Sen, "Permeability and fluid flow-induced wall shear stress of bone tissue scaffolds: Computational fluid dynamic analysis using newtonian and non-newtonian blood flow models," *Computers in biology and medicine*, vol. 99, pp. 201–208, 2018.

[133] C. Chatzigeorgiou, B. Piotrowski, Y. Chemisky, P. Laheurte, and F. Meraghni, "Numerical investigation of the effective mechanical properties and

local stress distributions of tpms-based and strut-based lattices for biomedical applications," *Journal of the mechanical behavior of biomedical materials*, vol. 126, p. 105025, 2022.

[134] D. Brindley, K. Moorthy, J.-H. Lee, C. Mason, H.-W. Kim, and I. Wall, "Bioprocess forces and their impact on cell behavior: implications for bone regeneration therapy," *Journal of tissue engineering*, vol. 2011, p. 620247, 2011.

[135] D. Savio and A. Bagno, "When the total hip replacement fails: A review on the stress-shielding effect," *Processes*, vol. 10, no. 3, p. 612, 2022.

[136] C. Wittkowske, G. C. Reilly, D. Lacroix, and C. M. Perrault, "In vitro bone cell models: impact of fluid shear stress on bone formation," *Frontiers in bioengineering and biotechnology*, vol. 4, p. 87, 2016.